

DTIC FILE COPY

2

Study of Short-lived Unstable Nuclei by Means of
Laser Optical Pumping

by

Joseph P. Mackin

B.S. United States Military Academy
(1974)

M.S. Naval Postgraduate School
(1980)

DTIC
ELECTE
JUN 07 1990
S D
Co

AD-A222 561

Submitted to the Department of Physics
in partial fulfillment of the requirements for the degree of

Doctor of Philosophy

at the

MASSACHUSETTS INSTITUTE OF TECHNOLOGY

June 1990

© Massachusetts Institute of Technology 1990

Signature of Author

Joseph P. Mackin

Department of Physics

June 4, 1990

Certified by

Michael S. Feld

Michael S. Feld

Professor of Physics

Thesis Supervisor

Certified by

Ramachandra Dasari

Ramchandra R. Dasari

Principal Research Scientist

Thesis Supervisor

Accepted by

George F. Koster

Chairman, Departmental Committee on Graduate Students

DISTRIBUTION STATEMENT A

Approved for public release
Distribution Unlimited

90 06 06 039

REPORT DOCUMENTATION PAGE

Form Approved
OMB No. 0704-0188

Public reporting burden for this collection of information is estimated to average 1 hour per response, including the time for reviewing instructions, searching existing data sources, gathering and maintaining the data needed, and reviewing the collection of information. Send comments regarding this burden estimate or any other aspect of this collection of information, including suggestions for reducing this burden, to Washington Headquarters Services, Directorate for Information Operations and Reports, 1215 Jefferson Davis Highway, Suite 1204, Arlington, VA 22202-4302, and to the Office of Information and Regulatory Affairs, Office of Management and Budget, Washington, DC 20503.

1. AGENCY USE ONLY (Leave Blank)		2. REPORT DATE E 1990	3. REPORT TYPE AND DATES COVERED Final Report Ph.D. Thesis	
4. TITLE AND SUBTITLE Study of Short-Lived Radioactive nuclei by means of laser optical pumping.			5. FUNDING NUMBERS	
6. AUTHOR(S) Joseph P. Mackin				
7. PERFORMING ORGANIZATION NAME(S) AND ADDRESS(ES) G.R. Harrison Spectroscopy Laboratory Massachusetts Institute of Technology			8. PERFORMING ORGANIZATION REPORT NUMBER	
9. SPONSORING/MONITORING AGENCY NAME(S) AND ADDRESS(ES) HQDA, MILPERCEN (DAPC-OPB-D)			10. SPONSORING/MONITORING AGENCY REPORT NUMBER	
11. SUPPLEMENTARY NOTES				
12a. DISTRIBUTION/AVAILABILITY STATEMENT DISTRIBUTION STATEMENT A Approved for public release Distribution Unlimited			12b. DISTRIBUTION CODE	
13. ABSTRACT (Maximum 200 words) A fundamental measurement using laser spectroscopy of the electric quadrupole moment of the short-lived radioactive isomer ^{85m}Rb .				
14. SUBJECT TERMS			15. NUMBER OF PAGES 157	
			16. PRICE CODE	
17. SECURITY CLASSIFICATION OF REPORT Unclassified	18. SECURITY CLASSIFICATION OF THIS PAGE Unclassified	19. SECURITY CLASSIFICATION OF ABSTRACT Unclassified	20. LIMITATION OF ABSTRACT	

Study of Short-lived Unstable Nuclei by Means of Laser Optical Pumping

by

Joseph P. Mackin

Submitted to the Department of Physics
on June 4, 1990, in partial fulfillment of the
requirements for the degree of
Doctor of Philosophy

Abstract

mu-s *Rb (85m)*
The effectiveness of laser-induced nuclear orientation in the study of short-lived unstable nuclei using radiation detection has been increased by the use of saturation spectroscopy to produce sub-Doppler resolved changes in the anisotropic spatial distribution of the 514-keV gamma rays from the 1 - (μ s) isomer (^{85m}Rb). The width (HWHM) of these change signals is about 60 MHz, a factor of ten better than Doppler-broadened signals previously obtained. This technique has been used to study the D1 and D2 transitions for the isomer. Precise values of the hyperfine A and B coefficients have been determined, and used to extract a value for the nuclear magnetic dipole moment ($6.043 \pm 0.005 \mu_N$), and, for the first time, a measured value of the nuclear quadrupole moment ($-.73 \pm .17$) b. Additionally, and a new, more accurate value for the isomer shift (-113 ± 5) MHz has been determined. *Theses (jhd)*

Thesis Supervisor: Michael S. Feld
Title: Professor of Physics

Thesis Supervisor: Ramchandra R. Dasari
Title: Principal Research Scientist

+ or -

mu sec N

Acknowledgments

I would like to thank the following people who have contributed a great deal to this work: Charlie Holbrow, Tim Hutton, Mike Lercel, Mike Otteson, Bill Quivers, and Greg Shinkaveg.

A special thanks to my advisors, Ramchandra Dasari and Mike Feld, for their help and guidance over the last four years.

A special thanks to my family , my two daughters Katie and Julie, and my loving wife Maureen, for their love and support during this period.

I would also thank the U.S. Army for sending me to school here.

STATEMENT "A" per Ltc. J. Jobe
OPM/TAPC-OPB-D, 200 Stovall St
Alexandria, VA 22332
TELECON 6/7/90

6/7/90

VG

Accession For	
NTIS CRA&I	<input checked="" type="checkbox"/>
DTIC TAB	<input type="checkbox"/>
Unannounced	<input type="checkbox"/>
Justification	
By <i>per call</i>	
Distribution /	
Availability Codes	
Dist	Avail and/or Special
A-1	

1
QUALITY
INSPECTED

Contents

1	Introduction and Overview	13
1.1	The Study of Short-Lived Nuclei: Why and How	14
1.1.1	Techniques Based on the Detection of Optical Photons	14
1.1.2	Techniques Based on Detection of Atoms and Ions	16
1.1.3	Methods Detecting Nuclear Radiation: RADOP	17
1.2	Brief Review of the MIT LINO Project: Successful Development of the ^{85m}Rb Gas-Cell System	20
1.2.1	Brief Review of Earlier LINO Work	20
1.2.2	Brief History of This Work	21
1.3	Organization of This Thesis	23
2	The Hyperfine Interaction: Coupling the Nucleus and the Atomic Elec- trons	25
2.1	The Magnetic Dipole Energy: A Product of the Nuclear Magnetic Dipole Moment and the Electronic Magnetic Field	26
2.1.1	The Magnetic Field at the Nucleus Produced by the Atomic Electrons	27
2.1.2	The A Term: Relating the Magnetic Dipole Moment and the Elec- tronic Magnetic Field	29
2.2	The Quadrupole Energy: A Product of the Nuclear Quadrupole Moment and Electronic Field Gradient	31
2.2.1	The Electric Field Gradient at the Nucleus	31

2.2.2	The B term: What We Actually Measure	32
2.3	The ^{85m}Rb Hyperfine Energy Diagram	32
2.4	The Isotope Shift: Caused by Changes in the Nucleus	34
2.4.1	The Shift Caused by the Change in the Reduced Mass	35
2.4.2	The Shift Caused by a Change in the Coulombic Potential	36
2.4.3	Converting the Isotope Shift to a Change in the Mean Square Charge Radius	38
3	The Production of the Sub-Doppler Change Signal using LINO	40
3.1	Anisotropy through Optical Pumping	40
3.1.1	The Coupling Between Electronic States: The Electronic Dipole Transition	41
3.1.2	Population Transfer within Sub-Levels through Optical Pumping	43
3.1.3	The Excess Population in the Sub-Levels Causes an Anisotropic Pattern in the Gamma-ray Emission of the Isomer	49
3.2	Creating a Sub-Doppler Change Signal in the Anisotropy through Satura- tion Spectroscopy	53
3.2.1	One Laser Beam Creates a Doppler-Broadened Signal	54
3.2.2	The Counter-Propagating Beam Produces a Saturation Effect	62
3.2.3	The Difference Between the Two Anisotropies is the Change Signal	62
3.3	Velocity Changing Collisions Affect the Optical Pumping	64
3.3.1	Pumping With Many Vcc's Increases the Number of Atoms Pumped But Gives a Broad Signal	66
3.3.2	Pumping with Just a Few Vcc's Produces a Dip and Pedestal	68
4	The Experimental ^{85m}Rb Gas-Cell System	70
4.1	Isomer Production and Neutralization in a Cell System	70
4.1.1	Production of the Isomer	70
4.1.2	Neutralization of the Isomer	71

4.2	Modeling the System	74
4.2.1	The Mathmathical Model	76
4.2.2	Numerical Solution of the Model	79
4.2.3	Predictions of the Model	80
4.3	Cell Design and Optimization	80
4.3.1	Calculation of Signal-To-Noise	83
4.3.2	Dip Amplitude vs. Pressure	85
4.3.3	Absorption Effect on Average Intensity	85
4.3.4	Maximizing Signal-to-Noise	89
5	Experiment Results and Analysis	93
5.1	General Description and Experimental Arrangement	93
5.2	Experimental Apparatus	94
5.2.1	Cell-Gas System	94
5.2.2	Laser Frequency Location	96
5.2.3	Data Aquisition	98
5.3	Results	99
5.3.1	Doppler-Broadened One Laser Pumping	99
5.3.2	Sub-Doppler Experimental Results	103
5.3.3	D1 and D2 Summary Results	103
5.3.4	Determination of Uncertainty	106
5.4	Analysis of The Results	111
5.4.1	Determining the A terms, and the Magnetic Dipole Moment	111
5.4.2	Extraction of Electric Quadrupole Moment	114
5.4.3	Extraction of Isomer Shift Value	115
6	Discussion Of Nuclear Parameters	117
6.1	The Nuclear Shell Model	117
6.1.1	Brief Development of the Shell Model	118

6.1.2	The Extreme Single Particle Model	119
6.1.3	The Shell Model and ^{85m}Rb	121
6.1.4	The Shell Model: Single Particle Plus Core Collective Motion . .	121
6.2	Comparison of Observed Results to Single Particle Predictions.	123
6.2.1	The Source of the Nuclear Magnetic Dipole Moment: The Motion of the Nucleons	123
6.2.2	The Single Particle Quadrupole Moment	127
6.2.3	The Quadrupole Moment of a Deformed Nucleus	128
6.3	Deformation Parameter	130
6.3.1	The Methodology For Separating the Mean Square Radius into a Volume Change and a Deformation Change.	131
6.3.2	Calculation of the Deformation Parameter	132
6.4	Comparing the $9/2^+$ spin nuclei: ^{81m}Rb and ^{85m}Rb	135
7	Concluding Remarks	137
A	Matrix Elements of ^{85m}Rb	142
B	Publication	148
A	Hyperfine Structure of Natural Rubidium	154

List of Figures

1-1	Lifetimes accessible to different laser techniques	15
1-2	Short summary of radiation detection by optical pumping (RADOP). (From Shimkaveg.)	18
1-3	Decay scheme of ^{85}Kr , producing the $1 - \mu\text{s}$ isomer ^{85m}Rb	21
2-1	The nuclear magnetic dipole in the magnetic field of the electron.	27
2-2	The hyperfine energy diagram For ^{85m}Rb , showing the energy shift from the electronic J states due to the A and B terms.	33
2-3	The field shift is caused by changes in the nuclear radius from isotope to isotope. The change is produced by either a volume change or shape change.	37
3-1	Sub-level structure of $F=5$ ground state and first excited state $F'=4$ of ^{85m}Rb . Each F level is divided into $2F+1$ sub-levels. Matrix elements for absorption of linearly polarized light are shown between sub-levels.	42
3-2	Matrix elements for absorption for linearly polarized light from $F=4$ to $F'=4$ transition.	43
3-3	The matrix elements for decay from the $F'=4$ level.	44
3-4	Matrix elements for decay of an atom excited to $F'=4$, $M_F=4$ sub-level.	45
3-5	Population transfer to trapped $M_F = \pm 5$ levels. Excess population also produced in $F=4$ ground state, but does not contribute to anisotropy.	48
3-6	Radiation patterns produced by F, M_F sub-levels in gamma-ray decay of ^{85m}Rb . (Courtesy of Shimkaveg)	51

3-7	Total radiation pattern seen by detectors is the sum of the isotropic background due to equal populations in all sub-levels, and the anisotropic pattern due to excess in $M_F = \pm 5$ sub-levels.	52
3-8	A Doppler-broadened distribution is divided into different homogeneous velocity bins.	57
3-9	Optical pumping 3-level system digs a hole in the pumped level, and puts the excess population in the trapped level.	59
3-10	One beam optical pumping transfers population to trapped level. The resultant anisotropy, proportional to total excess number of atoms from all velocity groups, maps out Doppler profile.	61
3-11	Two-beam optical pumping. When laser is tuned to zero velocity group, less atoms are transferred to trapped level. The resulting dip is shown in the anisotropy profile.	63
3-12	The change signal is produced by the difference between two laser pumping and one laser pumping.	65
3-13	Effect of vcc's on laser optical pumping, with pump laser tuned to resonance. Buffer gas perturbers cause vcc's into and out of the resonant velocity bin (broken vertical lines). (From Quivers.)	67
3-14	The effect of vcc on population transfer to the trapped level. The case with noo vcc's just produces a homogeneous bump. The case with vcc's produces a bump and a pedestal.	69
4-1	Calculated average velocity of the neutral ^{85m}Rb isomers in the cell vs. Kr density and pressure for the two cases $a = +1$ and $a = -1/3$	75
4-2	Three level model for optical pumping the D1 $F=5$ to $F' = 4$ transition. .	77
4-3	Change signal at 300 mTorr predicted by numerical model as a function of average intensity. A single laser was used to optically pump sample. .	81
4-4	The change signal is decomposed into a Lorentzian dip and Gaussian pedestal, with the amplitude of each shown at various intensities.	82

4-5	Dip amplitude vs. pressure at various values of \bar{I}	86
4-6	Relative S/N vs. pressure for various values of \bar{I} . S/N in arbitrary units, pressure in mTorr.	87
5-1	Schematic diagram showing experimental arrangement.	95
5-2	Single laser Doppler-broadened results on the low energy ^{85}Rb D1 tran- sitions using original 4 Torr cell with 300 mW of power. Frequency is reference to ^{87}Rb $F=2$ to $F'=1$ transition.	100
5-3	Single laser Doppler-broadened results on the high energy ^{85}Rb D1 tran- sitions using original 4 Torr cell with 300 mW. Frequency is reference to ^{87}Rb $F=1$ to $F'=2$ transition.	101
5-4	Initial sub-Doppler change signal produced by single laser optical pumping with 300 mW on $F=5$ $S_{1/2}$ to $F'=4$ $P_{1/2}$ transition. Cell pressure is at 300mTorr. Solid line is a least-square fit to a Lorentzian and Doppler composite curve. Frequency is reference to peak location. Dashed line is signal by our model.	104
5-5	Observed gamma ray change signal for ^{85}Rb D1 $F=5$ to $F'=4$ ^{85}Rb transition. Transition pumped with 300 mW total power, at cell pressure of 300 mTorr. Frequency measurement is made reference to ^{87}Rb $F=2$ to $F'=1$ transition	107
5-6	Observed gamma ray change signal for ^{85}Rb D1 $F=4$ to $F'=5$ ^{85}Rb transition. Transition pumped with 300 mW total power, at cell pressure of 300 mTorr. Frequency measurement is made with reference to ^{87}Rb $F=1$ to $F'=2$ transition	108
5-7	Observed gamma ray change signal for ^{85}Rb low energy D2 transitions. Transition pumped with 550 mW total power, at cell pressure of 300 mTorr. From higher to lower frequency, the $F=5$ to $F'=6$ transition, the 6 to 5 crossover, and the $F=5$ to $F'=4$ transition. Frequency mea- surements made with reference to ^{87}Rb $F=2$ to $F'=1$ transition.	109

5-8	Relative frequency location of all measured transitions of ^{85m}Rb	110
6-1	Single Particles States with Spin Orbit Splitting.	120
6-2	Ground state and low-lying excited states of ^{85}Rb	122

List of Tables

5.1	Single Laser Optical Pumping on the D1 with Doppler broadened transitions contrasted with two-laser pumping (from Shimkaveg)	102
5.2	Results of measurements on the D1 and D2 transitions. Measurements are made with reference ^{87}Rb transitions, and given with regard to calculated ^{85}Rb line center.	105
6.1	Comparison of single particle magnetic dipole moment values to actual observed values for several $n/2$ isotopes of Rb.	126
6.2	Comparison of single particle quadrupole values with actual observed values.	129
6.3	Comparison of quadrupole and isomer shift deformation parameters for several isotopes of rubidium. All values from Thibault except that of ^{85m}Rb measured in this work.	134
6.4	Comparison of ^{85m}Rb and ^{81m}Rb along with ground states.	135

Chapter 1

Introduction and Overview

The work described in this thesis is the culmination of a program begun in 1975 at the George R. Harrison Spectroscopy Laboratory to incorporate laser spectroscopy and its techniques into the field of nuclear physics using laser optical pumping. This technique, which is used to orient nuclei via the hyperfine interaction, is known as Laser Induced Nuclear Orientation (LINO). If the oriented nuclei are unstable, the resultant nuclear decay produces an anisotropy in the otherwise isotropic radiation decay pattern. This anisotropy, produced by the hyperfine resonance absorption, yields information about the nucleus.

Prior to this work, the anisotropic radiation signals produced in a gas-cell system were of Doppler width (approximately 360 MHz at the $1/e$ half width at 160°C , the temperature of our previous experiment with rubidium). This signal, while narrow enough in certain cases to allow for resolving the hyperfine resonances, in other cases is too broad to allow resolution. This indeed was the case for $^{85\text{m}}\text{Rb}$, the $1\text{-}\mu\text{s}$ isomer which was the focus of our prior work, where the inability to resolve the D2 transitions prevented a measurement of the quadrupole moment. This limited the usefulness of the LINO technique. Our goal was simple: to develop a technique using LINO that produced a narrow resonance anisotropic signal, and demonstrate the usefulness of the technique by measuring something that could not otherwise be measured optically, such as the quadrupole

moment of ^{85m}Rb . This thesis describes the successful accomplishment of that goal.

1.1 The Study of Short-Lived Nuclei: Why and How

The study of short-lived isomers is important because it can yield information about nuclei otherwise not available. For example, the measurement of the quadrupole moments of the 8 isomeric states ^{199m}Hg - ^{185m}Hg by the Mainz group led to the idea that the occupation number of a sub-shell and the type of coupling might be as important as the intrinsic deformation [22]. However, because short-lived isomers by their very definition do not last very long, they can be difficult to study.

There are methods to study nuclei, both optically and non-optically. As we are dealing in this work with optical measurements using lasers, we shall review briefly some of the techniques available. The discussion follows Feld[21], and his talk "Lasers in Nuclear Physics" at the 1982 conference by the same name.

There are several methods available for the study of radioactive nuclei using the hyperfine structure, and they can be categorized by the method in which they detect the signal. The three signal detection methods are detection of optical photons, detection of atoms or ions, and detection of nuclear radiation. These methods, and the lifetimes accessible to study by them are shown in Fig. 1.1.

1.1.1 Techniques Based on the Detection of Optical Photons

The detection of optical photons includes several specialized techniques. One technique is laser-excited fluorescence in a cell. In this technique the sample from a mass-separated beam is collected on a foil, moved quickly into a cell, and heated. As the laser is tuned through the hyperfine resonances, the fluorescence will peak. This technique has been used to study several isotopes of Hg [29]. A narrow resonance signal can be achieved here using saturation spectroscopy [22]. The technique is limited to relatively long-lived

LIFETIMES ACCESSIBLE TO OPTICAL MEASUREMENT TECHNIQUES

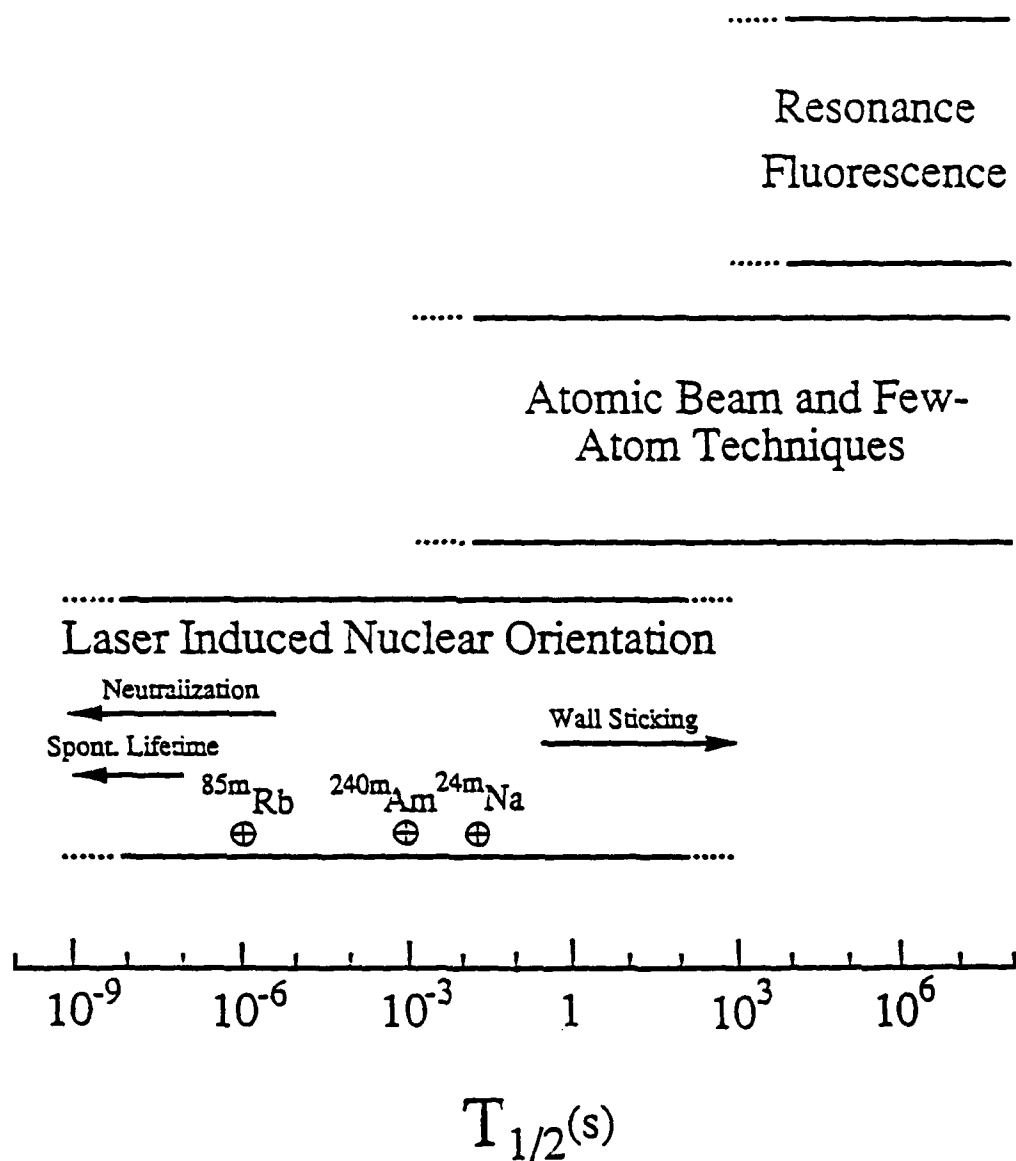


Figure 1-1: Lifetimes accessible to different laser techniques

species ($\tau \sim$ minutes) and relatively high densities. Other techniques rely on atomic beams produced in an accelerator, neutralized, and then optically pumped. For example, atomic beams have been used to study several radioactive isotopes of Ba [30, 31]. The lifetime limitation in these beam experiments is the transit time through the system, requiring a half-life of ≥ 10 ms. Atomic beam fluorescence produces a sub-Doppler signal by using laser radiation at right angles to the beam to access the narrow transverse velocity profile. The resulting fluorescence is then examined. Another beam technique, kinematic velocity compression in a fast atomic beam, produces a narrow resonance signal using a co-propagating (rather than transverse) laser beam in conjunction with a fast atomic beam. The atoms in the beam, accelerated as ions and then neutralized, have their Doppler width reduced by a factor u/v_a , where u is the thermal velocity and v_a is the velocity of the ions in the accelerated beam. This technique has been used by the Otten group to study Rb at Mainz [32]. A major problem with fluorescence techniques is the high background optical radiation, which may greatly diminish the signal.

1.1.2 Techniques Based on Detection of Atoms and Ions

Techniques based on atom or ion detection are generally more sensitive than those detecting optical photons because the background signal is usually much less. A particularly useful technique is the atomic beam laser optical pumping with magnetic detection which produces sub-Doppler signals in the same fashion as atomic beam fluorescence, but has a higher sensitivity since it detects the atoms themselves. Radioactive atoms are produced on line by spallation, fission, or fragmentation reactions and then collected in a vessel where they are neutralized and thermalized. They exit through a diaphragm to form an atomic beam. The beam is irradiated transversely by the laser in the region of a weak magnetic field. The equilibrium populations of the sub-levels in the ground state are altered due to this optical pumping. The beam then enters a strong magnetic field, where the nuclear spin and electronic angular momentum are decoupled, forming two groups of Zeeman levels with $M_J = \pm 1/2$. The field gradient is designed to focus only

one component onto a detector. The detector is a hot tungsten tube, which ionizes the beam as it passes through. The ions are then mass-separated and counted by an electron multiplier. Optical resonances are then observed by either a depletion or increase in the number of counts produced on resonance. This technique has been used by Thibault [19] to study an entire chain of rubidium isotopes and isomers. We have used information from that experiment to help analyze our results.

1.1.3 Methods Detecting Nuclear Radiation: RADOP

The most sensitive technique, and the one which is the main focus of this thesis, is RADOP (RAdiation Detection by Optical Pumping) developed by the Mainz group and used on radioactive isotopes of Hg, Au, and Cd [22]. It is this work that produced the unexpected nuclear shape deformation in the light Hg isotopes mentioned earlier. This technique was developed and applied by J. Bonn, G. Huber, H. J. Kluge and E.W. Otten. The original work was done with an optical lamp as a pump source, with later work done using a laser. The advantage of the technique is its sensitivity, allowing the measurements of very short-lived nuclei. Shimkaveg has summarized the work done using this technique [6]. The results are shown in Fig 1.2. As the figure shows, the technique can be used on line or off line, which means at an accelerator facility or away from one. The techniques have used different types of radiation; gamma radiation, β radiation, and fission fragments. The advantage of doing the experiment on line is that the short-lived nuclei are produced right there, and that several nuclei can be measured. The problem is usually the background radiation, and the time it takes to acquire a statistically significant signal.

The advantage of off line work is obvious; no accelerator is needed. This keeps the cost down significantly. The problem of excessive background radiation is also avoided. However, constructing an off line system introduces its own problems, some of which limit the applicability of the technique quite a bit.

The first problem is finding a suitable parent-daughter system. Normally, the parent

Year	Species ($T_{1/2}$)	Light Source	Accelerator Facility	Signal Form and Magnitude	Count Rate
1967-1976	alkalies, e.g. ^{37}K (12 s)	lamp	cyclotron, 7 MeV	β , 0.1-1%	$\sim 1000/\text{s}$
	mercury, e.g. $^{199\text{m}}\text{Hg}$ (43 m)	lamp	ISOLDE	γ (E2) 2.8% (M4) 35%	1500/s 150/s
1973	^{203}Hg (47 d)	lamp	none	γ , 3%	420/s
1979	$^{240\text{m}}\text{Am}$ (1 ms)	broadband dye laser	cyclotron, 49 MeV	fission fragment, 33%	40/hr
1979	$^{24\text{m}}\text{Na}$ (20 ms)	single-mode dye laser	Van de Graaf, 2.5 MeV	γ , 0.5%	300/s
1984	$^{85\text{m}}\text{Rb}$ (1 μs)	2 single-mode ring dye lasers	none	γ , 2%	1000/s

Figure 1-2: Short summary of radiation detection by optical pumping (RADOP). (From Shimkaveg.)

is a relatively long-lived nucleus that produces a daughter and other decay products. The daughter must live long enough to be neutralized (if it is an ion) and optically pumped many times to produce a significant population transfer to some Zeeman sub-level (optical pumping is discussed in chapter 3). This greatly limits the possible number of systems that can be studied. The parent must be one that does not stick to the wall of the cell, or else it becomes difficult to optically pump. This usually leads to the choice of a noble gas for a parent (such as ^{85}Kr in our case).

The neutralization of the daughter can be difficult also. While it is advantageous to use a stable isotope of the isomer being examined to provide resonant charge exchange, the stable isotope can absorb much of the pumping light, affecting the signal generation. Spin exchange with the stable isotope can also lead to a loss of signal. So, it is not an easy system to design. Additionally, unless one has chosen a particularly clever system, only one isomer can be studied per cell. Usually information from a whole chain of isotopes is used to draw some significant conclusion about nuclear structure. However, if it is a particularly interesting isomer, it may justify study by itself.

Prior to this work, a major disadvantage was the Doppler width signals produced in the gas-cell system. We have eliminated that disadvantage and increased the precision of the experiment by an order of magnitude, allowing us to measure for the first time the quadrupole moment of the isomer. A further complication in the original experiment was the need for two lasers to excite both ground state levels to achieve significant population transfer. We have shown that it is possible to achieve significant population transfer with only one laser, greatly simplifying the experiment. However, we pay a price for this in terms of counting time, which increases by an order of magnitude.

1.2 Brief Review of the MIT LINO Project: Successful Development of the ^{85m}Rb Gas-Cell System

As mentioned above, this work builds on the earlier efforts of many people, and in particular the previous Ph.D. students on the project, Drs. Burns, Pappas, Quivers, and Shimkaveg. Their work is summarized in the following section.

1.2.1 Brief Review of Earlier LINO Work

Dr. Burns did the initial work on the effects of optical pumping, both on laser saturation spectroscopy and on laser induced nuclear orientation. In laser saturation spectroscopy, he observed experimentally and explained theoretically three effects: (1) anomalous structure; (2) reduced saturation threshold; and (3) very narrow linewidths. He recorded the initial observation of LINO, as manifested in anisotropic gamma emission, in both ^{22}Na and ^{24m}Na , providing a preliminary value for the isomer shift in the latter [26]. Dr. Pappas continued this work, achieving nuclear polarization of 90% in ^{23}Na , using velocity changing collisions as a method to increase the pumping efficiency. He also observed gamma anisotropy in ^{24m}Na , deriving a value for the magnetic dipole moment, and the isomer shift [17].

Dr. Quivers developed a theoretical model of optical pumping with velocity changing collisions, describing quantitatively the creation of the Doppler pedestal and Lorentzian dip later demonstrated experimentally for ^{85m}Rb in this work. It is his model we used to successfully predict our results [16].

Subsequently, Dr. Shimkaveg and his colleagues successfully developed a gas-cell system that produced gamma anisotropy in the decay of the 1- μs isomer ^{85m}Rb , which has spin $9/2^+$ and is the 514 KeV isomeric state of ^{85}Rb . The isomer ^{85m}Rb was produced from the β^- decay of ^{85}Kr , enhanced to 30% in a sample of natural Kr. The decay scheme

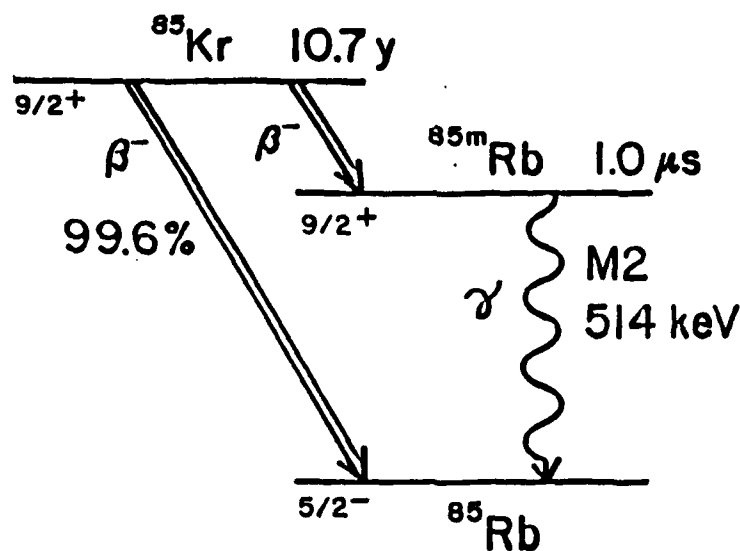


Figure 1-3: Decay scheme of ^{85}Kr , producing the 1 - μs isomer $^{85\text{m}}\text{Rb}$.

is shown in Fig. 1.3. The isomer was neutralized using natural rubidium, consisting of 72% ^{85}Rb and 28% ^{87}Rb , at a temperature of 160°C. The isomer was pumped near the D1 line (794.7 nm) and the D2 line (780 nm), producing Doppler broadened anisotropic signals.

1.2.2 Brief History of This Work

The precision of Dr. Shimkaveg's work was limited by two factors, (1) the Doppler width of the anisotropy signal, and (2) the shift of the signal's line center due to absorption of the pump light by natural rubidium in the cell. The uncertainties in the location of the transitions were approximately ± 60 MHz.

Although this did not prevent him from obtaining an accurate value for the magnetic dipole moment, as the ground state splitting is large and the transitions are well resolved, it did prevent him from getting an accurate value for the isomer shift. It also prevented him from obtaining a value for the hyperfine B value, as the expected contribution from this term to the energy splitting in the D2 was roughly the same as the uncertainty in those splittings. Additionally, the D2 Doppler broadened transitions overlap, making the

resolution of any measurement difficult. The need for a sub-Doppler technique apparent, Dr. Shimkaveg and his colleagues attempted a sub-Doppler measurement using the ^{85}Rb gas-cell system at cell pressures of 450, 300, and 80 mTorr of ^{85}Kr . Using two lasers, as was done throughout his Doppler broadened work, they fixed one laser on a chosen hyperfine transition frequency. The second laser, tuned to a different transition, was moved across the Doppler profile of that transition, and data taken at different locations. When the two lasers pumped the same velocity group, they expected a sub-Doppler anisotropic signal to be produced. The results were quite inconclusive. (For discussion of the underlining theory see [6][pgs. 106-110].)

When I joined the group in 1986, the experiment was being attempted again, using the same technique, but larger cells. The larger cells contained more radioactive gas, and thus it was felt that they would produce a higher signal-to-noise than the smaller cells. The results were also quite disappointing, as no sub-Doppler signal was obtained after a tremendous amount of effort. Following Prof. Feld's guidance, Dr. Hutton and I, using Dr. Quiver's theoretical model, wrote a computer program that described the behavior of the system. This model predicted success, but only using the much smaller cells originally designed by Dr. Shimkaveg.

In fact, the model predicted that Dr. Shimkaveg's experiment should have worked. There are several possible reasons why the experiment didn't work. The precision in locating the laser frequency may have been overestimated in the first experiment, thereby causing significant broadening of the observed results. (Our precision was greatly enhanced by the use of the Autoscan system, described in chapter 5.) The relative drift between the two laser may have also been excessive, producing a very broad signal. (This problem is eliminated by using only one laser.) The power available may have been inadequate. (We had over twice the power in our experiment from the Coherent laser.) Additionally, the data taken in his experiment is probably inadequate to analyze the results. It may be that there is a sub-Doppler signal sitting on top of a Doppler pedestal in his work. It is not possible from the observed data to draw any conclusions.

However, while trying to replicate Dr. Shimkaveg's experimental results with our computer model in the high pressure limit, we observed an interesting fact: one laser was producing the bulk of the anisotropic signal. The model actually predicted that we could replicate Dr. Shimkaveg's work with only one laser. Obviously, we were quite skeptical about this, as we assumed that the second laser was necessary to re-distribute lost population back into the pumping cycle in order to produce any significant anisotropy. (The reason why this not necessary is explained in chapter 3.) However, we decided to attempt the Doppler broadened experiment with one laser, just to assure ourselves that the model was incorrect in this regard. Actually, it was correct, and we were able to replicate Dr. Shimkaveg's results, for the most part. (There is a difference when pumping with one laser vs. two, and the difference is transition dependent. This also is explained in chapter 3.)

Once we realized that we could pump with one laser, the idea of using standing wave saturation followed quickly. Prof. Holbrow, visiting with us for a year from Colgate University, had re-written our computer program using a Gauss-Jordan technique, which was quite a bit more efficient than our original program. We asked him to modify the program to account for standing wave saturation, and to predict the results of the experiment. His program predicted success. We therefore ran the experiment, and the results are described in this thesis.

1.3 Organization of This Thesis

The thesis is organized going from the general to the specific. In chapter 2 the hyperfine interaction which couples the atomic and nuclear parameters is discussed. The theory of the sub-Doppler change signal in the low pressure limit is presented in chapter 3. Chapter 4 shows how we model the system, including the recoil effect of the β decay on the daughter and the background absorption of light by the natural rubidium. We present the predictions of our model, and an analysis of the signal-to-noise produced as a function

of counting time. Chapter 5 presents the experimental data, and shows how we extract the hyperfine A and B terms, with their associated moments, as well as the isomer shift. Chapter 6 looks at the nuclear information extracted using the single particle model to see if the isomer behaves differently from the ground state. Additionally, we look at the behavior of the isomer with reference to both its ground state and the other $9/2^+$ Rb isomer, ^{81m}Rb , to see if the behavior is very much different, or if the single particle spin state is the determining factor in the nuclear behavior. In chapter 7, we present our conclusion.

Chapter 2

The Hyperfine Interaction: Coupling the Nucleus and the Atomic Electrons

The study of isomers is hindered by the lack of a means to optically excite a nucleus from the ground state to an upper state, a situation that will remain that way until the gamma-ray laser is built (if ever). However, we can use the hyperfine coupling between the atomic electrons and the nucleus to affect the spatial distribution of the gamma-rays from the de-excitation of the ^{85m}Rb to the ground state of ^{85}Rb .

Although the total charge in the nucleus is the main determinant of the energy levels of the atomic electrons, the motion of the constituent nucleons and their charge distribution also affects these levels, causing very small or hyperfine splittings in optical spectra. These splittings provide physicists a window into the nucleus, and, through optical pumping a way to influence the nucleus. The hyperfine energy terms arise from the fact that the nucleus is not a point charge and is not truly spherical. Because the nucleus is not a point charge but is composed of neutrons and protons, the motion of the charged protons can produce a net current loop, and therefore a magnetic dipole moment. (This is discussed in Chapter 6.) Additionally, the protons and neutrons have their own intrinsic dipole

moments which can add together. This net dipole is then subject to a magnetic field produced by the motion (and intrinsic spin) of the atomic electrons, and the resulting energy term. Because it is not truly spherical the charge distribution of the protons can give rise to a quadrupole (and higher) moment. This moment is subject to a electric field gradient produced by the atomic electrons, and therefore produces a change in the energy. Because different nuclei with the same charge can have different numbers of neutrons (isotopes), they can have different volumes and shapes. These differences correspond to energy differences or shifts between the isotopes. Finally, even the same nucleus when excited to a higher nuclear energy level can have a different shape, producing a change in energy or isomer shift. The hyperfine energy terms can be written

$$E_{Hyperfine} = E_{Dipole} + E_{Quadrupole} + \delta E_{Isotope\ shift} \quad (2.1)$$

This section deals with these energies, how these are produced, and what we actually measure.

2.1 The Magnetic Dipole Energy: A Product of the Nuclear Magnetic Dipole Moment and the Electronic Magnetic Field

The Hamiltonian of a magnetic dipole in a magnetic field can be written

$$H_{Dipole} = -\vec{M} \cdot \vec{B}_J \quad (2.2)$$

and is a product of the nuclear magnetic dipole due to the motion of the nuclei and the magnetic field caused by the motion of the electrons. The nuclear dipole in the electronic magnetic field is illustrated at Fig. 2.1.

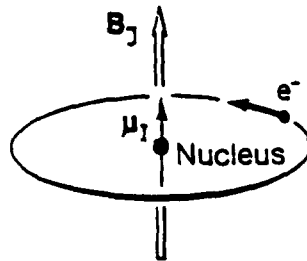


Figure 2-1: The nuclear magnetic dipole in the magnetic field of the electron.

2.1.1 The Magnetic Field at the Nucleus Produced by the Atomic Electrons

It is a well-known fact that a current moving in a loop produces a magnetic field which can be described by Maxwell's equations. An electron, which is a charged particle, classically orbits the nucleus and therefore will produce a magnetic field. Additionally, because the electron has intrinsic angular momentum associated with it, there is a contribution to the magnetic field from the electron's spin.

The field produced at the nucleus by the orbital motion of the electrons is the vectoral sum of the fields produced by the individual electrons, and can be written in terms of their individual orbital angular momentum as

$$\vec{B}_l = \frac{-e}{c} \sum_i \frac{\vec{v}_i \times (-\vec{r}_i)}{r_i^3} = -\frac{e\hbar}{mc} \sum_i \frac{\vec{l}_i}{r_i^3} \quad (2.3)$$

or

$$\vec{B}_l = -2\mu_B \sum_i \frac{\vec{l}_i}{r_i^3} \quad (2.4)$$

where l_i is the orbital angular momentum of the i th electron measured in units of \hbar ,

and μ_B is the Bohr magneton ($e\hbar/2mc$). The field contribution due to the spin of the individual electrons at the nucleus is

$$\vec{B}_s = \sum_i -\frac{2\mu_B}{r_i^3} (3 \frac{\vec{r}_i \cdot \vec{s}_i}{r_i^2} - \vec{s}_i). \quad (2.5)$$

The total field is the sum of the two contributions and can be written

$$\vec{B} = \sum_i -\frac{2\mu_B}{r_i^3} (\vec{l}_i - \vec{s}_i + 3 \frac{\vec{r}_i \cdot \vec{s}_i}{r_i^2} \vec{r}_i). \quad (2.6)$$

The magnetic field above is valid for the electrons outside the nucleus. For the case of the s electron (and relativistically the p electron) this is not true. However, it can still be treated classically as done by Armstrong [7]. If we assume that the nucleus is a sphere with uniform spin density throughout the volume, then there will be a uniform magnetization of $\vec{M} = -2\mu_B |\psi_0|^2 \vec{s}$, where ψ_0 is the wave function at the center of the nucleus, $r = 0$. Inside a sphere of uniform magnetization \vec{M} is a field $\vec{B} = (8\pi/3)\vec{M}$, with no magnetic field outside due to the s electron because of spherical symmetry of the electron density. Therefore, the s electron produces a field

$$\vec{B} = -\frac{16\pi}{3} \mu_B |\psi_0|^2 \vec{s} \quad (2.7)$$

at the nucleus. This field can be calculated using an approximate value for the wave function.

Segré list the values for the B_J field of rubidium for the different states [2, page 259, table 6-5]: for the $^2S_{1/2}$ state, $B = 1.3 \times 10^6$ G; for the $^2P_{1/2}$ state, $B = 1.6 \times 10^5$ G; and for the $^2P_{3/2}$ state, $B = 8.6 \times 10^4$ G. From these values it is clear that the electronic ground state of rubidium, which is an s state, will have a much larger energy splitting than the excited states.

2.1.2 The A Term: Relating the Magnetic Dipole Moment and the Electronic Magnetic Field

What we actually measure spectroscopically are energy splittings. However, knowing the angular momentum states of the transition levels allows us to extract the hyperfine A term. The A term is related to the product of the magnetic dipole moment and the electronic B_J , as shown in this section.

We can rewrite the magnetic dipole moment operator in terms of the angular momentum of the nucleus,

$$\vec{M} = \gamma \hbar \vec{I} = g_I \mu_N \vec{I} = \frac{\mu}{I} \vec{I} \quad (2.8)$$

where γ is the gyromagnetic ratio, g_I is the nuclear g factor, and μ_N is the nuclear Bohr magneton ($e\hbar/2m_p c$) with m_p the mass of the proton.

We can also rewrite the magnetic field in terms of the total electronic angular momentum

$$\vec{B}_J = \frac{B_J}{J} \vec{J} \quad (2.9)$$

so that the Hamiltonian term is

$$H_{Dipole} = \frac{\mu B_J}{IJ} \vec{I} \cdot \vec{J}. \quad (2.10)$$

Since the total angular momentum of the atom can be written

$$\vec{F} = \vec{I} + \vec{J} \quad (2.11)$$

then the $\vec{I} \cdot \vec{J}$ can be written

$$\vec{I} \cdot \vec{J} = \frac{1}{2}(F^2 - I^2 - J^2). \quad (2.12)$$

The expectation value using the quantum mechanical operators \vec{F} , \vec{I} , and \vec{J} is

$$\langle FM_F | F^2 - I^2 - J^2 | FM_F \rangle = [F(F+1) - I(I+1) - J(J+1)]\hbar^2. \quad (2.13)$$

We can then write the energy term as

$$E_{Dipole} = \frac{A}{2}[F(F+1) - I(I+1) - J(J+1)] \quad (2.14)$$

or

$$E_{Dipole} = \frac{AC}{2} \quad (2.15)$$

where

$$A = \frac{\mu B_J}{IJ} \quad (2.16)$$

and

$$C = [F(F+1) - I(I+1) - J(J+1)]. \quad (2.17)$$

From this development, it is clear that the A term is a product of the magnetic dipole moment of the nucleus and the magnetic field of the atomic electrons. Since it is the A term that we measure optically, we cannot determine precisely what either μ or B_J are, only their product. If, however, we have an independent measure of μ , perhaps from a scattering experiment, we can extract the value of B_J . Assuming that the electronic B_J remains the same, this field can then be used to extract the magnetic dipole moment for other isotopes, although one may have to correct for the change in the spatial distribution of the magnetic dipole moment (see 5.4.1).

2.2 The Quadrupole Energy: A Product of the Nuclear Quadrupole Moment and Electronic Field Gradient

The quadrupole moment arises from the non-spherical charge distribution within the nucleus. This quadrupole moment sees a gradient in the electric field produced by the atomic electrons, so again the energy term is coupled.

2.2.1 The Electric Field Gradient at the Nucleus

Just as the electrons produce a B_J field that affects the magnetic dipole moment, they also produce a gradient in the electric field at the nucleus, affecting the quadrupole moment.

The potential seen at the nucleus due to the electrons is

$$\phi_e(0) = \int \frac{\rho_e(r_e)}{r_e} d\tau_e \quad (2.18)$$

where $\rho_e(r_e)$ represents the electronic charge density, and the origin is taken at the center of the nucleus. Then the z component of the electric field at the origin can be written as

$$E_z = -\frac{\partial \phi_e}{\partial z} = -\int \frac{\rho_e(r_e)}{r_e^3} z_e d\tau_e \quad (2.19)$$

So, then the gradient of the electric field along z is

$$\frac{\partial E_z}{\partial z} = -\int \frac{\rho_e(r_e)}{r_e^3} (3z_e^2 - r_e^2) d\tau_e. \quad (2.20)$$

This integral can be evaluated since the electronic charge density is proportional to the wavefunction. However, just as can be done in the case of the magnetic dipole moment, if the quadrupole moment is known from nuclear scattering experiments, then the electric

field gradient can be extracted. Once extracted, and assuming again that the electronic factors remain unchanged from isotope to isotope, this value can be used to determine the quadrupole moment for other isotopes.

2.2.2 The B term: What We Actually Measure

The energy due to the quadrupole interaction can be treated in a fashion similar to the treatment provided the magnetic dipole energy term, although it is more complex (see [8, pages 377-379] or [2, pages 251-253]). We will simply quote the result here

$$E_{\text{Quadrupole}} = \frac{B}{4} \frac{\frac{3}{2}C(C+1) - 2I(I+1)J(J+1)}{I(2I-1)J(2J-1)} \quad (2.21)$$

where

$$B = eQ \frac{\partial E_z}{\partial z} = eQ \frac{\partial^2 V}{\partial z^2}. \quad (2.22)$$

The B term is nonzero only if $J > \frac{1}{2}$.

2.3 The ^{85}Rb Hyperfine Energy Diagram

We have seen that it is the product of the atomic and nuclear terms that produce the hyperfine structure. From the preceding discussion, we can construct a hyperfine energy diagram using the hyperfine A and B terms. Knowing the relationship between the energy splittings allows us to use the actual measurements to determine these terms. Once we know these hyperfine terms, we can extract the nuclear moments.

The hyperfine energy diagram is shown in Fig 2.2.

Also, from the above equations, it is easy to see that the energy difference between two F levels can be written

$$\Delta E_F = E_F - E_{F-1} = AF + B \frac{3F[2F^2 - I(I+1) - 2J(J+1) + 1]}{4I(2I-1)J(2J-1)}. \quad (2.23)$$

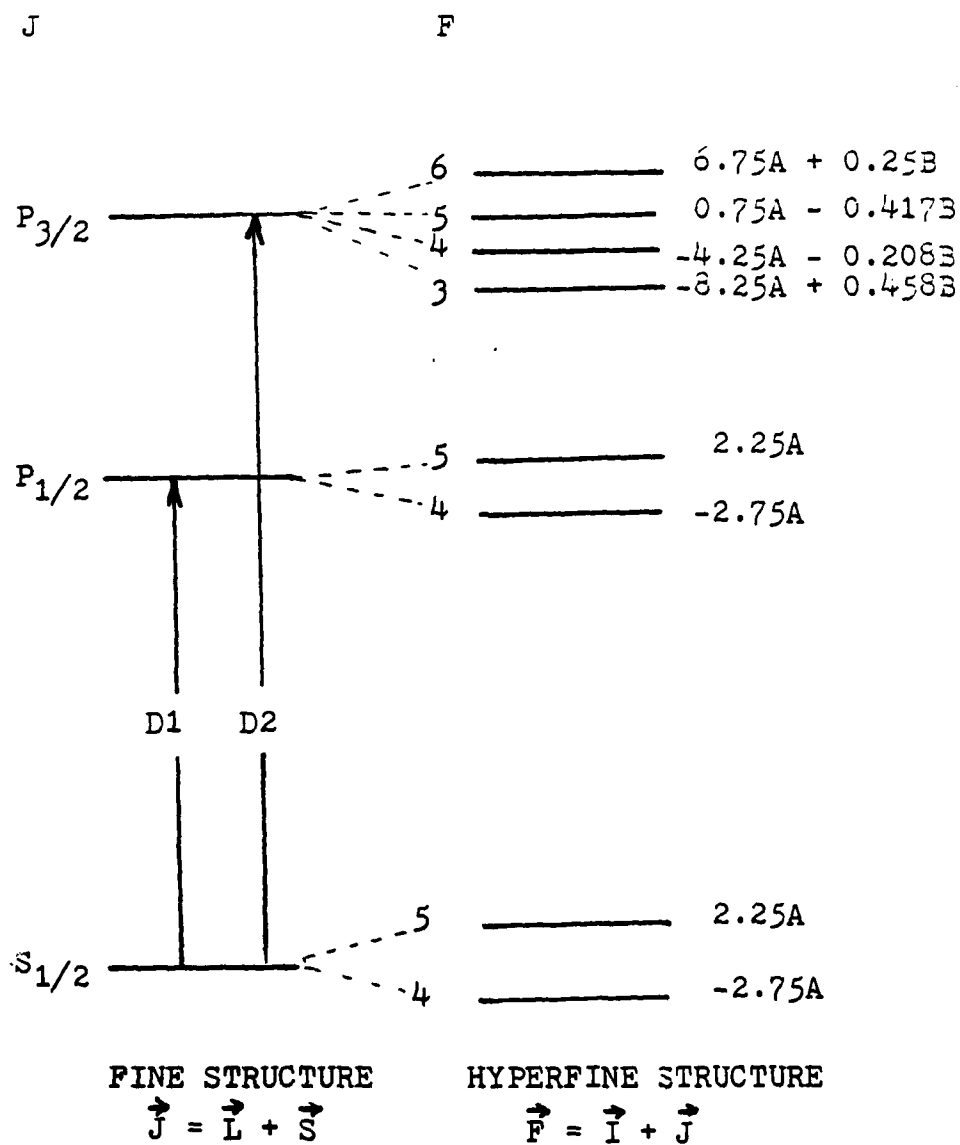


Figure 2-2: The hyperfine energy diagram For ^{85m}Rb , showing the energy shift from the electronic J states due to the A and B terms.

If $I = 1/2$ or $J = 1/2$, then $B = 0$ and the only contribution is from the A term, making the splitting easier to interpret. This splitting

$$\Delta E_F = AF \quad (2.24)$$

forms the ladder interval rule since each successive rung in the ladder is in increments of A . This is the case in rubidium for the $D1$ transitions, where the transition is from a $J = 1/2$ to a $J = 1/2$ state. The $D2$ transitions, from a $J = 1/2$ to a $J = 3/2$ state, involve both A and B terms. The B term can then be used to extract a value for the quadrupole moment (see 5.4.2). Dr. Shimkaveg estimated that the B term would be about 35 MHz [6][page 89] in ^{85m}Rb , so that the Doppler broadened anisotropic signals from the $D2$ transitions would overlap, preventing a measurement of the B term. The inability to resolve these splitting, and therefore the inability to measure the quadrupole moment, are why we decided to develop a sub-Doppler system.

2.4 The Isotope Shift: Caused by Changes in the Nucleus

Our work provides a direct measure of the isotope shift of ^{85m}Rb . There are two components to the isotope shift, the mass shift and the field shift. The mass shift is due to the different nuclear masses between isotopes and the field shift is due to changes in the coulombic potential produced within the nucleus by size or shape changes. We present a brief description of both terms. The isotope shift is often given in terms of a change in the mean square radius of the nucleus, so we show how the isotope shift can be converted to a change in the mean square radius.

2.4.1 The Shift Caused by the Change in the Reduced Mass

The mass shift is also divided into two components; (1) the normal mass shift and (2) the specific mass shift. The normal mass shift is also called the Bohr shift or reduced mass effect. In the solution to the hydrogen atom using the Schrodinger equation the reduced mass is introduced in the center of mass coordinate system as

$$\mu = \frac{m_e M}{m_e + M} \quad (2.25)$$

where m_e is the mass of the electron and M is the nuclear mass. The kinetic energy is then $p^2/2\mu$. It is clear that if the mass of the nucleus is changed, then the reduced mass is also changed, and a shift in the energy levels will occur. The shift for single electron atoms can be expressed as [4]

$$\frac{\nu_H - \nu_L}{\nu_H} = \frac{m_e(M_H - M_L)}{M_L(M_H + M_e)} \quad (2.26)$$

where the subscripts H and L stand for heavy and light respectively. For example, the shift between ^{87}Rb and ^{85}Rb is 57.025 MHz, or 75% of the total observed isotope shift.

If in two electron atoms there is a correlation between the electrons, then the energy shift is not merely the sum of two one electron shifts, but has an interaction term, called the specific mass shift (SMS). This term is normally small compared to the normal mass shift and is treated as a perturbation to the same shift. The specific mass shift has been found to be negligible experimentally for the rubidium isotopes [19].

Since the mass does not change between an isomer and the ground state, there is no mass shift. However, there is a field shift.

2.4.2 The Shift Caused by a Change in the Coulombic Potential

The field shift involves the electrostatic interaction between the atomic electrons and the nucleus. There are two sources of a field shift; (1) the volume change of the nucleus and (2) the shape change of the nucleus. The field shift can be understood in the following fashion: the Coulomb potential seen by an electron outside the nucleus is just $V_c = -Ze/r$. However, if the electron penetrates the nucleus, as does an s electron (and to a much smaller degree, a relativistic p electron), the potential within the nucleus (V_N) is different than that outside, and depends on the volume and shape of the charge distribution. This is illustrated in Fig. 2.3.

The change in energy can be written

$$\Delta E = e \int_0^{r_0} \psi^2(r) (V_N - V_c) 4\pi r^2 dr. \quad (2.27)$$

The wavefunction varies very little across the nucleus, so it can be removed from the integral, leaving

$$\Delta E = e |\psi_0|^2 \int_0^{r_0} (V_N - V_c) 4\pi r^2 dr. \quad (2.28)$$

The integral can be transformed [27][page 496] to an expression containing the mean square charge radius

$$\Delta E = \frac{2}{3} \pi |\psi_0|^2 Ze^2 \langle r^2 \rangle \quad (2.29)$$

where the mean square charge radius is

$$\langle r^2 \rangle = \frac{1}{Ze} \int \rho(r) r^2 dV \quad (2.30)$$

where Ze is the total nuclear charge and ρ is the nuclear charge density.

The energy shift is then related directly to the mean square charge radius.

ISOTOPE SHIFT

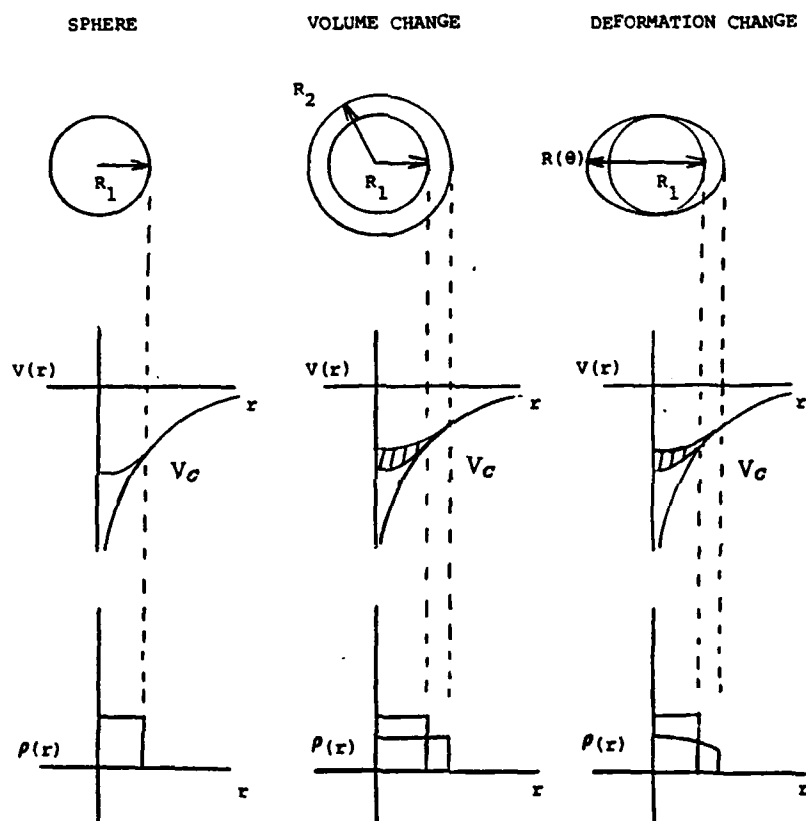


Figure 2-3: The field shift is caused by changes in the nuclear radius from isotope to isotope. The change is produced by either a volume change or shape change.

2.4.3 Converting the Isotope Shift to a Change in the Mean Square Charge Radius

The energy shift between isotopes due to changes in the coulombic potential can be written

$$\delta(\Delta E_1 - \Delta E_2) = \frac{2}{3}\pi |\psi_0|^2 Ze^2 \delta\langle r^2 \rangle \quad (2.31)$$

so that shifts in energy between isotopes can be directly related to changes in the mean square radius.

For rubidium, the expression above is modified to include both screening and relativistic effects and is written

$$\delta E = \pi\beta_s |\psi_0|^2 \frac{a_0^3}{Z} f(Z) \delta\langle r^2 \rangle \quad (2.32)$$

where the electronic factors are the $|\psi_0|^2$, the Bohr radius (a_0) and β_s , the screening factor due to the other electrons in the atom. The nuclear factors are $f(Z)$ and $\delta\langle r^2 \rangle$. The nuclear quantity

$$f(Z)\delta\langle r^2 \rangle = C \quad (2.33)$$

is normally called the isotope shift constant, and the electronic quantity is

$$\pi\beta_s |\psi(0)|^2 \frac{a_0^3}{Z} = F, \quad (2.34)$$

so that the shift can be written

$$\delta E = FC. \quad (2.35)$$

For our application, however, the relationship is best given in terms of frequency and mean square charge radius as

$$\delta\nu = \frac{F}{h} f(Z) \delta\langle r^2 \rangle \quad (2.36)$$

which relates the measured isotope shift to the change in the mean square charge radius.

Thibault gives the nonrelativistic value for the 5s electron at the nucleus extracted

from a measurement of ^{85}Rb as $|\psi_0|^2 = (2.05)/a_0^3$, and a calculated value for the screening factor as $\beta_s = 1.1$ [19]. Therefore the total electronic factor is $F/h = 0.19128899$.

The $f(Z)$ function includes information about the charge distribution within the nucleus as well as relativistic correction factor. It has been evaluated for rubidium [4][page 43] as $f(37) = -3398 \text{ MHz/fm}^{-2}$, so that the total conversion factor can be written

$$\delta\langle r^2 \rangle = \frac{\delta\nu}{-650 \text{ MHz/fm}^2}. \quad (2.37)$$

Our measurement of the isotope shift $\delta\nu$ can then be converted to a $\delta\langle r^2 \rangle$.

Chapter 3

The Production of the Sub-Doppler Change Signal using LINO

This chapter presents the theory of the sub-Doppler change signals produced in the gamma-ray emission of the ^{85m}Rb isomer using laser induced nuclear orientation (LINO). It explains how optical pumping produces an excess population in a particular sub-level of the level being pumped and how this population excess produces an anisotropic radiation pattern in the gamma-ray emission of the nuclei. It explains how a Doppler-broadened signal results from using a gas in a cell system, and then how standing wave saturation can narrow that signal to homogeneous width. It explains the effects of velocity changing collisions in the production of anisotropy, and shows why the experiment is conducted in a low pressure region.

3.1 Anisotropy through Optical Pumping

Of paramount importance in this experiment is the redistribution of the populations of the hyperfine sublevels, producing an excess of population in some levels and a depletion in other sublevels. These non-equal populations produce anisotropy in the gamma-ray decay of the isomer. This section describes the hyperfine structure of the isomer, the ma-

trix elements coupling various electronic states, the process of population redistribution through optical pumping, and the effect of population redistribution on the gamma-ray spatial distribution.

3.1.1 The Coupling Between Electronic States: The Electronic Dipole Transition

As described in chapter 2, the hyperfine structure of $^{85\text{m}}\text{Rb}$ couples the nuclear spins states (I) and the electronic angular momentum states (J) into a total atomic angular momentum (F). Each F level will have $2F+1$ Zeeman sub-levels which are degenerate in energy in the absence of an external field.

The Absorption of Linearly Polarized Light

The atomic electrons can be excited from the ground F, M_F state to an upper $F', M_{F'}$ state by the absorption of an incident photon. The incident light is described by the location of the electric vector relative to the propagation axis (Poynting vector) of the light. It can be circularly polarized (right or left) or linearly polarized. The absorption of the light by the atomic electrons depends on the polarization, and is governed by quantum mechanical selection rules. For linearly polarized light, the $\Delta M_F = 0$ rule governs, for right circularly polarized light the rule is $\Delta M_F = 1$, and for left circularly polarized light $\Delta M_F = -1$. For reasons explained later on in this section, we have chosen linearly polarized light for the experiment.

The cross section for absorption between a photon and an atomic electron is given by the absorption cross section [16]

$$\sigma_H = 8\pi k \frac{|\mu|^2}{\hbar \gamma_N} \frac{\gamma_N}{\gamma_H} \mathcal{L} \quad (3.1)$$

where γ_N is the natural width of the transition, γ_H is the homogeneous width of the transition, k is the wavenumber, and \mathcal{L} is the lineshape function describing the transition. A discussion of these quantities is deferred until section 3.2. The quantity of interest

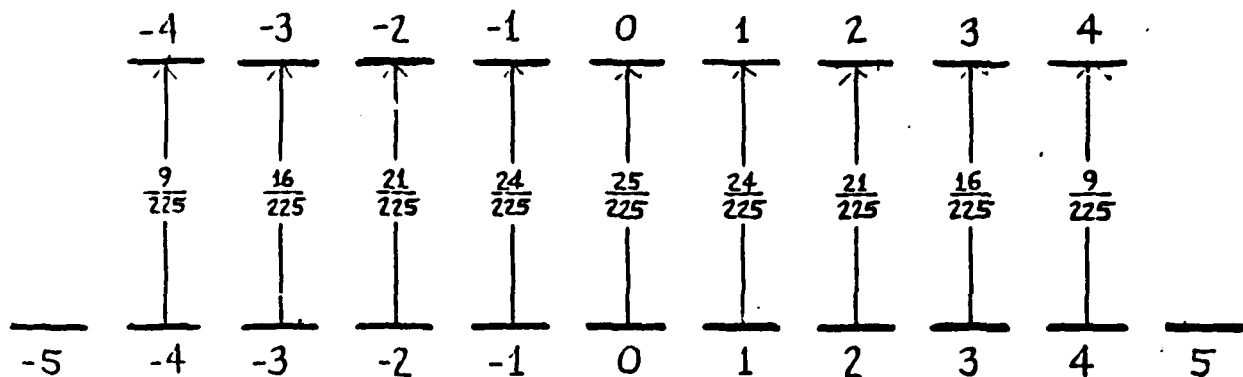


Figure 3-1: Sub-level structure of $F=5$ ground state and first excited state $F'=4$ of ^{85m}Rb . Each F level is divided into $2F+1$ sub-levels. Matrix elements for absorption of linearly polarized light are shown between sub-levels.

presently is $|\mu|^2$, the electronic dipole matrix element. The evaluation of the matrix elements between the different F levels and M_F sublevels of ^{85m}Rb is done in Appendix 1. These matrix element represent the relative strength of different couplings.

As an example, consider the matrix elements coupling the $F=5$ to $F'=4$ transition shown in Fig. 3.1. The total matrix elements added across the level equal $165/225$. Now consider the $F=4$ to $F'=4$ transition, shown in Fig. 3.2. Adding the matrix elements across this transition yields a $60/225$ sum. Therefore, taking the ratio of the two shows the first transition to be 2.75 times stronger than the second for absorption with linearly polarized light.

Radiative Decay and Branching Ratios

For radiative decay the selection rules are $\Delta M_F = 0, \pm 1$. The matrix elements for the decay for the states described above are shown in Fig. 3.3. The total decay rate from the excited state is given by $1/\tau$ where τ is the spontaneous lifetime of the excited state, which in this case is 27 nanoseconds. That rate can be apportioned to the various levels

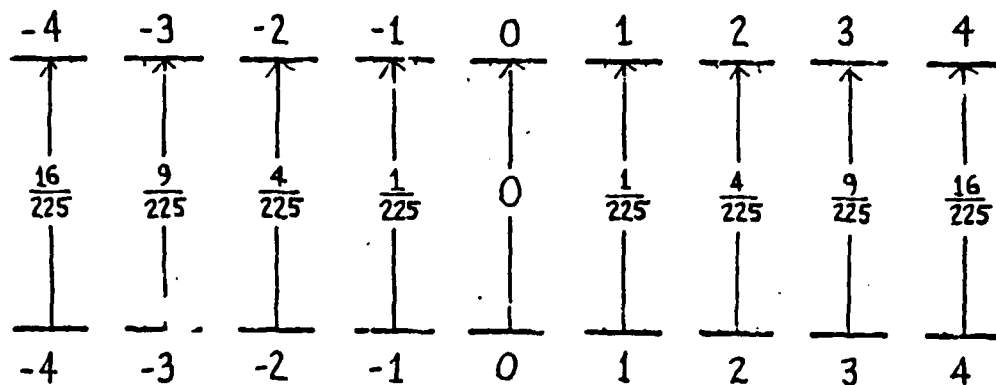


Figure 3-2: Matrix elements for absorption for linearly polarized light from $F=4$ to $F'=4$ transition.

and sub-levels in the same way that absorption is. For example, the decay to the $F=5$ ground state is the sum of all the matrix elements which is $495/225$. The sum for decay to the $F=4$ state is $180/225$. Therefore the branching ratio to the $F=5$ ground state is

$$\Gamma_{4'5} = \frac{495}{495 + 180} = \frac{99}{135} \quad (3.2)$$

and for the $F=4$ ground state

$$\Gamma_{4'4} = \frac{180}{675} = \frac{36}{135}. \quad (3.3)$$

The actual decay rate to the level is the branching ratio times the total decay rate, $1/\tau$. So, relatively speaking, this $F=5$ to $F'=4$ transition could be categorized as a strong absorber with a relatively low loss rate to the unpumped level.

3.1.2 Population Transfer within Sub-Level through Optical Pumping

Population can be transferred within sub-levels of a pumped level. The population trans-

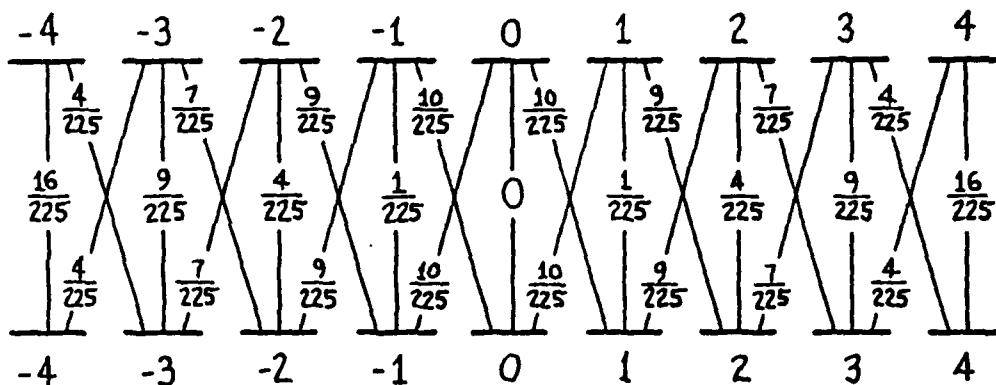
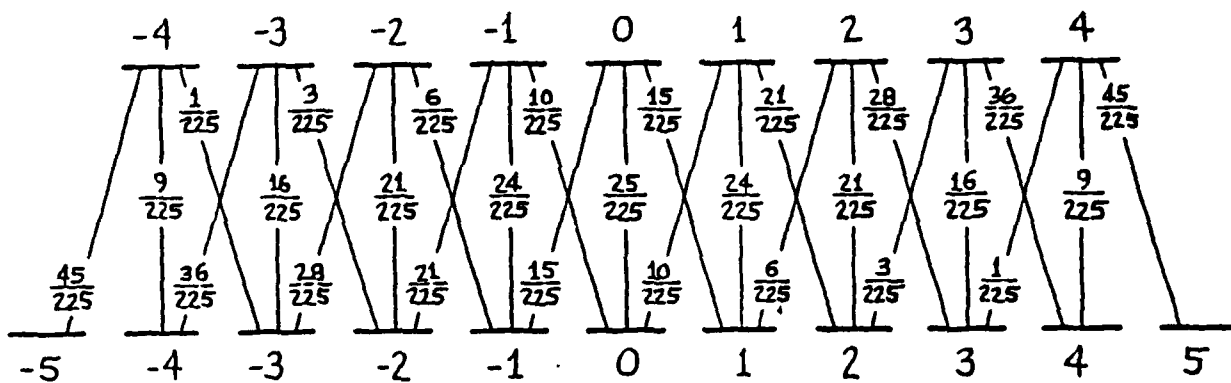


Figure 3-3: The matrix elements for decay from the $F' = 4$ level.

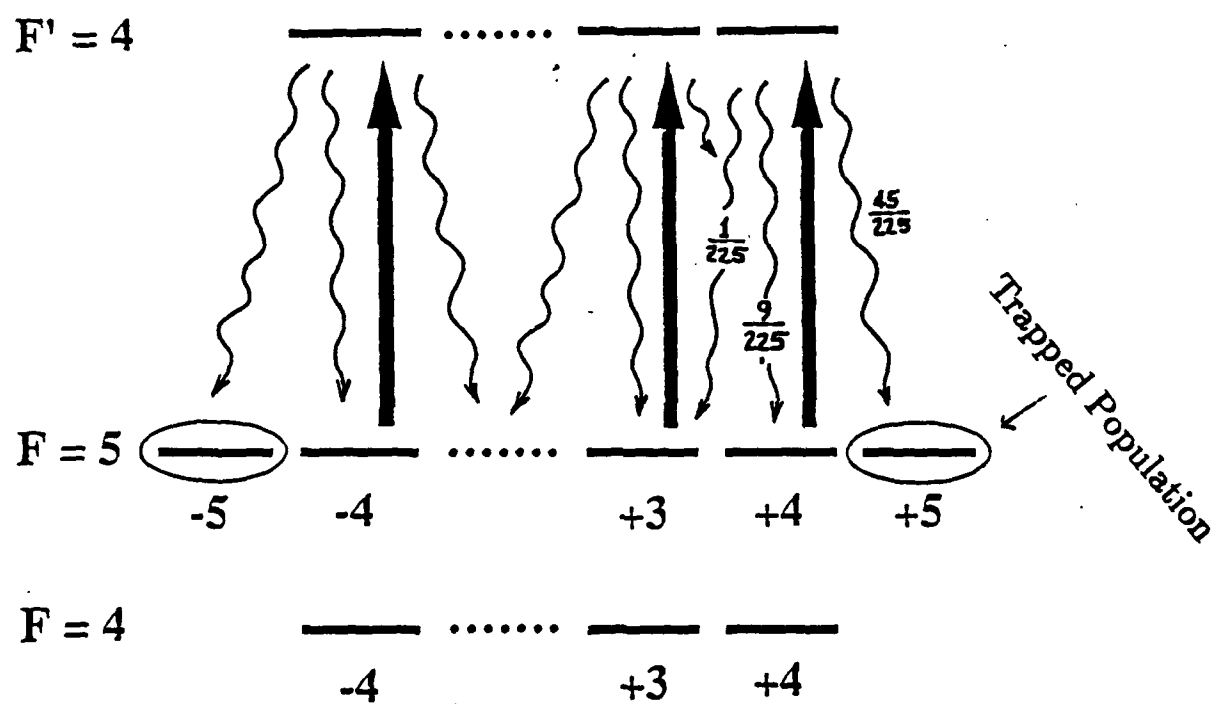


Figure 3-4: Matrix elements for decay of an atom excited to $F' = 4$, $M_F = 4$ sub-level.

fer effect can best be visualized as walking the population of the sub-levels over to an unpumped level. For example, consider an atom in the $F=5$, $M_F=4$ state excited into the $F'=4$, $M_{F'}=4$ sub-level, as shown in Fig. 3.4. It can decay three ways back to the $F=5$ state, and two ways back to the $F=4$ state, the sum of the matrix elements being 75/225. From the diagram, the probability that it will go to the $F=5$, $M_F=5$ state is 45/75 or 60 %. The probability that it will go to either the $F=5$, $M_F=4$ or $M_F=3$ state is 10/75 or 13%. The probability that it decays to the $F=4$ unpumped ground state is 20/75 or 27%. If it goes back into the $F=5$ pumped sub-levels, it can be again excited to the upper level where it will decay following the same probability pattern. In the same manner the other pumped sub-levels are pushing population over to the unpumped levels. This creates an excess population in the unpumped levels.

The more times these atoms are excited to the upper level, the more population is transferred to the unpumped ground levels. In an unstable atom, the number of cycles and hence the amount of population transferred, depends on the lifetime of the isomer and the spontaneous emission time of the excited state. If the incident laser intensity is high enough that the probability that the atom will absorb a photon approaches certainty, then the number of cycles can be approximated by dividing the lifetime of the atom by the spontaneous decay time of the excited state, i.e.,

$$\#cycles = \frac{T_{atom\ average\ isomer\ lifetime}}{\tau_{spontaneous\ decay}}. \quad (3.4)$$

In the case of ^{85m}Rb , the average lifetime of the isomer as an atom is 1 microsecond, and the spontaneous decay time is 27 nanoseconds, yielding 37 cycles. (The atom's average isomer lifetime is different from the average isomer lifetime of 1.4 microseconds since the isomer is produced as an ion and must be neutralized before it can be optically pumped [see section 4.1.2].)

Lost Population to the Unpumped Level

As described above, and illustrated in Fig. 3.4, when pumping with only one laser, a certain percent of the population is lost to the $F=4$ ground state. For those pumping schemes which have relatively strong matrix elements between levels, such as the $\Delta F = \pm 1$ transitions, it is still possible despite this loss to achieve a significant population excess in some sub-level of the pumped level, and therefore a significant anisotropy. However for the $\Delta F = 0$ transitions, which have relatively weak matrix elements with linearly polarized light, the loss term (branching ratio to unpumped state) becomes dominant, and very little population excess is created in a particular sub-level of the pumped level. This effect clearly shows up in our experimental results [chapter 5].

To enhance these weak transitions, a second laser can be used to redistribute this "lost" population by pumping it to an excited state, where some of it would decay back into the the ground state of interest for re-distribution. This was done by Dr. Shimkaveg in his work. In our work we did not use a second laser, as it was possible to map enough transitions in the D1 and D2 to extract the information we needed.

Relative Population Excess and Sublevel Grouping: The Three Level Model

The population of each of the 20 ground state sub-levels (11 from the $F=5$ level and 9 from the $F=4$ level) in the absence of optical pumping is the same, $N_{Tot}/20$, where N_{Tot} is the total population of the levels. The population excess for a particular sublevel can be written

$$\delta N_{M,F} = N_{M,F}^{Optical\ Pumping} - N_{M,F}^{No\ Optical\ Pumping}. \quad (3.5)$$

For simplification in modeling, Quivers has suggested [16] that it is possible to group common sublevels together based on their approximate behavior when being optically pumped. For example, when optically pumping the $F=5$ to $F'=4$ transition described earlier, the 20 sublevels of the $F=5$ and $F'=4$ levels can be reduced to three levels, numbered and constructed in the following manner: (1) the 9 $M_F = 4..0..-4$ sublevels

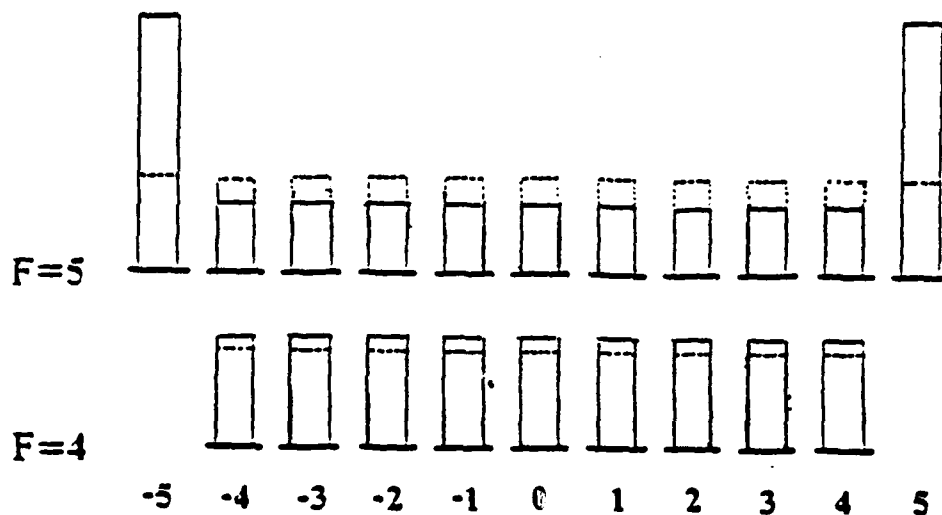


Figure 3-5: Population transfer to trapped $M_F = \pm 5$ levels. Excess population also produced in $F=4$ ground state, but does not contribute to anisotropy.

of the $S_{1/2}$ $F = 5$ level ; (2) the 2 $M_F = \pm 5$ sublevels of the $S_{1/2}$ $F = 5$ level ; (3) the 9 sublevels of the $F' = 4$ level. In this model, the source of the anisotropy is the excess population in the 2 level.

The population transfer effect for this model is illustrated in Fig. 3.5. The dashed lines show the population in each sub-level in the absence of laser pumping. The laser pumping re-distributes the population equally to the grouped sub-levels. The $M_F = \pm 5$ sub-levels (or level 2) are the trapping levels. Although there is also excess population in the $F=4$ level (Fig. 3.5), in our model it is the excess population built up in a sub-level relative to the other sub-levels of the level that produce the anisotropy. In the $F=4$ ground state, the excess is assumed equally distributed within all the sub-levels, producing no anisotropy. While this is not strictly true, it is a fair approximation as shown by Dr. Shimkaveg [6][page 166].

The relative population excess produced by this particular pumping scheme can be written

$$\mathcal{P} \approx \frac{\delta N_{5,5}}{N_{Tot}} \quad (3.6)$$

which is directly related to the observed anisotropy (see below).

3.1.3 The Excess Population in the Sub-Levels Causes an Anisotropic Pattern in the Gamma-ray Emission of the Isomer

The excess population built up in the $M_F = \pm 5$ sub-levels will produce an anisotropy in the gamma-ray emission of the isomer. This $M_F = \pm 5$ sub-level corresponds to a nuclear spin state of $I = \pm 9/2$, so there is a population excess in this nuclear sub-level. Since this state is defined with reference to a quantization axis (also called a keeper field [17]), there will be more gamma rays emitted on average in this direction, and less on average from other directions. In the following section, we see how this excess population produces the anisotropic gamma-ray pattern.

Multipole Radiation Patterns

The excited state at 514 keV has a spin parity of $9/2^+$ while the ground state has $5/2^-$, so that the decay involves a $\Delta I = 2$ with a parity change, characteristic of the M2 radiation which is observed in this decay. The angular intensity pattern emitted from a radiating quadrupole of charges or currents is [25]

$$I(\theta) = \frac{c}{8\pi k^2} \sum_q |a_{2q}|^2 |X_{2q}(\theta, \phi)|^2 \quad (3.7)$$

where c is the speed of light, k is the wavevector ($2\pi/\lambda$), the coefficients a_{2q} depend on the source, and

$$|X_{2q}(\theta, \phi)|^2 = \frac{(2+q)(3-q)}{12} |Y_{2q-1}(\theta, \phi)|^2 + \frac{q^2}{6} |Y_{2q}(\theta, \phi)|^2 + \frac{(2-q)(3+q)}{12} |Y_{2q+1}(\theta, \phi)|^2 \quad (3.8)$$

where $q = (-2, -1, 0, +1, +2)$ is the orientation transfer (ΔM_I) radiated from the quadrupole source, the $Y_{l,m}$'s are the familiar spherical harmonics and the X functions are identical for $\pm q$ due to parity symmetry. The X 's are also axially symmetric, independent

of ϕ , since the ϕ variable appears only in the phase of the spherical harmonics, and is lost when evaluating the magnitude. The radiation patterns produced are shown in Fig 3.6. In the absence of optical pumping the $a_{2,q}$ coefficients add to 1, producing an isotropic decay pattern. This corresponds physically to the case where the sub-levels are all equally populated, as is the case in the absence of laser optical pumping. Excess population in the $M_I = \pm 9/2$ sublevel produces an anisotropic component superimposed on the isotropic background. Since the $M_I = \pm 9/2$ state corresponds to the $X_{2\pm 2}$ function, then the radiation pattern (Φ_{FM}) corresponding to this state is equal to

$$\Phi_{5,\pm 5} = |X_{2,\pm 2}| = \frac{5}{16\pi}(1 - \cos^4\theta). \quad (3.9)$$

The total radiation pattern of the sample can be written

$$\Phi(\theta) = C_0 + \mathcal{P}\left(\frac{5}{16\pi}\right)(1 - \cos^4\theta) \quad (3.10)$$

where C_0 represents the isotropic background, and the anisotropic component is proportional to the relative population excess (equ. 3.6) in the $M_{9/2}$ sublevel. The total radiation as the sum of the two pattern is illustrated in Fig. 2.7.

The pattern is normalized

$$2\pi \int_{\theta=0}^{\pi} \Phi(\theta) \sin\theta d\theta = 1 \quad (3.11)$$

so that the normalization constant is

$$C_0 = \frac{1 - \mathcal{P}}{4\pi}. \quad (3.12)$$

The expression then becomes

$$\Phi(\theta) = \frac{1}{4\pi} \left[1 + \mathcal{P} \frac{(1 - 5\cos^4\theta)}{4} \right]. \quad (3.13)$$

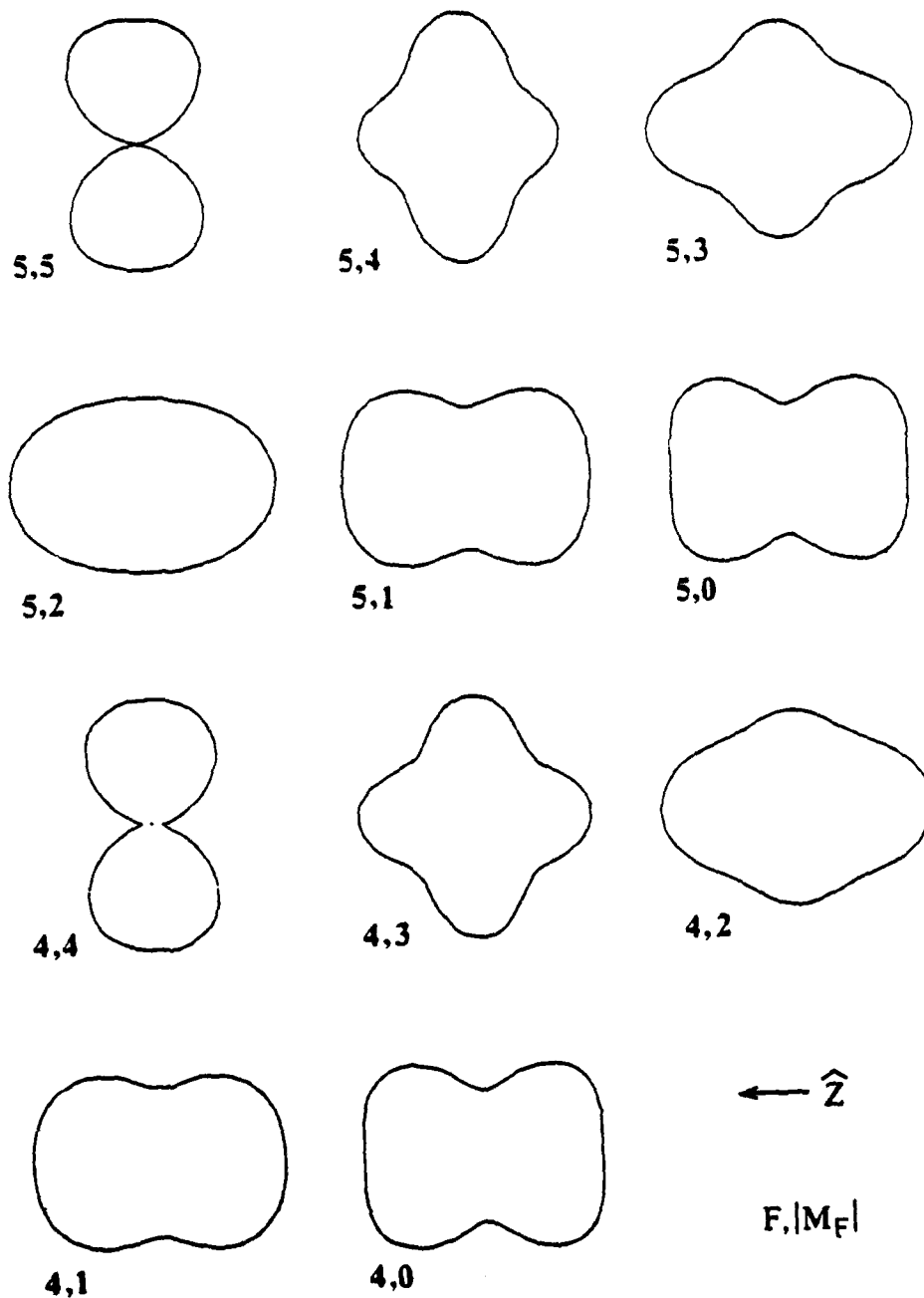


Figure 3-6: Radiation patterns produced by F, M_F sub-levels in gamma-ray decay of ^{85m}Rb . (Courtesy of Shimkaveg)

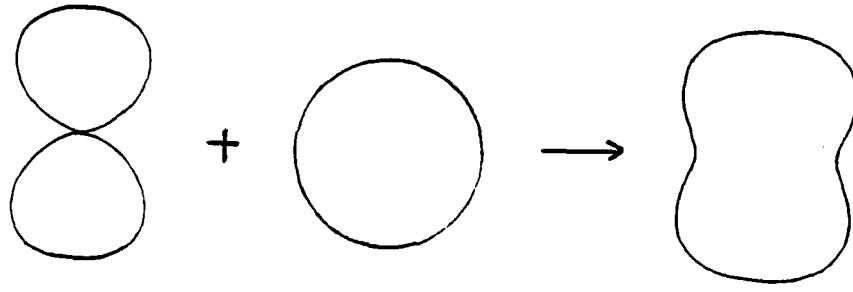


Figure 3-7: Total radiation pattern seen by detectors is the sum of the isotropic background due to equal populations in all sub-levels, and the anisotropic pattern due to excess in $M_F = \pm 5$ sub-levels.

We note that in the limit as the population excess goes to zero, the pattern becomes isotropic, i.e.

$$\Phi(\theta) = \frac{1}{4\pi} \quad (3.14)$$

and in the limit where all the population is in the $\pm 9/2$ sub-level, or $\mathcal{P} = 1$, then

$$\Phi(\theta) = \frac{5}{16\pi}(1 - \cos^4\theta) = |X_{2\pm 2}|^2 \quad (3.15)$$

or completely anisotropic.

Calculation of Anisotropy

The function used to measure anisotropy is

$$A = \frac{N_{on} - N_{off}}{N_{on} + N_{off}} \quad (3.16)$$

where N_{on} refers to the number of counts with the laser on and N_{off} refers to the number of counts with the laser off. Since we used two detectors in this work, detector 1 at 0° and detector 2 at 180° to our quantization axis, our anisotropy is

$$A = A_1 + A_2 \quad (3.17)$$

where the subscript 1 or 2 refer to the detector 1 and 2 .

For the limiting case of a point source and point detector the number of counts seen by the detector is proportional to the radiation pattern i.e., $N_1 \propto \Phi(0)$ and $N_2 \propto \Phi(180)$. Then the number of counts seen by detector 1 with the laser is on can be written

$$N_1 = N_{1\,off}(1 - \mathcal{P}) \quad (3.18)$$

where \mathcal{P} is the relative population excess defined previously. The anisotropy for detector 1 is then

$$A_1 = \frac{N_{1\,off}(1 - \mathcal{P} - 1)}{N_{1\,off}(1 - \mathcal{P} + 1)} \approx -\frac{\mathcal{P}}{2} \quad (3.19)$$

where $1 - \mathcal{P} + 1 \approx 2$ for small \mathcal{P} . If the detectors are properly balanced so that $N_{1\,off} = N_{2\,off}$ the total anisotropy can be written

$$A \approx -\mathcal{P} \quad (3.20)$$

so that the anisotropy produced is approximately equal to the relative population excess in the $M_{\pm 5}$ sublevels.

3.2 Creating a Sub-Doppler Change Signal in the Anisotropy through Saturation Spectroscopy

We have seen above how the excess population in a particular sublevel can result in an anisotropic gamma-ray emission signal from the radioactive nuclei. In this section we

will explain the shape and width of the anisotropy signal produced. We will look at why a Doppler-broadened signal is produced when using a gas in a cell system, and then we will see how we use saturation spectroscopy to narrow the signal to homogenous width. We first start out, however, by providing a little background information on lineshapes necessary for discussing our results.

3.2.1 One Laser Beam Creates a Doppler-Broadened Signal

The spectral lines in absorption and emission spectra are never exactly monochromatic. Instead, the intensity of the line can be described by a distribution function, $I(\omega)$, around a central frequency

$$\omega_0 = (E_i - E_k)/\hbar \quad (3.21)$$

where

$$\Delta E = E_i - E_k \quad (3.22)$$

corresponds to the energy difference between upper and lower levels. The frequency interval

$$\delta\omega = |\omega_2 - \omega_1| \quad (3.23)$$

between the two frequencies ω_1 and ω_2 for which $I(\omega_1) = I(\omega_2) = I(\omega_0)/2$ is called the full width at half maximum (FWHM).

The Natural Linewidth

For an atom in an excited state the radiative decay of the emitted light can be written

$$I_{sp} = I_0 \frac{1}{(\omega - \omega_0)^2 + (\gamma/2)^2} \quad (3.24)$$

where $\omega_0 = \nu_0/2\pi$ is the natural frequency of the transition, $\gamma = 1/2\pi\tau_{sp}$ is the natural or radiative linewidth (in Hertz) and τ_{sp} is the spontaneous lifetime (in seconds) of the

transition. To compare distributions, the normalized distribution is introduced

$$\int_{-\infty}^{\infty} g(\omega - \omega_0) d(\omega - \omega_0) = 1. \quad (3.25)$$

Then the normalized Lorentzian profile becomes

$$g(\omega - \omega_0) = \frac{1}{2\pi} \frac{\gamma}{(\omega - \omega_0)^2 + (\gamma/2)^2}. \quad (3.26)$$

Now, in the general case, there are also non-radiative relaxation mechanisms that contribute to the broadening, in particular the collision broadening contributions. These include pressure broadening caused by neutral nonresident collisions between rubidium and krypton atoms. These are different than the velocity changing collisions discussed later, in that it is not the velocity changing effect that is important but rather the time-varying change in phase associated with the differential shift in electronic eigenstate energies that an absorbing atom is subject to during a collision. Such collisions also produce a pressure shift in the center frequency of the homogeneous lineshape. The contribution $\gamma_{Pressure}$ due to pressure broadening is proportional to the density of Kr atoms. At room temperature, this amounts to 19.8 MHz/Torr (FWHM) in the D1 line and 17.6 MHz/Torr (FWHM) [28]. The rubidium lines are also broadened by resonant broadening self-collisions, which amount to about 16 MHz (FWHM) at 300 mTorr. The total decay constant then is written

$$\gamma_{Homogeneous} = \gamma_{Natural} + \gamma_{Pressure} + \gamma_{Self}. \quad (3.27)$$

In our experiment, the γ_N is 6 MHz, and the γ_P is equal to 6.0 MHz at 300 mTorr for the D1 and 5.5 MHz for the D2, and the self broadening $\gamma_S = 16$ MHz so the total linewidth is 28 MHz.

For a full development see Feld [13]. For an abbreviated discussion see Demtröder [15][page 80-83].

The Doppler Profile

The atomic oscillators of a gas are continually undergoing random thermal motion. Then an assembly of atoms at a temperature T will have a distribution of velocities along a particular direction given by the Maxwell-Boltzman distribution

$$G(kv) = \frac{1}{ku} \exp-(kv/ku)^2 \quad (3.28)$$

where u is the thermal velocity given by eqn. (3.5) and

$$k = \omega/c \quad (3.29)$$

is the wavenumber, usually written in inverse centimeters. This type of distribution has a Gaussian profile and the width of this distribution is often given as ku , which is the $1/e$ half width. A Gaussian profile can also be normalized such that

$$\int_{-\infty}^{\infty} G(kv) d(kv) = 1. \quad (3.30)$$

To an observer at rest, the resonant frequency of the atom with velocity component v along the direction of emission or absorption of radiation will appear Doppler-shifted to frequency

$$\omega(v) = \omega(1 + v/c) = \omega + kv. \quad (3.31)$$

Atoms with different velocity components will appear to have different resonant frequencies. The Doppler-broadened distribution can then be divided into different velocity groups (or "bins"), each of homogeneous width (γ_H) with a Lorentzian profile. The number of groups is written

$$N_G \approx 2ku/\gamma_H \quad (3.32)$$

with γ_H given in FWHM. This is illustrated in Fig. 3.8.

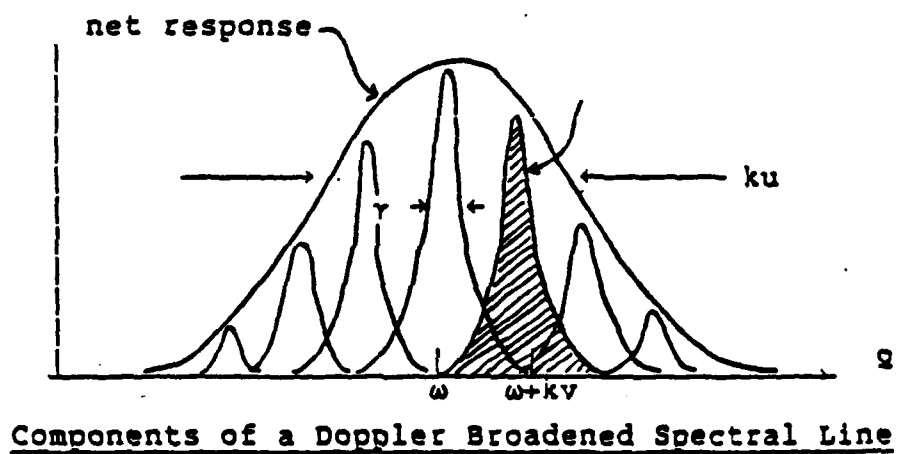


Figure 3-8: A Doppler-broadened distribution is divided into different homogeneous velocity bins.

Optically Pumping the Homogeneous Group

The interaction of the monochromatic laser radiation with the thermalized gas involves mainly those atoms in the velocity group which are Doppler-shifted into resonance with the laser frequency. In a multi-level system like the one we are dealing with, if the laser radiation is intense enough it can transfer a sizable fraction of the atoms in this group from a particular ground state energy level into another ground state level by exciting the atoms into an upper level, where a fraction of them decay into the other unpumped ground state level. This population transfer is described in 3.1.2. The "optical pumping" process can actually burn a "hole" in the Doppler distribution at the resonant velocity group. The more intense the beam, the deeper this hole is. At a certain intensity, however, the population transfer "saturates" and the population transfer is no longer directly proportional to the incident radiation. This population transfer effect, digging a hole at a particular velocity group in the pumped level and producing an excess in the population of the trapped level at the same velocity group is shown in Fig. 3.9 for a three level system. Note that the excited state acts only as a transfer mechanism here.

The rate at which atoms in a particular velocity group are optically pumped into the excited state is given by

$$R = \frac{\sigma_H I}{\hbar \omega} \mathcal{L} \quad (3.33)$$

where σ_H is the cross section for absorption given earlier and depends on the matrix elements coupling the ground state to the excited state, and where I is the intensity of the incident radiation. The Lorentzian profile factor \mathcal{L} is similar to that described earlier but now includes the Doppler-shifting, i.e.

$$\mathcal{L} = \frac{\gamma_H^2}{(\omega - \omega_0 - kv)^2 + \gamma_H^2} \quad (3.34)$$

where ω is the frequency of the laser and ω_0 is the frequency of the transition. The

OPTICAL PUMPING 3 LEVEL DOPPLER SYSTEM

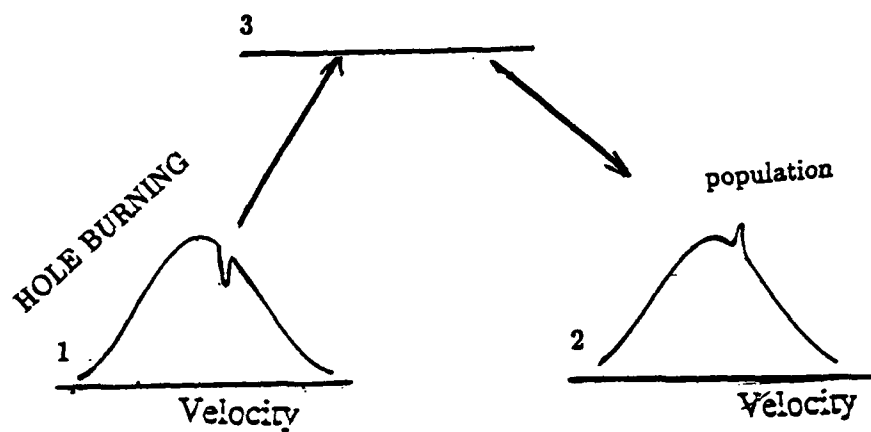


Figure 3-9: Optical pumping 3-level system digs a hole in the pumped level, and puts the excess population in the trapped level.

intensity at which the transition saturates is given by [16]

$$I_s = \left(\frac{\gamma_e}{\gamma_e + \gamma_g - \Gamma_{BR}} \right) \frac{\hbar\omega}{\sigma_H} \gamma_g \quad (3.35)$$

where γ_e is the excited state relaxation rate, γ_g is the ground state relaxation rate, and Γ_{BR} is the decay rate from the excited state back to the optically pumped ground state. The excited state relaxation rate in the absence of collisions can be written

$$\gamma_e = \frac{1}{\tau_{sp}} + \frac{1}{T_{avg}} \quad (3.36)$$

and the ground state relaxation rate is written

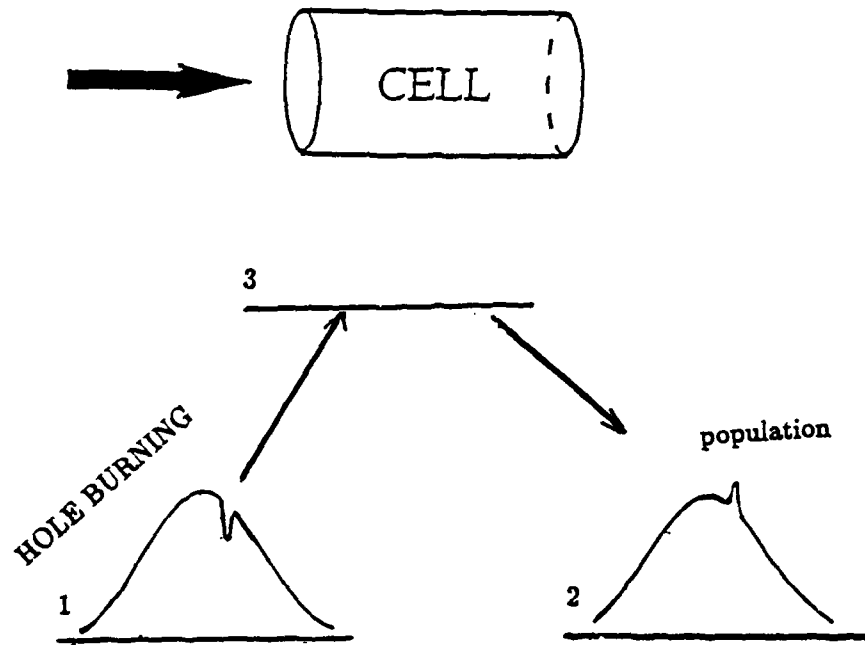
$$\gamma_g = \frac{1}{T_{avg}} \quad (3.37)$$

where T_{avg} is the average lifetime of the isomer as an atom. Note as the branching ratio, Γ_{BR} , increases the saturation intensity increases also, making it more difficult to transfer population. These expression will be modified when collisions effects are considered (section 3.3).

In our detection scheme we count the gamma rays from all velocity bins at the same time. Therefore, our anisotropy is proportional to the number of excess atoms in the unpumped sub-level. When the laser frequency is in resonance with a particular velocity group of atoms, the number of atoms transferred to the unpumped level is proportional to the number in that group, which is governed by the Doppler distribution function. As the laser is tuned into resonance with different velocity groups, the anisotropy function will map out the Doppler profile.

This one beam pumping is illustrated in Fig 3.10. The population transferred to the trapped level is shown (cross-hatched) with the resultant Doppler profile mapped out.

ONE BEAM LASER PUMPING



DOPPLER BROADENED SIGNAL

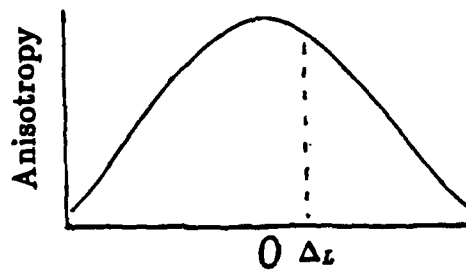


Figure 3-10: One beam optical pumping transfers population to trapped level. The resultant anisotropy, proportional to total excess number of atoms from all velocity groups, maps out Doppler profile.

3.2.2 The Counter-Propagating Beam Produces a Saturation Effect

Now consider a sample of atoms in a cell optically pumped by a laser beam split into two beams, with one beam entering the front of the cell and the other beam entering the rear of the cell. When the laser frequency is detuned off the atomic resonance, ω_0 it will interact with two velocity groups of atoms, the group moving towards the beam entering the front of the cell with $v = \Delta/k$ and the group moving towards the rear of the cell with the minus velocity. The number of atoms transferred to the trapped level will reflect the contribution from two different velocity groups. However, when the laser frequency is tuned into resonance with the atomic transition only one group of atoms will be in resonance, the group with zero velocity. If the transition is saturated, that is if the laser intensity is high enough so that the number of atoms in a velocity bin transferred to the trapped level is not directly proportional to the intensity of the incident light (non-linear response), then the number of atoms in the trapped level will decrease, causing a dip in the anisotropy signal measured by the detectors. This is illustrated in Fig. 3.11.

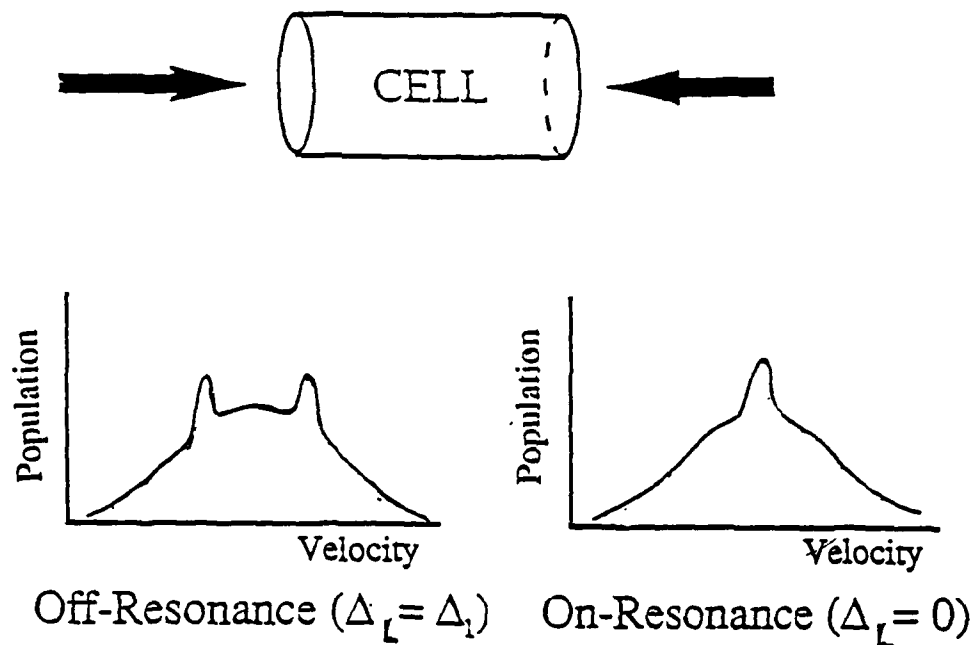
This decrease is called a "Lamb Dip" after Willis E. Lamb, Jr. who postulated its existence in 1962, and is used to obtain a narrow resonance in the absorption spectrum of atoms. Here, it is creating a narrow resonance in the gamma emission of an unstable nucleus.

3.2.3 The Difference Between the Two Anisotropies is the Change Signal

We can measure the effect of the overlapping beams in the following manner. Let the beam entering the front of the cell be #1 and the counterpropagating beam be #2. If both beams illuminate the cell, the spatially overlapped beams will produce a count rate

$$N_{Both} = N_{off} + \Delta N_{Beam 1} + \Delta N_{Beam 2} + \epsilon \quad (3.38)$$

TWO BEAM LASER PUMPING



LAMB DIP IN DOPPLER PROFILE

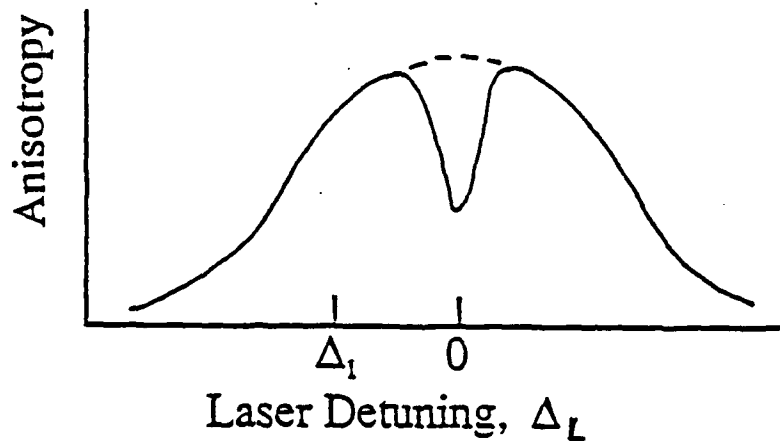


Figure 3-11: Two-beam optical pumping. When laser is tuned to zero velocity group, less atoms are transferred to trapped level. The resulting dip is shown in the anisotropy profile.

where N_{off} is the count rate in the absence of optical pumping, $\Delta N_{beam 1}$ is the change in count rate due to beam 1 in the absence of beam 2, $\Delta N_{beam 2}$ is the count rate due to beam 2 in the absence of beam 1, and ϵ is the decrease in both due to overlap of excited velocity groups.

Now if we turn off beam 2, and count only with beam 1 on, we get

$$N_{Beam 1} = N_{off} + \Delta N_{Beam 1}. \quad (3.39)$$

Likewise, if we count with only beam 2 on then we get

$$N_{Beam 2} = N_{off} + \Delta N_{Beam 2} \quad (3.40)$$

and, counting with no beam on we get N_{off} .

We can therefore define the difference function, or change signal, as

$$D \equiv \frac{N_{Both} - N_{Beam 1} - N_{Beam 2} + N_{off}}{2N_{off}} = \frac{\epsilon}{2N_{off}} \quad (3.41)$$

which is the quantity that we measure experimentally. The difference signal is shown in Fig. 3.12.

3.3 Velocity Changing Collisions Affect the Optical Pumping

The isomer is undergoing velocity changing collisions in the cell as a function of krypton pressure. A velocity changing collision (vcc) is an elastic collision which does not destroy the orientation (Zeeman sub-level) of the atom. As the name suggests, these collisions move atoms from one velocity group to another. The vcc rate can be written

$$\Gamma_{vcc} = n_{Kr} \sigma_{vcc} v_{rel} \quad (3.42)$$

CHANGE SIGNAL

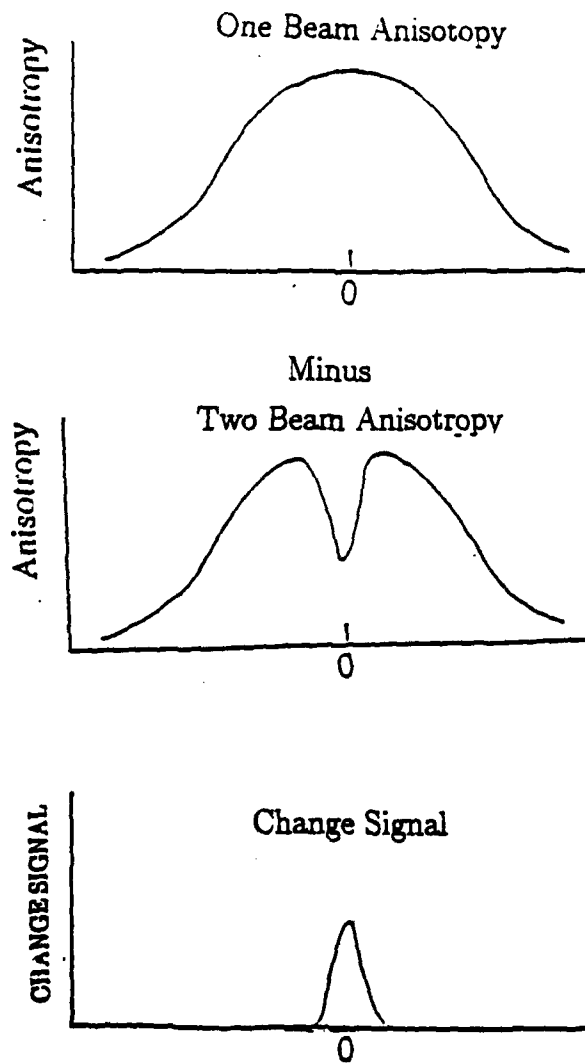


Figure 3-12: The change signal is produced by the difference between two laser pumping and one laser pumping.

where n_{Kr} is the number density of krypton atoms in the cell, σ_{vcc} is the cross section for collisions (estimated at 50 \AA^2 using "billiard ball" type collisions [6][page 68]), and v_{rel} is the relative velocity between the isomer and the krypton atoms. The number of vcc's in the isomers lifetime is usually written as $\Gamma_{vcc}T_{avg}$.

Vcc's can be either desirable or undesirable, depending upon what type of signal one is trying to produce. If one is trying to produce a Doppler-broadened signal, then the vcc's allow one to optically pump most of the atoms in the Doppler profile, producing a relatively large anisotropy, but a broad signal (which may be adequate depending upon the resolution needed). This was done in Dr. Shimkaveg's experiment. If one is trying to produce a narrow Lorentzian signal, then the vcc's have an undesirable effect and must be minimized.

3.3.1 Pumping With Many Vcc's Increases the Number of Atoms Pumped But Gives a Broad Signal

The vcc rate does affect how the laser saturates the homogeneous group, since atoms will spend less time on average interfacing with the laser. The effect is included in the relaxation rates given earlier, so that the excited state relaxation rate becomes

$$\gamma_e = \frac{1}{\tau_{sp}} + \frac{1}{T_{avg}} + \Gamma_{vcc} \quad (3.43)$$

and the ground state relaxation rate becomes

$$\gamma_g = \frac{1}{T_{avg}} + \Gamma_{vcc}. \quad (3.44)$$

As the vcc rate increases, it becomes harder and harder to saturate the particular velocity group in resonance with the laser.

Since the laser radiation pumps only the particular velocity group which has been shifted into resonance, and therefore only a fraction of the atoms in the Doppler distri-

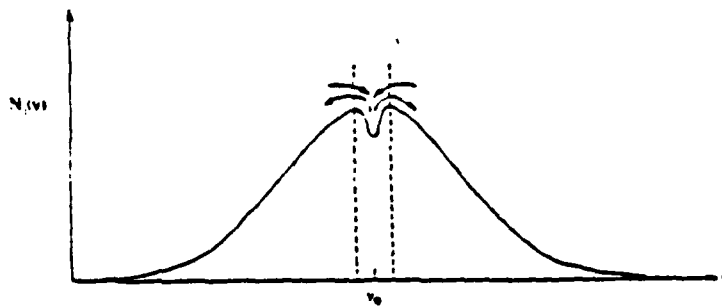


Figure 3-13: Effect of vcc's on laser optical pumping, with pump laser tuned to resonance. Buffer gas perturbors cause vcc's into and out of the resonant velocity bin (broken vertical lines). (From Quivers.)

bution. This fraction is normally approximated as $1/N_G$ where N_G is defined earlier. One way to increase the number of atoms in resonance with the laser is to introduce vcc's into the system. During optical pumping the vcc's transfer pumped atoms into nonresonant velocity groups and replenish the resonant velocity group with atoms not yet pumped. This is illustrated in Fig. 3.13.

This allows the laser to effectively interact with more of the atoms in the distribution than it would normally.

To completely remove velocity selectivity from the pumping process, two conditions must be met [16]. The number of collisions ($\Gamma_{vcc} T_{avg}$) in the atom's lifetime must be relatively high, i.e.

$$\Gamma_{vcc} T_{avg} \gg \frac{2ku}{\gamma_H} = N_G \quad (3.45)$$

with Γ_{vcc} determined using eqn. (3.6) and $T_{avg} = 1.0 \mu s$ from Hutton's calculations (section 3.1.2). Also the collision rate must be much greater than the pump rate

$$\Gamma_{vcc} \gg R \quad (3.46)$$

where R is defined earlier.

When these two conditions are met, the parameter that specifies the effectiveness of pumping the Doppler distribution is called the optical-pumping saturation intensity and is written [16]

$$I_{OP} = \frac{1}{\rho} \frac{\hbar \omega}{\sigma_D} \frac{1}{T_{avg}} \quad (3.47)$$

where ρ is the branching ratio to the trapping state and σ_D is the Doppler-broadened absorption cross section, which can be written

$$\sigma_D = \sigma_H \frac{\gamma_H \sqrt{\pi}}{2ku} \exp -(kv/ku)^2. \quad (3.48)$$

Note that it is reduced from the homogeneous cross section.

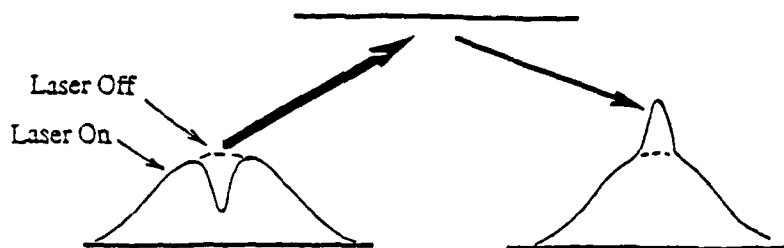
There are two saturation parameters now when pumping with vcc's. The dominant one depends on the number of vcc's. In the low pressure region with few vcc's $I_s \gg I_{op}$, and it is easier to pump the homogeneous group than the whole profile. At high pressure with many vcc's $I_{op} \gg I_s$, and it is easier to pump the whole profile than the particular velocity bin.

The initial experiment done by Dr. Shimkaveg was in the high vcc limit, where all velocity selectivity was removed. At a temperature of 160°C with 4 Torr of krypton pressure the isomer's average velocity is thermal and $ku = 360$ MHz, so that $\Gamma_{vcc} T_{avg} = 29$. Since γ_H equals 100 MHz (FWHM), then $N_G = 7$ and the experiment was conducted primarily in the Doppler regime [6][page 152].

3.3.2 Pumping with Just a Few Vcc's Produces a Dip and Pedestal

Ideally in our experiment, where we are trying to produce a homogeneous signal at the zero velocity bin, we would have no vcc's, as they tend to destroy velocity selectivity. However, this is not possible since the buffer gas that causes the vcc's is the source of our isomers. Therefore, we operate at a low pressure where there are some vcc's, but

Optical Pumping - No VCC's



Optical Pumping With VCC's

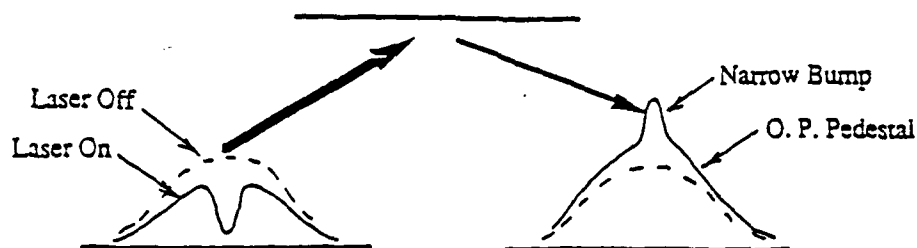


Figure 3-14: The effect of vcc on population transfer to the trapped level. The case with no vcc's just produces a homogeneous bump. The case with vcc's produces a bump and a pedestal.

not enough to remove all the velocity selectivity. For example, at 300 mTorr of Kr pressure the number of collisions in an isomers lifetime as an atom is 2. We are then in an intermediate area, where we expect both velocity selective features and velocity independent features.

Being in this intermediate region produces two components in the population transferred to the trapped level (and in the resultant anisotropic change signal described earlier), (1) a narrow "dip" of homogeneous width produced by atoms that are resonant with the field but do not undergo vcc's, and (2) a broad Doppler "pedestal" with all velocity selectivity removed. This is illustrated in figure 3.14.

The relative size of the two features depend on the dominance of the vcc process. The larger the pedestal, the more effective the vcc's. For a fixed laser intensity, the size of the pedestal increases with pressure, while that of the dip decreases.

Chapter 4

The Experimental ^{85m}Rb Gas-Cell System

4.1 Isomer Production and Neutralization in a Cell System

This section explains the production of the isomer and its neutralization for optical pumping. In particular, since this experiment is conducted in low pressure regions, for reasons explained in chapter 3, the focus is on the neutralization process at low pressure. Included in the discussion on neutralization is the effect of the non-thermal velocity distribution of the recoiling isomer when the parent β decays, an important consideration at low pressure.

4.1.1 Production of the Isomer

Krypton gas, enriched to 30% ^{85}Kr , is placed in a sealed pyrex cell along with a small drop of natural rubidium. The radioactive krypton, which has a half life of 10.7 years, decays by β^- emission 99.6% of the time to the ground state of ^{85}Rb and 0.4% of the time to an excited state of ^{85}Rb , the isomer ^{85m}Rb , which subsequently undergoes gamma

decay (M2) with a half life of 1.0 microseconds. The decay scheme is shown earlier in Chapter 1.

4.1.2 Neutralization of the Isomer

The isomers are produced predominantly in a singly ionized state. (A small number are produced in a doubly ionized state due to Auger processes (see [6][pages 72-76]), but this is a small effect which we can neglect). The optical transitions of the $^{85m}\text{Rb}^+$ lie far in the ultraviolet where tunable dye lasers are not available. Therefore, in order to optically pump these ions, they must first be neutralized. This is the function of the natural rubidium in the cell, which will undergo resonant charge exchange with the isomers and neutralize them. Rubidium, because its charge exchange cross section is very large, minimizes the amount of material needed in the cell, preventing an excess number of disorienting collisions from occurring. The rate at which the ions neutralize is called the charge exchange rate and is written

$$\Gamma_{\text{charge exchange}} = n_{\text{Rb}} \sigma_c v_{\text{rel}} \quad (4.1)$$

where n_{Rb} is the density natural rubidium, σ_c is the resonant charge exchange cross section, which is estimated at approximately $550 \pm 50 \text{ \AA}^2$ [6][page 71], and v_{rel} is the relative velocity between the ^{85m}Rb isomer and a neutral atom of natural rubidium. The density of the natural rubidium in the cell is tabulated as a function of temperature in Dr. Shimkaveg's thesis [6][page 71]. It is approximately exponential, and therefore is the predominant factor in the charge exchange rate at pressures above 100 mTorr. Below 100 mTorr, the v_{rel} term also obeys an exponential type behavior, as will be discussed below.

Thermalization of the Isomer - The v_{rel} Term

As seen above, the charge exchange rate depends on the relative velocity between the charged isomer and the neutral krypton in the cell. Additionally, the collisions rate, which also is extremely important in our work, depends on the relative velocity between the neutral isomer and the krypton gas. These relative velocities are quite different in low pressure regions (approximately below 500 mTorr) than they are in higher pressure regions. This can be understood by looking at what happens when the parent decays by β^- , and seeing how this effects the relative velocity term. The following is a brief summary from the work by Dr. Hutton and Prof. Quivers [12].

The nuclear decay to the isomeric state can be written



Some of the energy goes into the kinetic energy of the β^- particle, some into the $\bar{\nu}$, and some into the recoil of the nucleus. The angular correlation between the electron and neutrino emitted during β^- decay can be written

$$W(\theta) \approx 1 + a \frac{v}{c} \cos \theta \quad (4.3)$$

where v is the electron velocity, c is the speed of light, and θ the angle between the momenta of the electron and the anti-neutrino in the rest frame of the parent. The value of a is equal either to $+1$ or $-1/3$, depending on whether the transition is Fermi transition or Gamow-Teller.

In the Fermi interaction, the electron and anti-neutrino are emitted in the singlet state (spins anti-parallel) thus carrying away no angular momentum. Due to their helicities, they tend to be emitted in the same direction and so their linear momenta tend to add. This means that the recoil energy transmitted to the daughter will be relatively large. The selection rule for this process is $\Delta I = 0$, with no change in parity. In the Gamow-Teller interaction, the electron and anti-neutrino are emitted in the triplet state

(with spins parallel), and tend to be emitted in opposite directions, so that their linear momenta tend to cancel. Consequently, the energy transmitted to the daughter is less. The selection rules for this process are $\Delta = 0, 1$ (no $0 \rightarrow 0$) with no change in parity.

In the ^{85m}Rb system, both transition selection rules can be satisfied since the transition is from $I = 9/2^+$ to $I' = 9/2^+$. Therefore, for this case all that can be said is $-1/3 \leq a \leq +1$. In either case, the initial velocity distribution of the recoil ion is approximately Gaussian with a peak velocity of 1.17×10^5 for $a = -1/3$, or 1.41×10^5 for $a = +1$. The thermal velocity of a particle in a gas can be written

$$u = \sqrt{\frac{2k_B T}{M_{Rb}}} \quad (4.4)$$

where k_B is the Boltzman constant, T is the temperature in degrees Kelvin, and M_{Rb} is the mass of the atom. Using a temperature of 160°C (the temperature at which the initial Doppler experiments were done) yields a value of $u = 2.8 \times 10^4 \text{ cm/s}$. Therefore, the recoil speed is between 4.2 and 5.0 times thermal.

Now the "hot" ion will undergo velocity changing collisions (vcc's) at the following rate

$$\Gamma_{vcc}^+ = n_{Kr} \sigma_{vcc}^+ v_{rel} \quad (4.5)$$

where σ_{vcc}^+ is the cross section for collisions between the ion and a buffer atom and has been estimated to be approximately 350 \AA^2 based on Rb ion mobility data [12]. After the ion is neutralized the collisions can be treated as "billard ball" type collisions with the vcc rate the same as given earlier (equ. 3.42) and written

$$\Gamma_{vcc} = n_{Kr} \sigma_{vcc} v_{rel}.$$

After their recoil, the ^{85m}Rb ions will undergo vcc's with the Kr atoms in the cell, and will eventually thermalize. They will also undergo resonant charge exchange with the natural rubidium as described earlier.

The parameters of interest in our work include the charge exchange rate, the mean time for the ion to neutralize, and the relative velocity as a function of pressure. Dr. Hutton extracted this information using a time-dependent approach. He first assumed a Gaussian distribution of ions with a width $v_z^0 > u$ at time $t=0$, which thermalizes as a result of collisions with the Kr atoms in the cell, and so has a time dependent width $v_z^+(t)$. By including charge exchange, they calculated the width of the neutral isomers as a function of time, $v_z(t)$. They then time averaged $v_z(t)$ to get an average velocity of the neutral Rb isomers in the cell. The average velocity of the neutral isomer as a function of pressure for both values of a is shown in Fig. 3.1 (For a complete description of this non-thermal effect, see reference [12].)

The relative velocity depends on whether $a = +1$ or $-1/3$, but quickly approaches the thermal relative velocity above 500 mTorr. From Fig. 4.1 it can be seen that at lower pressures (≤ 100 mTorr) it is a very pronounced effect. This large relative velocity term at very low pressures means that the velocity distribution is very large, and so the number of homogeneous velocity groups will be greatly increased. Since the number of atoms is conserved, the number in each velocity group will be much less than at thermal velocity. Therefore the laser, which interacts with only one velocity group, will pump less atoms to the trapped level, decreasing the anisotropic signal. As seen later in this chapter, this effect greatly diminishes the signal-to-noise below 100 mTorr.

For our modeling, we used both a 's and averaged the corresponding relative velocities. We also used the charge exchange rate and mean time to neutralize provided by the authors as input into our model.

4.2 Modeling the System

After initially failing to produce a sub-Doppler signal experimentally (which involved months of work) using large cells at low pressure, we modeled the system in order to determine the proper experimental parameters for producing a change signal. We wanted

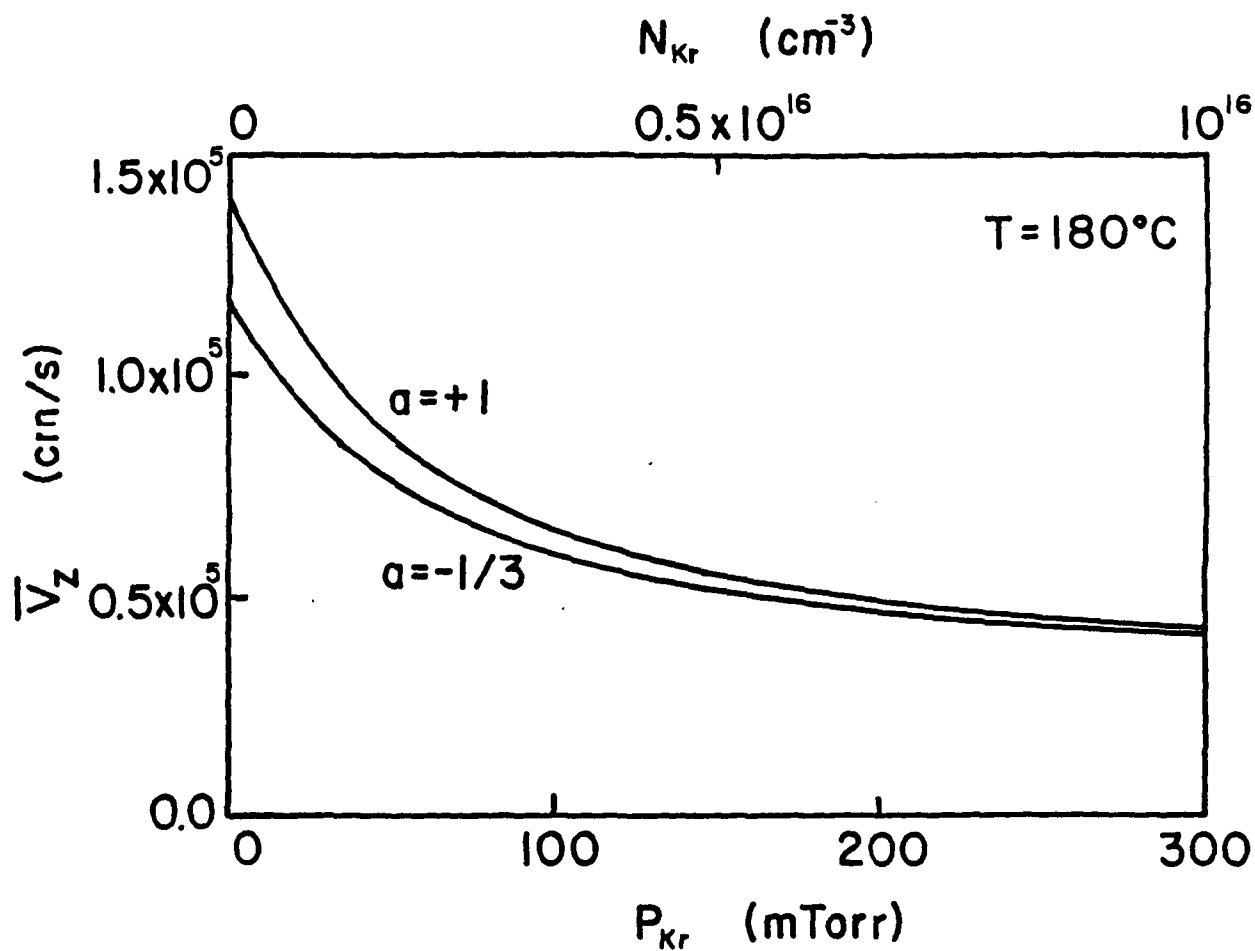


Figure 4-1: Calculated average velocity of the neutral ^{85m}Rb isomers in the cell vs. Kr density and pressure for the two cases $\alpha = +1$ and $\alpha = -1/3$.

specifically to determine the proper pressure and temperature at which to operate. The model is based on the theoretical model of laser optical pumping developed by Prof. Quivers [16], and is fairly simple. We group the sub-levels within a manifold that behave similarly when optically pumped into equivalent groups. This approach allowed us to reduce a 29-level model to a 3-level model, simplifying tremendously the computational effort necessary to solve the system.

Although we originally thought that two lasers were necessary for the experiment, the model showed that it was possible to produce a significant change signal with only one laser. This was an additional benefit from using the model, as a one laser experiment is much simpler to conduct than a two laser experiment. This model predicted fairly accurately the sub-Doppler signal we later observed. The details of that model are discussed in this section.

4.2.1 The Mathematical Model

As mentioned earlier, we chose to model optical pumping on the $S_{1/2} F = 5$ to $P_{1/2} F' = 4$ transition. The sub-level grouping is the same as given earlier: (1) level 1 is composed of the 9 $M_F = -4 \dots 0 \dots 4$ sublevels in the $F=5$ ground state; (2) level 2 is composed of the 2 $M_F = \pm 5$ sublevels in the $F=5$ level and (3) level 3 is composed of the 9 sublevels in the $F' = 4$ excited state. The $F=4$ level does not contribute to the population transfer to the 2 level, and is not included. The fact that atoms are lost to this level is included in the branching rate terms, which are reduced do to the presence of this level (see section 3.1). The three-level model is shown in Fig. 4.2.

The rate equations for the number of atoms in a particular velocity group, $N(v)$, can be written

$$\frac{dN_1}{dt} = -\frac{N_1 - N_3}{9}(R_+ + R_-) + \Gamma_{31}N_3 - \gamma_g N_1 + \mathcal{W}_g \mathcal{N}_1 + S, \quad (4.6)$$

$$\frac{dN_2}{dt} = \Gamma_{32}N_3 - \gamma_g N_2 + \mathcal{W}_g \mathcal{N}_2 + S_2, \quad (4.7)$$

3 LEVEL MODEL

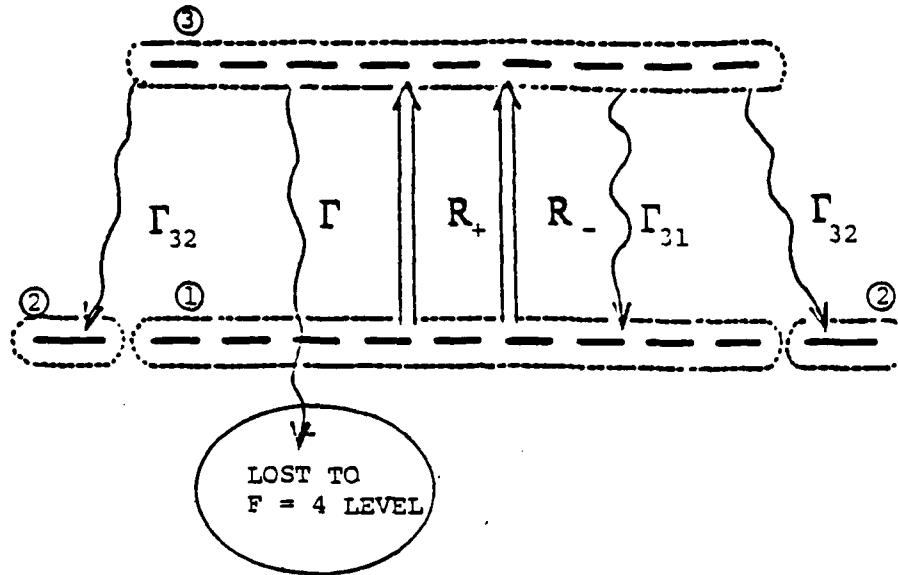


Figure 4-2: Three level model for optical pumping the D1 $F=5$ to $F'=4$ transition.

$$\frac{dN_3}{dt} = -\frac{N_3 - N_1}{9}(R_+ + R_-) - \gamma_e N_3 + W_e N_3, \quad (4.8)$$

with the components described below. The optical pumping rate produced by the laser is as given earlier

$$R_{\pm} = \frac{\sigma_H I}{\hbar \omega} \mathcal{L}_{\pm}$$

with the Lorentzian lineshape as

$$\mathcal{L}_{\pm} = \frac{\gamma_H^2}{(\omega - \omega_0 \mp kv)^2 + \gamma_H^2}$$

and the (+) and (-) terms here indicate the propagating and counter-propagating beams.

The excited state relaxation time is

$$\gamma_e = \frac{1}{\tau_{sp}} + \Gamma_{vcc} + \frac{1}{T}$$

and the ground state relaxation is

$$\gamma_g = \Gamma_{vcc} + \frac{1}{T}$$

with Γ_{vcc} as the vcc rate.

The production rate resulting from the β decay of the parent into the particular velocity group of atoms is given

$$S = \frac{9}{20} F_{CE} \Lambda n_{85kr} G(kv) \quad (4.9)$$

and the production rate into the trapped level is given

$$S_2 = \frac{1}{10} F_{CE} \Lambda n_{85kr} G(kv) \quad (4.10)$$

with Λ the krypton decay rate ($8.21 \times 10^{-12}/s$) which is a product of the decay rate of the ^{85}Kr and the branching ratio to the ^{85m}Rb state, F_{CE} the charge exchange rate extracted from Hutton's work (section 3.1.2), n_{85kr} the density of the radioactive krypton in the cell, and $G(kv)$ the Doppler distribution. The quantities $\Gamma_{F'F}$ are the branching ratios for the decay from the excited state. The quantity \mathcal{W} is the collision kernel in the strong collision approximation where one collision completely thermalizes the atom (i.e. it retains no memory of its velocity prior to the collision). This collision term represents atoms knocked into this velocity bin from another bin. The kernel can be written

$$\mathcal{W}_{g(e)} = \Gamma_{g(e)}^v G(kv). \quad (4.11)$$

The quantity

$$\mathcal{N}_i = \int N_i(v) dv \quad (4.12)$$

is the total population of the i 'th level.

The interpretation of the equations is straight-forward. For example, eqn (4.6) is read as follows: The rate change per unit volume of atoms in level 1 must be equal to minus those atoms that absorb photons from both laser fields and are excited to the higher energy level 3 plus those the decay by spontaneous emission back into level 1 minus those the leave the velocity group either by a vcc or gamma decay plus those that are

knocked into the velocity group by vcc's plus those that are "born" in the velocity group from the decay of the parent. The interpretation of the other equations is similar.

The equation can then be solved for the population excess in level 2, which is directly related to the anisotropy function

$$A \approx -P \approx \frac{\delta N_3}{N_3^{no\ optical\ pumping}}. \quad (4.13)$$

The difference between the anisotropy produced by two beams and that produced by one leads to the change signal. However, the above equation must be modified using a correction factor to account for the fact that the detectors are not point detectors. This correction factor has been calculated numerically by Dr. Shimkaveg [6][pgs. 146-150] as a function of the detector diameter (a) and the distance to the cell (d), and is given for our geometry at 0.86.

4.2.2 Numerical Solution of the Model

The coupled equations described above can be solved numerically. We solved them by two different methods and obtained identical results. The first method was a brute force technique where we chose a Δt and solved the equations for ΔN_i , subject to the constraint that the total population be conserved. We then used the new populations in the equations, and again solved them for ΔN_i . We continued this until there was no longer an appreciable change in the populations of the levels. We then used the excess population in level 2 to determine the anisotropy. This technique, though effective, was very time consuming computationally.

The second technique, written by Prof. Holbrow, employed the Gauss-Jordan matrix inversion technique to solve the steady state equations (placing the dN/dt terms equal to zero). This technique also is iterative, but takes much less computational time to solve.

4.2.3 Predictions of the Model

The predicted change signal at 300 mTorr produced by optically pumping with a single laser is plotted as a function of average intensity in Fig. 4.3. The change signal is composed of a narrow dip and broad pedestal as expected. The dip is fitted to a Lorentzian profile and the pedestal is fitted to a Gaussian profile. There are two key features of the signals; (1) The dip is power broadened at high intensities and (2) the dip to pedestal ratio varies as a function of intensity.

From Fig 4.3, it is clear the dip and the pedestal grow at different rates. The change signal is decomposed into a dip and pedestal, and the growth of each as a function of average intensity is plotted simultaneously in Fig 4.4. Notice that at intensities above 120 mW/cm^2 , the dip starts to saturate, and the pedestal dominates. At low pressure, and few vcc's, I_S is much less than I_{OP} , and it takes a lot of power to pump the pedestal. The opposite case occurs with many vcc's, where I_S is much greater than I_{OP} , and it takes a lot of power to pump the dip (see section 3.3).

4.3 Cell Design and Optimization

There are several considerations necessary when designing the optimum cell, in particular the pressure and the length and the radius. One also has to decide at what temperature to run the experiment, but that can be maximized experimentally once a cell is constructed. In this section we detail the procedure for design a suitable cell for the experiment. The important criteria in selecting the proper geometry is not just the amplitude of the dip at a particular pressure, but the count rate seen by the detectors. The quantity to maximize is the dip signal-to-noise, which gives the relative strength of a signal. This quantity is discussed next.

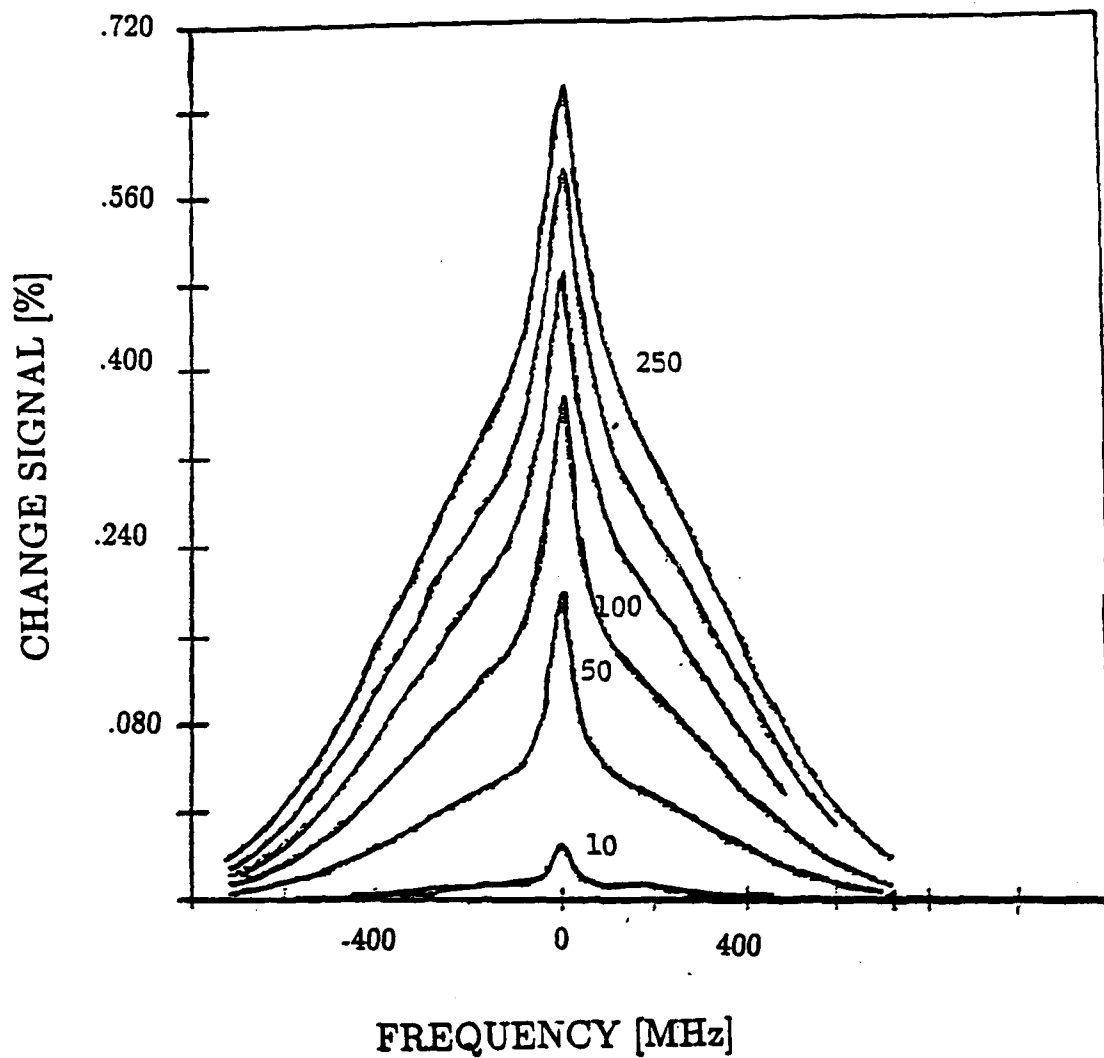


Figure 4-3: Change signal at 300 mTorr predicted by numerical model as a function of average intensity. A single laser was used to optically pump sample.

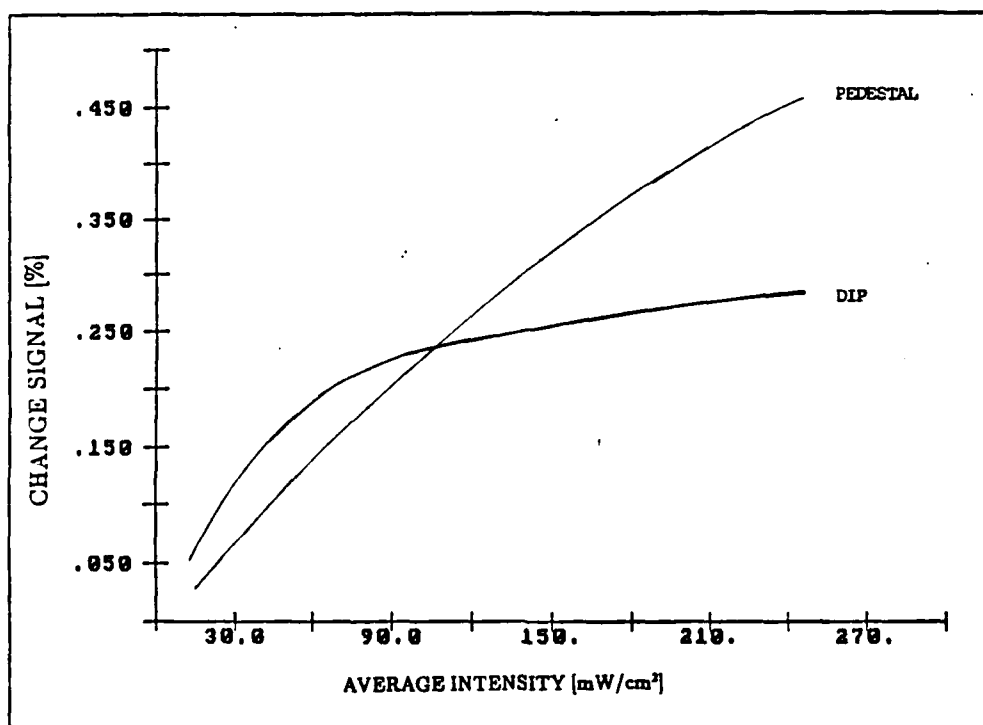


Figure 4-4: The change signal is decomposed into a Lorentzian dip and Gaussian pedestal, with the amplitude of each shown at various intensities.

4.3.1 Calculation of Signal-To-Noise

The signal-to-noise (S/N) function¹ is defined as the magnitude of the signal divided by its uncertainty and is given for the change signal as

$$S/N = \frac{D}{\Delta D}. \quad (4.14)$$

The value of D given earlier can be written as the difference between two anisotropies

$$D = A' - A_{Beam\ 2} \quad (4.15)$$

so that

$$\Delta D = \Delta A' - \Delta A_{Beam\ 2} \quad (4.16)$$

where

$$A' = \frac{N_{Both} - N_{Beam\ 1}}{2N_{off}} \quad (4.17)$$

and

$$A_{Beam\ 2} = \frac{N_{Beam\ 2} - N_{off}}{2N_{off}}. \quad (4.18)$$

The uncertainty in A can be written [6][pg. 145]

$$\Delta A = \frac{1}{\sqrt{N_{off}/2}} \quad (4.19)$$

or, using the fact that

$$N_{off} = \text{Total Count both Detectors} = 2N_{off\ Single\ Detector}, \quad (4.20)$$

we can write this as

$$\Delta A = \frac{1}{\sqrt{N_{off\ s.d.}}}. \quad (4.21)$$

¹Also called signal-to-Background since the background is really not noise.

Adding the two uncertainties in quadrature, then,

$$(\Delta D)^2 = \frac{1}{N_{off\ s.d.}} + \frac{1}{N_{off\ s.d.}} \quad (4.22)$$

and we get as our uncertainty

$$\Delta D = \frac{1}{\sqrt{N_{off\ s.d.}/2}} \quad (4.23)$$

with our signal-to-noise as

$$S/N = D\sqrt{N_{off\ s.d.}/2}. \quad (4.24)$$

What is important in this experiment is not the total signal-to-noise, but the signal-to-noise of the dip component of the change signal. So, when using the above expression for maximization, the change signal must first be decomposed into the dip and the pedestal. Only the amplitude of the dip is then used for comparison between intensities and pressures.

An expression for the count rate is given later, but clearly it is proportional to the number density of radioactive atoms in the cell, which is equal to

$$n_{85mRb} = (3.3 \times 10^{16} / Torr - cm^3) p_{kr} \quad (4.25)$$

where the numerical factor is just a conversion factor relating pressure to density using the natural gas law [6][page 68]. So, the S/N is then

$$S/N \propto \sqrt{p_{kr}} \quad (4.26)$$

and we can use this factor to pick the proper pressure to operate at if we know the amplitude of the dip there, which we do from our model.

4.3.2 Dip Amplitude vs. Pressure

Using our model, we looked at the amplitude of the dip (A_{Dip}) in the range from 80 mTorr to 450 mTorr. The dip amplitude for several average intensities is plotted vs. pressure in Fig. 4.5. The results are quite interesting. Note that the dip starts to decrease relatively fast beyond 300 mTorr, which is not surprising, as the vcc rate is increasing and washing out the dip. However, it is also decreasing below 100 mTorr, which may seem surprising at first, but actually is expected from Dr. Hutton's work. Recall (Fig 4.1) that below 100 mTorr the relative velocity between the isomer and the krypton atom starts to climb very quickly due to the low density. At a pressure of 80 mTorr, the ku width of the distribution is estimated by Hutton at 840 MHz, which means the number of velocity bins in the Doppler profile has increased substantially. The number of atoms in each bin therefore decreases, and so the amount of population transferred decreases also, making the dip smaller.

Now, using this curve, and the proportionally relationship between the amplitude and the square root of the pressure, we can plot the relative S/N as a function of pressure. This is done in Fig 4.6. From this figure it is clear that the S/N is maximized around 300 mTorr, and that any pressure in the range 250-350 mTorr would be acceptable.

Now, having chosen the pressure, we can design the proper geometry for the cell.

4.3.3 Absorption Effect on Average Intensity

The model we used above to predict the change signal was based on using the average intensity in the cell. The intensity in the cell at any location can be written [6][page 195]

$$I(\rho, z) = \frac{P}{\pi a^2} [\exp -(\alpha z)] [\exp -(\frac{\rho}{a})^2] \quad (4.27)$$

where P is the incident power, a is the 1/e half-width of the beam, α is the absorption coefficient, ρ is the radius of the cell at any point out to R, and z is the location along the axis of the cell to any point out to L. The average intensity in the cell can then be

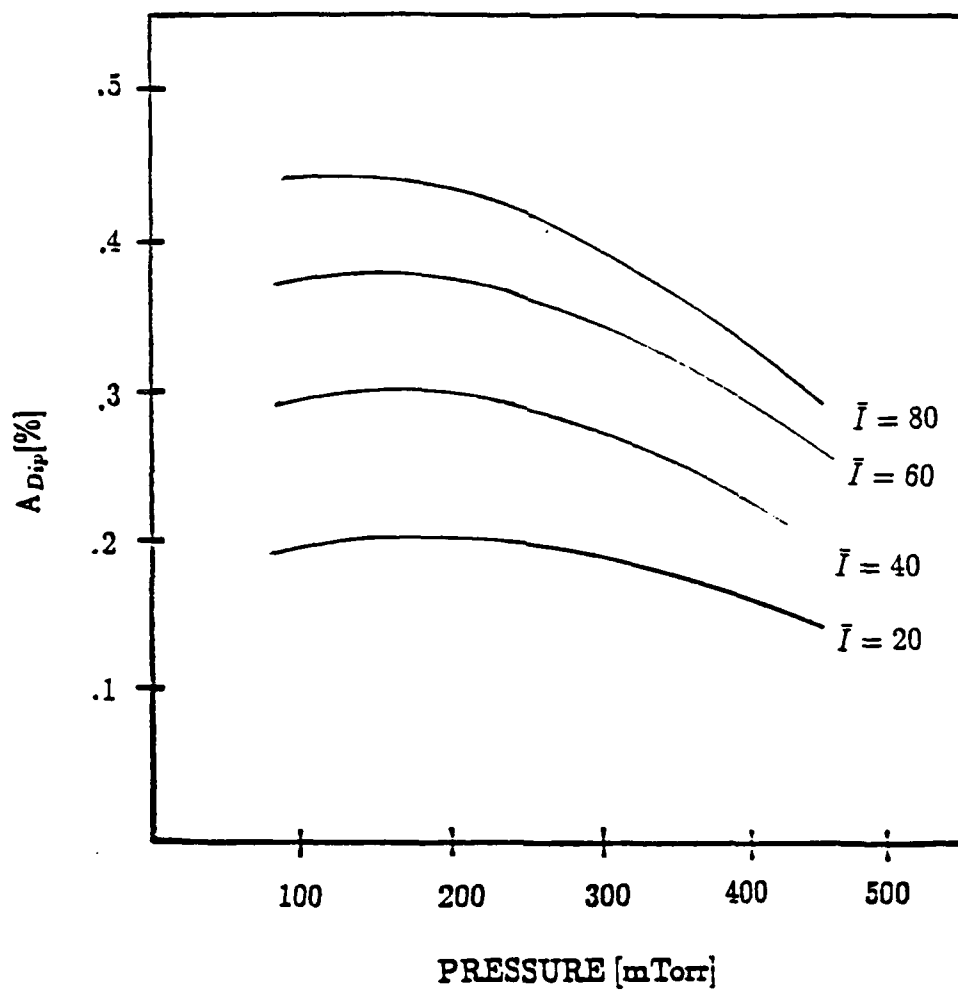


Figure 4-5: Dip amplitude vs. pressure at various values of \bar{I}

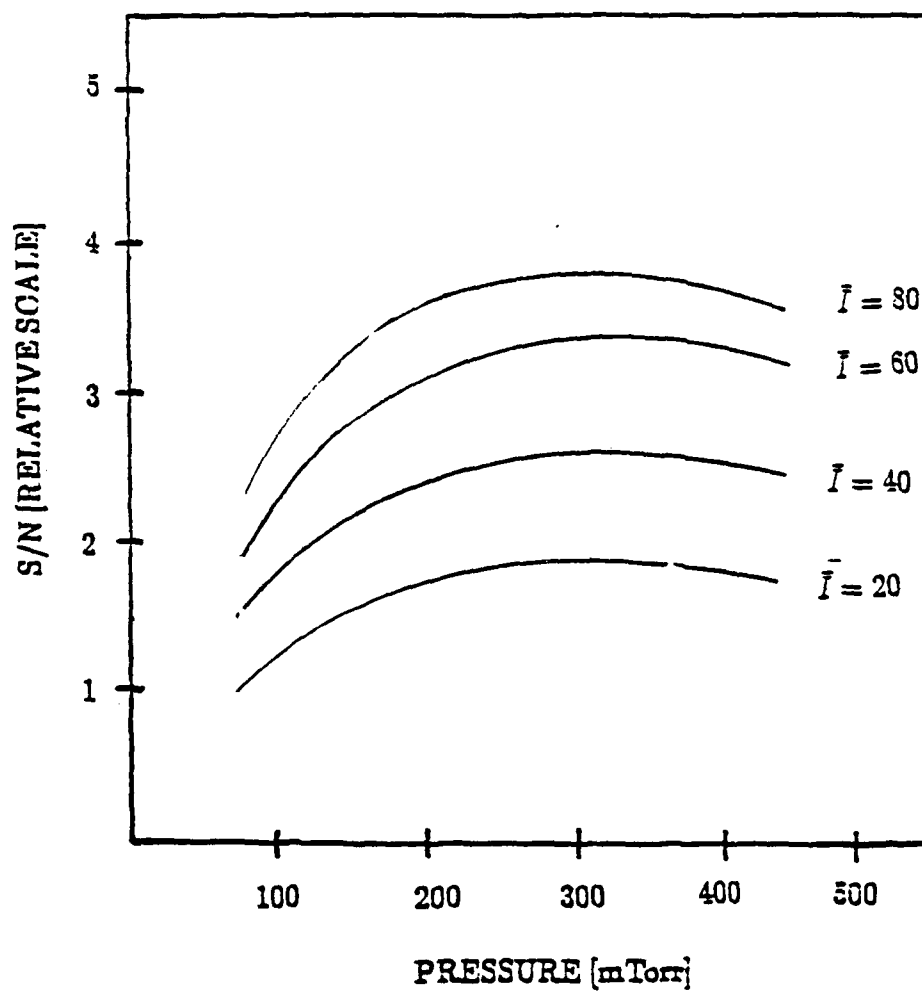


Figure 4-6: Relative S/N vs. pressure for various values of \bar{I} . S/N in arbitrary units, pressure in mTorr.

written

$$\bar{I} = \frac{1}{\alpha L} \left(\frac{a}{R}\right)^2 [1 - \exp -(\alpha L)] [1 - \exp -(\frac{R}{a})^2]. \quad (4.28)$$

Dr. Shimkaveg has done extensive work on cell design to maximize anisotropy. He has found that it is maximized when $(R/a)^2 = \alpha L = 2.01$ [6][pg. 200], where a is the 1/e half-width of the laser beam, R is the radius of the cell, α is the absorption coefficient, and L is the length of cell. We are also interested in maximizing the anisotropy, since it is the difference between the anisotropy produced by the two beams and that produced by the one beam that we actually measure. So, using these criteria, we must develop a method for choosing R and L that maximizes the dip signal-to-noise. Prior to doing that, however, we will first discuss the quantity α that appears in the above equation, and also the signal-to-noise function.

The Absorption Coefficient

The absorption coefficient due to background absorption by the natural rubidium can be approximated

$$\alpha = fn_{Rb} + gn_{Rb}p_{Kr} + hn_{Rb}^2 \quad (4.29)$$

where f , g , and h are a function of laser detuning from natural rubidium line center, and p_{Kr} is the krypton pressure in Torr. Following Shimkaveg [6][page 213], to estimate α we use the values of the parameters evaluated at -5049 MHz from ^{85}Rb line center, i.e.,

$$f = 6.28 \times 10^{-16} \text{ cm}^2$$

$$g = 1.67 \times 10^{-15} \text{ cm}^2/\text{Torr}$$

$$h = 5.95 \times 10^{-30} \text{ cm}^5.$$

Using these values, we can compute the α at various temperatures from 140°C to 170°C, the range of temperatures at which we can conduct the experiment, using the krypton pressure of 0.3 Torr. These temperatures are fairly close to the limits dictated by charge exchange and spin exchange. For example, at temperatures below 135°C there

is no appreciable experimental anisotropy measured, primarily because the density of natural rubidium in the cell is too low to provide for adequate charge exchange. Above 180°C the effects of spin exchange start to greatly diminish the signal [6].

4.3.4 Maximizing Signal-to-Noise

The S/N function for the dip can be written

$$S/N_{Dip} = A_{Dip} \sqrt{N/2} \quad (4.30)$$

where A_{Dip} is a function of average intensity, given in Fig. 4.7.

Using the expression for average intensity from above, and using the criteria for maximizing anisotropy, $\alpha L = (R/a)^2 = 2.01$, the average intensity can be written

$$\bar{I} = \frac{P}{\pi a^2} (0.1746) \quad (4.31)$$

or

$$a^2 = \frac{P}{\pi \bar{I}} (0.1746) \quad (4.32)$$

or, using the $R^2 = 2.01a^2$

$$R = \sqrt{(2.01) \frac{P}{\pi \bar{I}} (0.1746)} \quad (4.33)$$

and, finally, inserting the available power, $P = 150$ mW, we can write

$$R(\bar{I}) = 4.0935 \sqrt{\frac{1}{\bar{I}}} \quad (4.34)$$

where \bar{I} is given in mW/cm².

Now, at a fixed point into the cell we can write our S/N_{Dip} as

$$S/N_{Dip} = C A_{Dip} R \quad (4.35)$$

where C is a constant and includes the value of z , and the expression can be evaluated as a function of \bar{I} only, using Fig. 4.7. The expression maximizes at $\bar{I} = 27mW/cm^2$ where $A_{Dip} = 0.00075$ and $R_{optimum} = 0.79$ cm.

In a similar fashion, we can fix the radius and write the S/N_{Dip} as

$$S/N_{Dip} = C_1 A_{Dip} \sqrt{L} \quad (4.36)$$

where C_1 includes the value of the radius.

We can use the fact that the A_{Dip} is proportional to the charge exchange fraction, which at a constant pressure is a function of temperature, and the fact that α is also a function of temperature, and determines L using $\alpha L = 2.01$. The expression becomes

$$S/N_{Dip} = C_2 F_{CE} \sqrt{2.01/\alpha}. \quad (4.37)$$

The charge exchange fraction can be written

$$F_{CE} = \frac{\Gamma_{CE} T_{avg}}{\Gamma_{CE} T_{avg} + 1} \quad (4.38)$$

where

$$\Gamma_{CE} = n_{Rb} \sigma_{CE} v_{rel}$$

has been given earlier and T_{avg} is the lifetime of the isomer. Using the v_{rel} from Hutton's work, and the α from above, we find the optimum temperature at 165° C, and the optimum length of the cell at $L = 6.42$ cm.

Predicted Counting Time

Having determined the optimum cell, with $R = 0.79$ cm, $L = 6.42$ cm, and $V = 12.587$ cm³, we can calculate the amount of time necessary to count to obtain a statistically significant signal.

The number of decays seen by a detector can be written

$$N = \Lambda \frac{\Omega}{4\pi} \epsilon \eta n_{kr} (\pi R^2 L) t_c \quad (4.39)$$

where $\Lambda = 8.21 \times 10^{-12}$ is the activity defined earlier, $(\Omega/4\pi) = 0.06$ is the normalized solid angle, $\epsilon = 0.27$ is the concentration fraction of radioactive Kr, $\eta = 0.32$ is the detector efficiency, $n_{kr} = 0.99^{16} \text{ cm}^{-3}$ is the Kr density and t_c is the counting time in seconds. Now, recall that from above

$$S/N_{Dip} = A_{Dip} \sqrt{N/2}$$

using the expression for N , we can solve for the counting time

$$t_{counting} = \frac{(S/N)^2}{A_{Dip}^2 2.65 \times 10^3} \quad (4.40)$$

Then considering the S/N that we require, we can predict the necessary counting time. To establish that we have a real change signal, we using the criteria $S/N = 4$ (10,000 to 1 odds). At the chosen $\bar{I} = 27 \text{ mW/cm}^2$, we expect an $A_{Dip} = 0.00075$ so we get $t_c = 1.0734 \times 10^4$ seconds or 3.0 hours.

Actual Cell

As it turned out, we did not have to construct a sub-Doppler cell to use for our first attempt. Dr. Shimkaveg had actually made several low pressure cells for his attempt at a sub-Doppler signal, at various sizes and pressures. We analyzed the S/N for the existing cells. Although not optimized, we found one that was acceptable with a $R = 0.60 \text{ cm}$ and $L = 4.2 \text{ cm}$. Operating at a temperature of 150°C , we had an $\alpha L = 0.5872$, and using $(R/a)^2 = 2.01$, we had an average intensity of 94 mW/cm^2 with a predicted

$A_{Dip} = 0.00126$. So, comparing the S/N of this cell to the idealized cell

$$S/N_{(Actual/Optimum)} = \frac{A_{Dip\ actual} R_{Actual} \sqrt{L_{Actual}}}{A_{Dip\ Optimum} R_{Optimum} \sqrt{L_{Optimum}}} \quad (4.41)$$

where, upon substituting the appropriate values, we get a ratio = 0.83, meaning that this cell was within 83% of our optimum. So this is the one we used, with the results given in the next chapter.

Chapter 5

Experiment Results and Analysis

This chapter describes the actual experiment and is divided into four sections: (1) general description and experimental arrangement; (2) experimental apparatus; (3) the results; and (4) the analysis.

5.1 General Description and Experimental Arrangement

A schematic of the experiment is shown in Fig. 5.1 and described in the following way. A cell containing radioactive krypton gas is maintained in a controlled thermal and magnetic environment. The output from a narrow frequency high intensity dye laser has two low intensity beams sequentially split from the main beam to be used for frequency control. The first beam goes to a reference cell containing natural rubidium and is used to produce Lamb dips, and the second beam goes to a 1.5 GHz Fabry-Perot spectrum analyzer. The remainder of the output is sent through a 50-50 beam splitter, providing two equal intensity beams. The first beam is incident upon a shutter, which when open allows the beam to enter the cell. A lens is placed between the shutter and the cell to control the size of the beam entering the cell. Similarly, the second beam is brought around to the rear of the cell using mirrors, and is incident upon a second shutter, which

when open allows the beam to pass through a lens into the rear of the cell. When both beams are in the cell, they form a standing wave. The amount of time the beams are on and off is controlled by the computer which sends a voltage to each solenoid to open or close it as programmed. The gamma rays emitted from the cell are detected by 3-inch NaI(Tl) detectors, with the output fed through a nuclear electronics package, and into a computer where the anisotropy is calculated.

5.2 Experimental Apparatus

For convenience in discussing the apparatus used, this section is further divided into three functional areas: (1) target cell and its environment; (2) optical pumping source and frequency monitoring apparatus; (3) nuclear data acquisition and control electronics. We will provide here a functional description of the apparatus. Since the "home-built" equipment such as the cells, the oven, and the preamp for the nuclear electronics package was built by Dr. Shimkaveg, the reader is referred to his thesis for construction details.

5.2.1 Cell-Gas System

A pyrex cell is 40mm long and 12mm in diameter and is filled with 300 mTorr of Kr containing 1 mCi of 10.7-y ^{85}Kr . The cell is placed inside an oven, with the temperature maintained at 150°. The oven consisted of three pieces: two end pieces with 1-in diameter quartz windows to allow the light through, and a central core consisting of commercial fire brick with a 2.25 inch cylinder hole for cell placement. Resistive nichrome heating wire was imbedded in each end piece, while the central piece was left unheated, so that the end pieces would be hotter. This design was used to keep the cell windows hotter than the center of the cell. If the windows were not hotter, then the rubidium vapor would condense on them, and block the incoming light. A single DC power supply, operating at approximately 20 volts, was used to provide current to both end plates in parallel. Initially, the rear of the cell was cooler than the front, as we did get some condensation

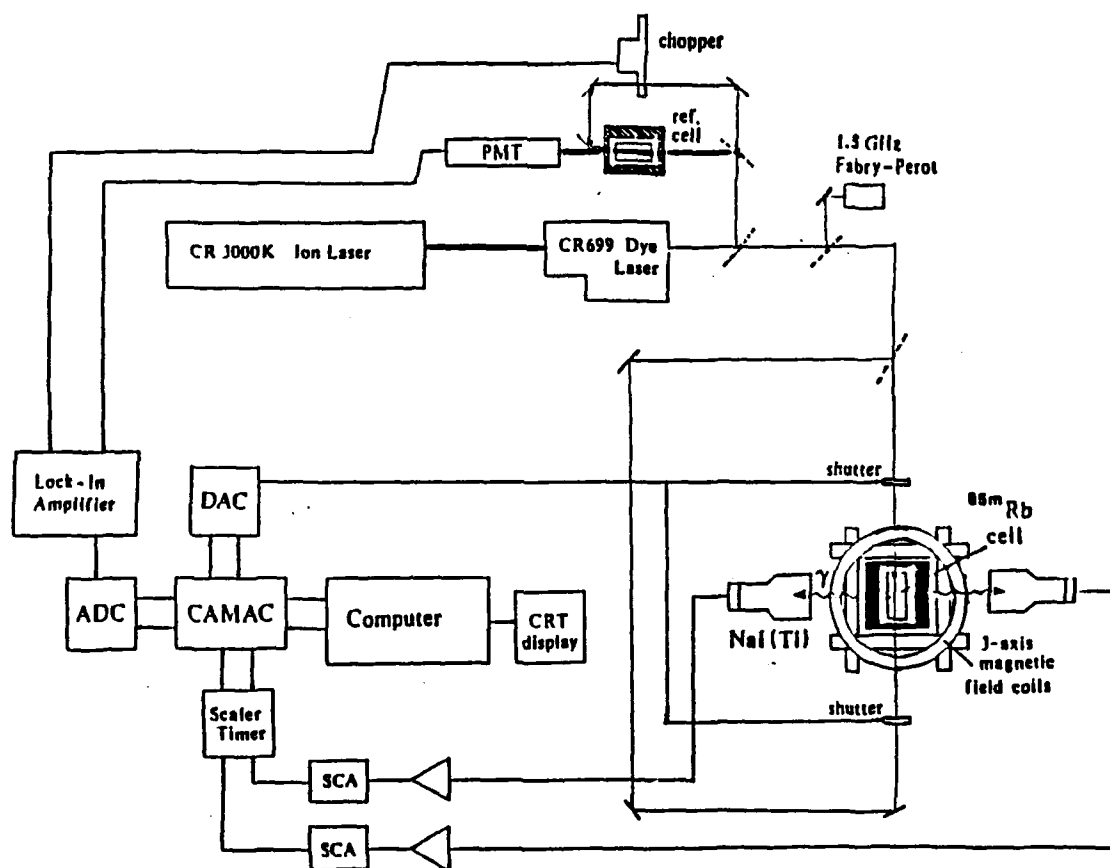


Figure 5-1: Schematic diagram showing experimental arrangement.

on the window. We corrected this by placing a variable resistor in series with the front heating element and adjusting it until the two windows were clear. We also drilled some holes in the center of the cell to make it slightly cooler than the end. This seemed to work quite well, and we were able to clear the windows.

The magnetic field is controlled by a three-axis Helmholtz coil arrangement, each coil with its own independent current source. To set the field we used a three-axis hole effect probe. Using this probe, we first nulled the earth's magnetic field, and then established a 1 Gauss B field along the quantization axis (perpendicular to the direction of propagation of the beam). Our initial attempt to reproduce Dr. Shimkaveg's results failed, however, because we set the field incorrectly the first time. The field actually quenched the signal. This was discovered by turning off the field altogether, and running the experiment. Our results doubled. We then reset the field properly and maximized the signal as a function of field amplitude. It turns out that the signal reaches a maximum at about 0.5 Gauss, and stays flat above that. However, as the field increases from 0.5 Gauss to 1 Gauss, we found that the count rate in the detectors decreased by 15% due to interference with the NaI(Tl) detectors. Therefore, we set the field at 0.5 Gauss.

5.2.2 Laser Frequency Location

In our work, we were able to achieve excellent precision using the Coherent CR699-29 Autoscan Dye Laser, pumped with a 3000K Coherent krypton cw laser. The Autoscan is the state of the art dye laser, designed to allow the user to select by computer any frequency within the dye range (in this case for LD700 that means from 700nm-800nm), do seamless scans across large frequency ranges (100 cm^{-1}), and allow for input from three data channels while scanning for later analysis. The controller is an Apple IIe computer with software designed to locate the laser to $\pm 3\text{MHz}$ inputs. When a desired laser frequency is input into the program, the laser first locates itself by using its specially designed wavemeter located at the output of the dye laser, then moves different tuning elements in the laser to bring itself to the specified frequency, re-reads its location, and

retunes until it is within the 3 MHz specified. The wavemeter is calibrated with known reference frequency, which in our case is the $F=2$ to $F'=1$ Lamb dip transition (see below). Once it is calibrated, it only needs to be re-calibrated if the laser itself is re-aligned. During a scan the three data channel analog inputs are converted to digital signals, and displayed on the monitor as a function of frequency, with the Autoscan program locating any point on the signal to ± 3 MHz.

Although the system works well at 795 nm and 780 nm, its performance is guaranteed only to 750 nm. Therefore, we devised a procedure to insure correct frequency location. We first located the ^{87}Rb $F=2$ to $F'=1$ transition using the Lamb dips input into a data channel. We then performed a series of scans through the Lamb dips, and used the ground state splitting of ^{87}Rb (which is known to very high precision) to determine a scan error. The scan error is usually very small, approximately 0.5% or less. A larger error typically implies improper alignment which must be corrected. (Of course one could also use the ground state splitting of ^{85}Rb to calibrate the scan error, but since we decided to use the outlying ^{87}Rb transitions which are closest to the $^{85\text{m}}\text{Rb}$ transitions as frequency references, we used ^{87}Rb .)

We calculated the frequency difference between the reference transition and the desired location and sent the laser there. Once there, we scanned the laser back through the known reference point and read the location of the transition on the autoscan monitor. We then applied the correction factor previously determined. This procedure allowed us to locate ourselves within ± 6 MHz of the reference transition. (In theory, we should be able to locate ourselves even more precisely since the autoscan program will digitize the input signal into 1 MHz samples. However, it will only print the location to 3 MHz precision. We did at one time attempt to modify the autoscan program to achieve this higher precision, but were unsuccessful.)

As an independent test of this procedure, we calibrated a 1.5 GHz spectrum analyzer using the same ground state ^{87}Rb splitting, and fed that signal into a separate data channel while we scanned the laser. We then measured the frequency difference between

the reference transition and the start location using the calibrated spectrum analyzer, an obtained agreement within the uncertainty claimed.

The Lamb dip signals are obtained by utilizing a standard pump-probe arrangement. The probe beam is split from one of the frequency monitoring beams mentioned earlier, and sent through a natural rubidium reference cell into a photomultiplier tube (PMT). The rest of the beam is sent through a reference chopper, then into the rear of the cell. When the beam is on a resonance, a very narrow Lorentzian dip is produced. The output from the PMT is fed into a lock-in amplifier, and the amplified signal is sent to the autoscan data input channel.

5.2.3 Data Acquisition

The experiment is controlled by a program on an IBM-PC, written in the ASYST language, a special language designed for control of laboratory equipment and for data analysis. The program controls the timing sequence of the shutter, following the sequence described in section 4.3.1, to produce a change signal. Additionally, the program also controls a standard scalar-timer where the number of gamma rays detected in a specified time frame is recorded. Finally, the program will calculate the change signal from the data input from the scalar timer.

The gamma rays are detected with two 3-in NaI(Tl) detectors placed up to the oven wall, about 1.5 inches from the center of the cell. The detectors are maintained at 1200 volts by a regulated high power supply. The incident gamma rays produce a voltage pulse which is fed through a pre-amplifier into an amplifier and then into a single channel analyzer (SCA). The amplitude of the pulse is proportional to the amplitude of the gamma ray detected.

The single channel analyzer is set to allow only certain voltage pulses through, in order to eliminate background radiation. The output from the SCA is sent to a scalar-timer, where the number of counts in a specified time is recorded. That count is then sent to an IBM-PC, where the number of counts is recorded and used to compute the

anisotropy.

5.3 Results

The results of both the Doppler-broadened experiment and the Sub-Doppler Experiment are presented. The Doppler-broadened results established the fact that one laser pumping would indeed produce a measurable signal. Additionally, it gives a measure of the strength of the different transitions. The sub-Doppler results yield information as to the location of the ^{85}Rb transitions.

5.3.1 Doppler-Broadened One Laser Pumping

Initially it was thought that two lasers were needed to produce an anisotropy signal, due primarily to the fact that population was lost to an unpumped level. However, our computer model showed that a single laser did provide a substantial signal. This surprised us, and actually cast doubts on our model. However, we decided to try single laser pumping to reproduce Dr. Shimkaveg's results, and indeed we were able to do so as seen in Fig. 4.1 and 4.2.

From these results, the transitions can be categorized as follows: (1) the $\Delta F = -1$ transitions, which push population to the high M_F sublevels, produce a positive anisotropy and are quite strong, reflecting the strength of the matrix elements of the pumping, and the relative weakness of the matrix elements of the unpumped level; (2) the $\Delta F = +1$ transitions, which push population to the lower M_F sublevels, produce negative anisotropy and are still relatively strong; and (3) the $\Delta F = 0$ transitions, which push population to the lower M_F sublevels, produce negative anisotropy, and are very weak.

However, there were substantial difference from Dr. Shimkaveg's results in the relative amplitudes of the transitions, notably those with $\Delta F = 0$. (Note that certain transitions are substantially larger than those produced by Dr. Shimkaveg. This is because the laser he used had a defective element, which when corrected allowed the laser to produce

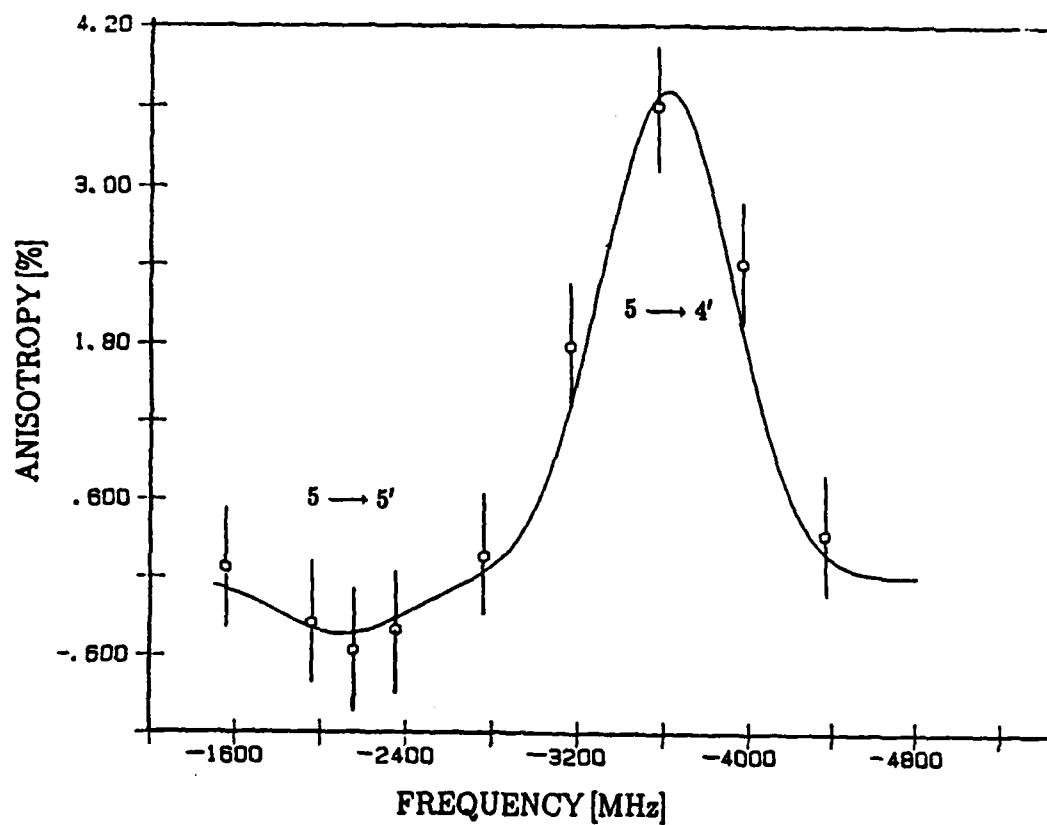


Figure 5-2: Single laser Doppler-broadened results on the low energy $^{85\text{m}}\text{Rb}$ D1 transitions using original 4 Torr cell with 300 mW of power. Frequency is reference to ^{87}Rb $F=2$ to $F'=1$ transition.

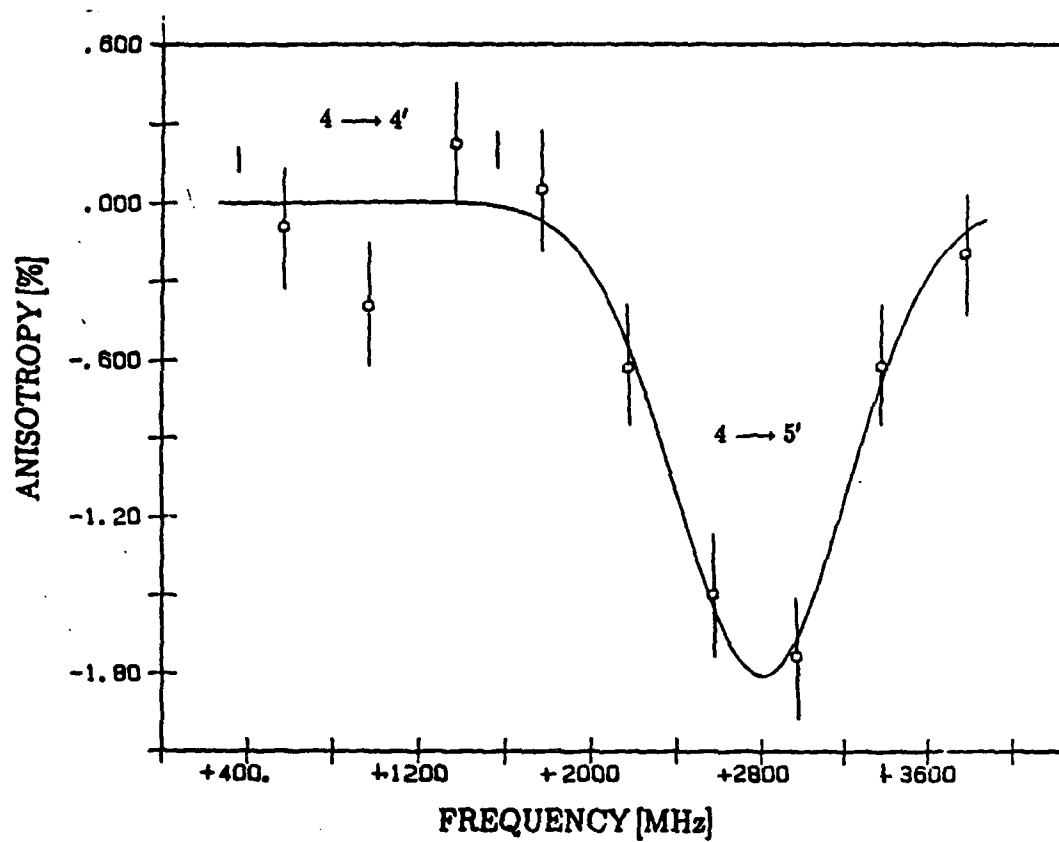


Figure 5-3: Single laser Doppler-broadened results on the high energy $^{85\text{m}}\text{Rb}$ D1 transitions using original 4 Torr cell with 300 mW. Frequency is reference to ^{87}Rb $F=1$ to $F'=2$ transition.

Transition	Two Laser Amplitude [%]	One Laser Amplitude [%]	$\frac{\text{Amplitude}_{\text{Two Laser}}}{\text{Amplitude}_{\text{One Laser}}}$
D1 $F=5 \rightarrow F'=4$	1.3	1.5	1.2
D1 $F=5 \rightarrow F'=5$	-0.70	-0.23	3.04
D1 $F=4 \rightarrow F'=4$	—	—	—
D1 $F=4 \rightarrow F'=5$	-1.5	-0.70	2.1

Table 5.1: Single Laser Optical Pumping on the D1 with Doppler broadened transitions contrasted with two-laser pumping (from Shimkaveg)

approximately twice its previous power. This large power allowed us to produce a larger signal with one laser than Dr. Shimkaveg had been able to produce with two.) To discern the effect of the second laser, we ran the experiment at the same power that Dr. Shimkaveg used (150 mW). We ratioed the two laser results to the one laser results to determine some measure of the enhancement effect of the second laser. The results are shown in table 5.1. Several points are made clear. Just as one would expect, the second laser enhancement is most pronounced on the $F=4$ to F' transition ($\Delta F = 0$). This is because in the one laser pumping scheme, the population lost to the unpumped $F=5$ level is relatively large due to the strong matrix elements between the $F=5$ and $F'=4$ level. Also, as one would expect, the effect is very weak for the $F=5$ to $F'=4$ transition, for just the opposite reason. The effect on the $F=4$ to $F'=5$ case is intermediate between the two.

5.3.2 Sub-Doppler Experimental Results

Once we realized that we could effectively optically pump with one laser, we considered the idea of "Lamb dipping" the signal. After our modeling predicted success (chapter 4), we attempted our first sub-Doppler change signal. The initial change signal was produced by optically pumping the D1 $F=5$ to $F'=4$ transition and is shown in Fig 5.4. The dashed line is the predicted value using the model discussed in section 4.3, and is in good agreement with the actual results. Just as we did with the results of the model, we least-square fit the experimental results to a Lorentzian dip (45 MHz HWHM) and a Doppler-broadened pedestal ($ku = 534$).

The frequency locating technique described above was not used for this data collection, as it was done before we developed that technique. Instead, we simply used the Autoscan wavemeter directly to locate ourselves in frequency space. We also did not correct for frequency drift as we did later on. Having said that, the signal and its location in frequency space are virtually identical with that found using the more sophisticated technique. This is because the Autoscan system is quite powerful and quite precise when properly aligned, as it was in this case. Nevertheless, to assure correct frequency location we developed the alternate technique, and retook the data as described below.

5.3.3 D1 and D2 Summary Results

We re-measured the D1 transitions with the frequency selection technique described earlier. Those results, as well as our D2 results, are presented in Tab. 5.2. The measurements were made using the ^{87}Rb Lamb dip transitions for reference as described above. The locations were then calculated with regard to the ^{85}Rb line center using the known hyperfine A and B values for ^{87}Rb [18] and the known isomer shift value for ^{85}Rb to ^{87}Rb measured by Thibault [19]. D1 and D2 line centers are the calculated frequencies in the absence of hyperfine structure. The value of ku used is 523 MHz, determined from the D1 measurements, and quite close to the original (534 MHz) Doppler width measured at 300 mTorr.

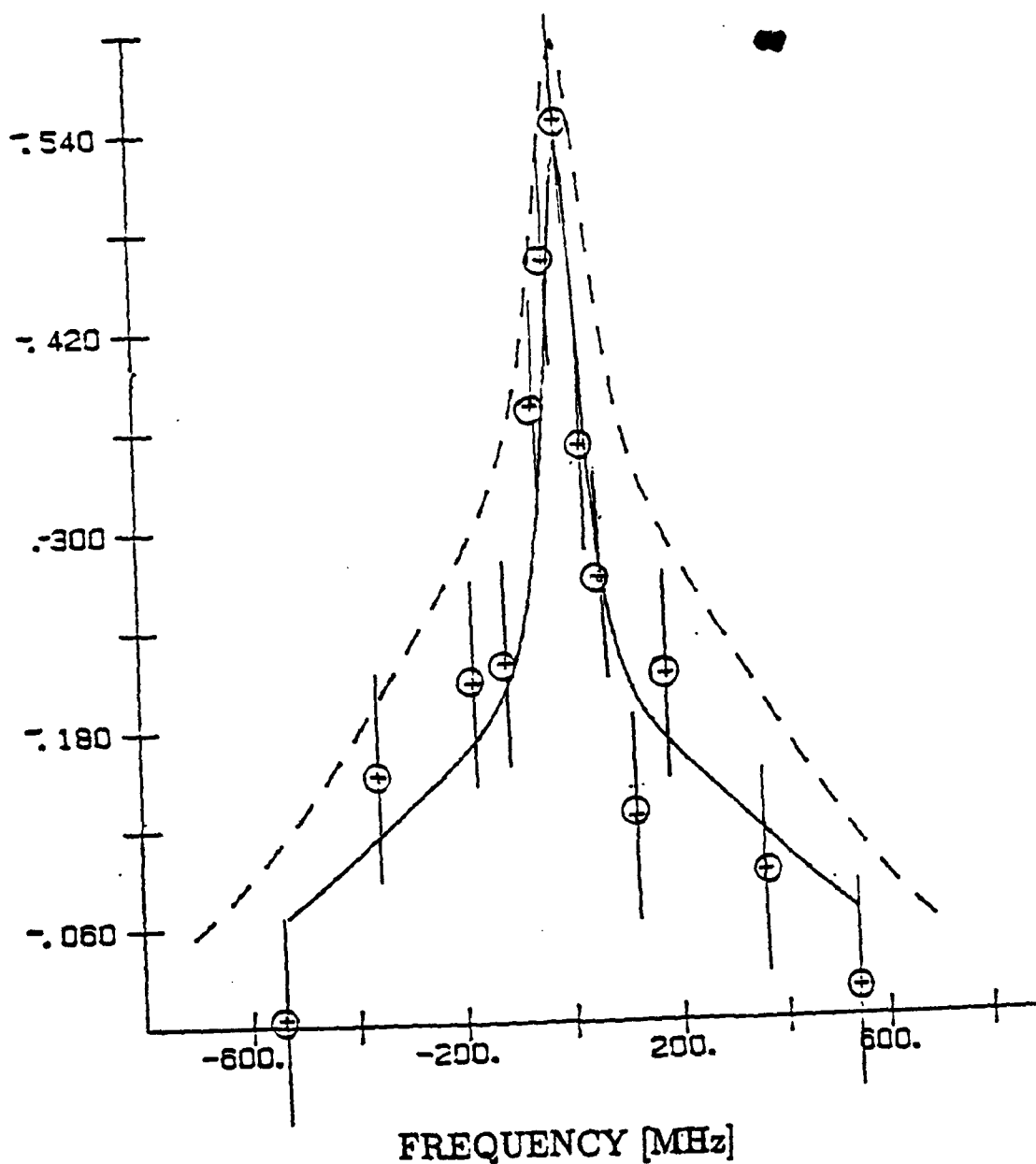


Figure 5-4: Initial sub-Doppler change signal produced by single laser optical pumping with 300 mW on $F = 5 S_{1/2}$ to $F' = 4 P_{1/2}$ transition. Cell pressure is at 300mTorr. Solid line is a least-square fit to a Lorentzian and Doppler composite curve. Frequency is reference to peak location. Dashed line is signal by our model.

Type Of Transition	Observed ^{85m} Rb Transition	⁸⁷ Rb Reference Transition	$\Delta\nu$ Observed (± 6 MHz)	$\Delta\nu$ reference ⁸⁵ Rb Line Center (± 6.5 MHz)
D1	F=5 \rightarrow F'=4	F=2 \rightarrow F'=1	-3602	-6593
D1	F=4 \rightarrow F'=5	F=1 \rightarrow F'=2	2800	7457
D2	F=5 \rightarrow F'=4	F=2 \rightarrow F'=1	-3291	-5932
D2	F=5 \rightarrow F'=6	F=2 \rightarrow F'=1	-2641	-5354
D2	(6 \rightarrow 5) Crossover	F=2 \rightarrow F'=1	-2806	-5519

Table 5.2: Results of measurements on the D1 and D2 transitions. Measurements are made with reference ⁸⁷Rb transitions, and given with regard to calculated ⁸⁵Rb line center.

The D1 $F = 5$ to $F' = 4$ transition is shown in Fig 5.5, the D1 $F=4$ to $F'=4$ transition is shown in figure 5.6, and the D2 transitions are shown in Fig 5.7. The relative location of all the transitions is shown in Fig. 5.8.

The results are predictable. For the D1 transitions, the strongest peak is the $F=5$ to $F'=4$ transition, and the change signal has a negative sign as expected. The $F=4$ to $F'=5$ transition is fairly strong also, with a positive change signal. The widths of the dips are about equal. The $\Delta F = 0$ transitions are too small to measure.

The D2 transitions are also predictable. The $F=5$ to $F'=6$ transition is very strong, and is positive. It is a particularly strong transition since population optically pumped to the $F'=6$ level cannot decay to the $F=4$ level due to the selection rule $\Delta F = 0, \pm 1$. The $F=5$ to $F'=4$ transition is relatively strong, as expected, and negative. The $F=5$ to $F'=5$ transition does not appear, which is not unexpected.

The appearance of the crossover between the $F' = 6$ to $F' = 5$ transition is also predictable. Although the $F=5$ to $F' = 5$ transition is very weak, it is still pushing population towards the lower M_F sublevels, just as the $F=5$ to $F' = 6$ transition is. This is why there is a crossover transition between them. On the other hand, the $F=5$ to $F' = 4$ transition is pushing population the other way, so the tendency is to cancel out, and therefore no crossover appears. The widths of the signals are consistent with expectations also, and are within 20 % of each other. The $F=5$ to $F' = 4$ signal is narrower than that of the $F=5$ to $F' = 6$ signal, indicating a larger saturation intensity (as expected from examining the matrix element [Appendix 1]).

5.3.4 Determination of Uncertainty

To determine a measure of the uncertainty in the location of our peaks, we added to the change signal amplitude of every other frequency point its uncertainty, and to the in between points we subtracted the uncertainty. We then refit the data and determined a new location. We then reverse the process, changing plus to minus, and refit the data. We averaged the two results, and the difference between that result and the actual result

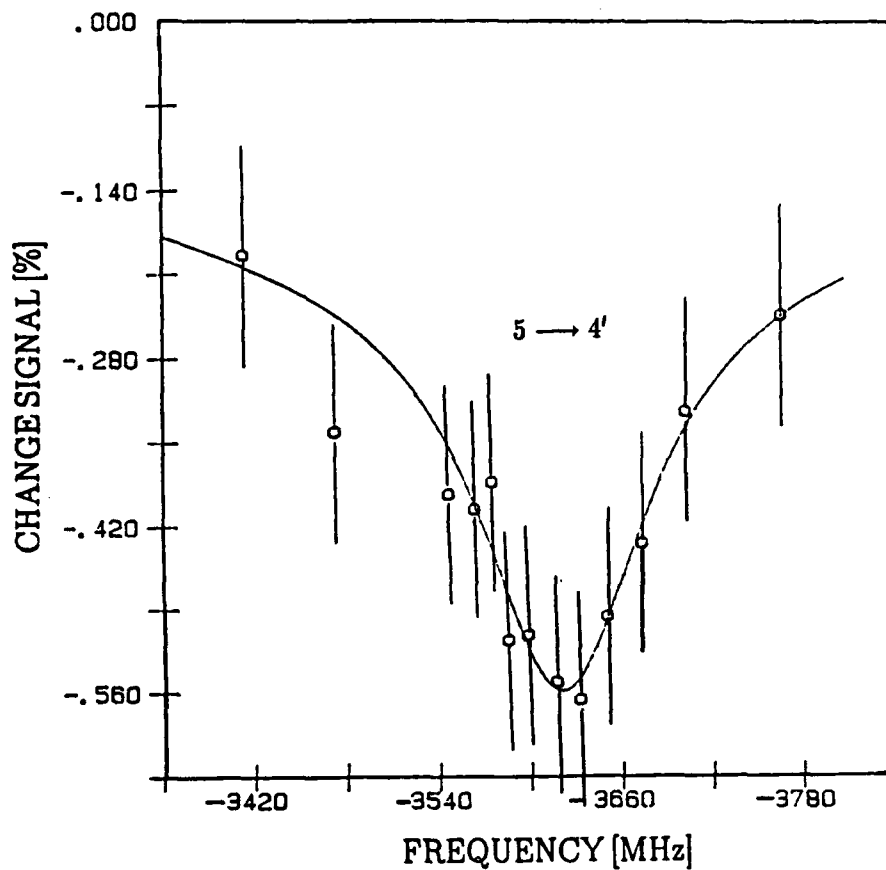


Figure 5-5: Observed gamma ray change signal for ^{85m}Rb D1 $F = 5$ to $F' = 4$ ^{85m}Rb transition. Transition pumped with 300 mW total power, at cell pressure of 300 mTorr. Frequency measurement is made reference to ^{87}Rb $F=2$ to $F' = 1$ transition.

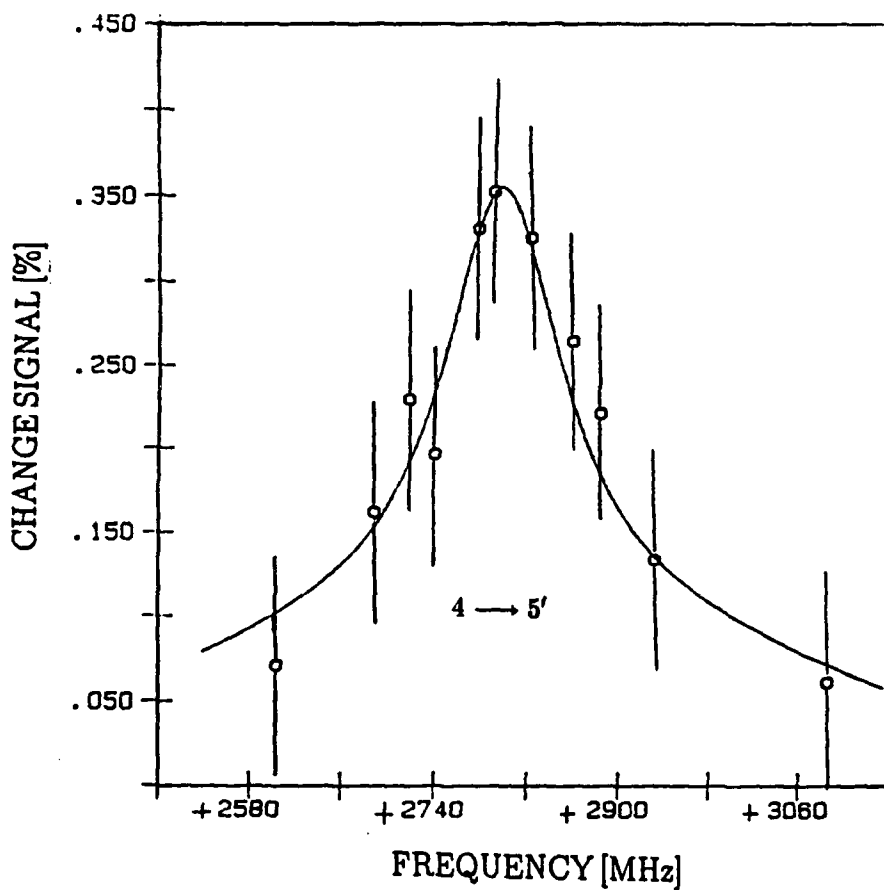


Figure 5-6: Observed gamma ray change signal for ^{85m}Rb D1 $F = 4$ to $F' = 5$ ^{85m}Rb transition. Transition pumped with 300 mW total power, at cell pressure of 300 mTorr. Frequency measurement is made with reference to ^{87}Rb $F=1$ to $F'=2$ transition

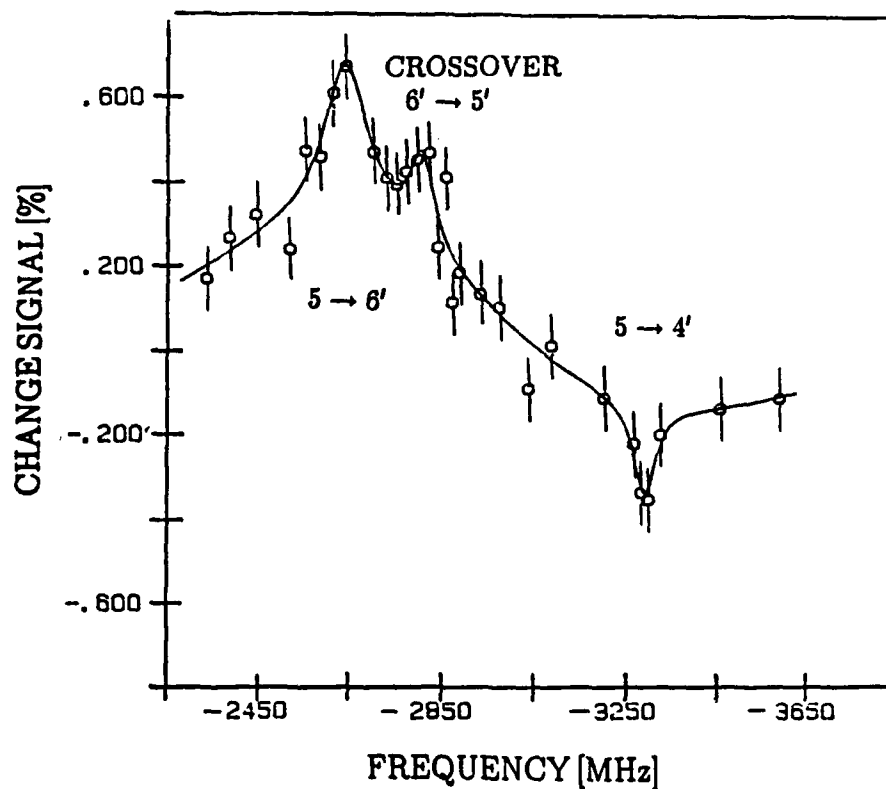


Figure 5-7: Observed gamma ray change signal for ^{85m}Rb low energy D2 transitions. Transition pumped with 550 mW total power, at cell pressure of 300 mTorr. From higher to lower frequency, the $F=5$ to $F'=6$ transition, the 6 to 5 crossover, and the $F=5$ to $F'=4$ transition. Frequency measurements made with reference to ^{87}Rb $F=2$ to $F'=1$ transition.

RELATIVE FREQUENCY LOCATIONS

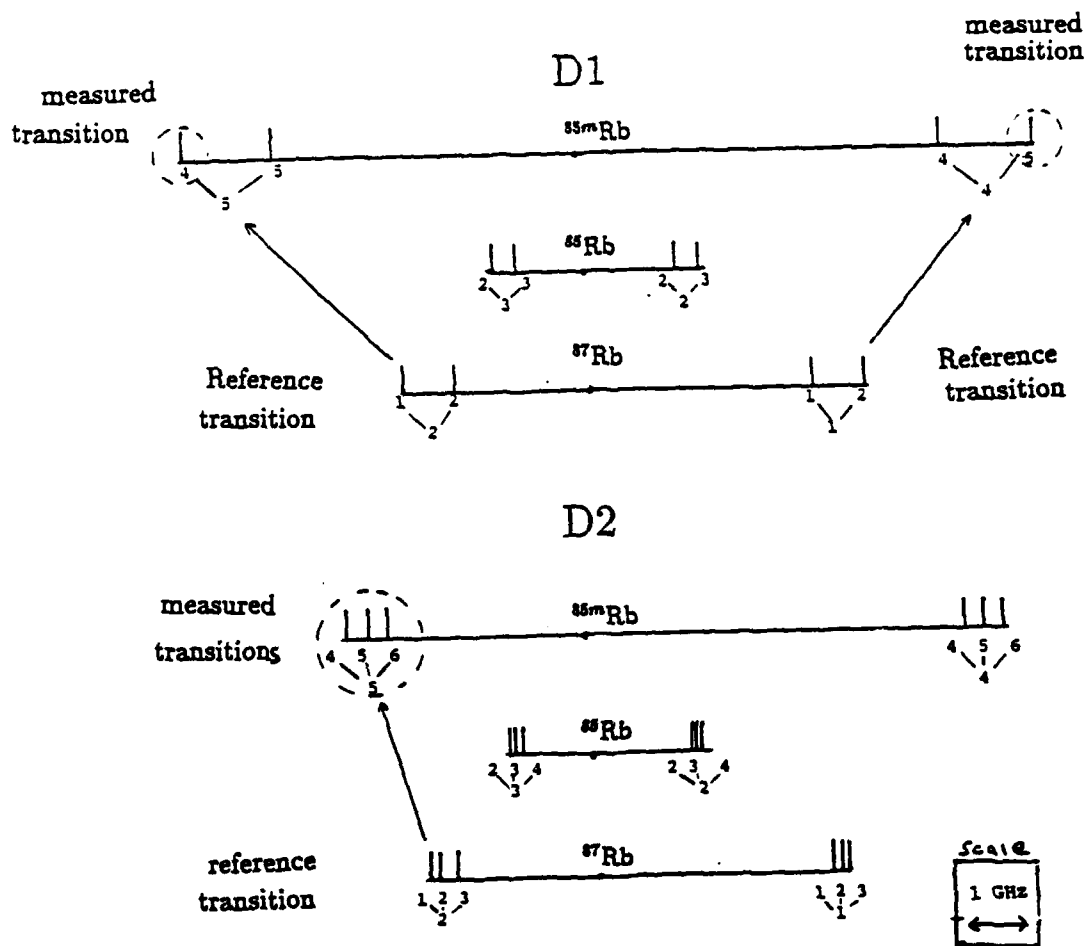


Figure 5-8: Relative frequency location of all measured transitions of ^{85}mRb .

became our uncertainty (± 6 MHz).

We also refit the data by using a $k_u = 360$ MHz, the thermal width, to see how sensitive the peak location was to this parameter. It is actually very insensitive, as it usually shifts the location less than 3 MHz. This is in contrast to fitting Doppler-broadened peaks, where the k_u parameter has a pronounced effect. In truth, one can probably eyeball the location of the transition to within ± 6 MHz using the raw data. This indeed is one of the nice features of a sub-Doppler signal. (The bad feature is that you have to count so long.)

5.4 Analysis of The Results

In this section we use the observed frequency measurements to calculate values for the nuclear parameters of interest, the A term and the magnetic dipole moment, the B term and the electric quadrupole moment, and the isomer shift.

5.4.1 Determining the A terms, and the Magnetic Dipole Moment

The total ground state and excited state splitting of the ^{87}Rb D1 is $(7647 \pm 3)\text{MHz}$, calculated using the known hyperfine coefficients provided in Arimondo [18]. From the hyperfine energy diagram (Fig. 2.2), the ground state and excited state splitting can be written $5A_{P1/2} + 5A_{S1/2}$, so that combined with the results in Tab. 5.2, the total D1 ^{85m}Rb splitting can be written

$$\Delta^{total} = 5A_{S1/2} + 5A_{P1/2} = (14049 \pm 9)\text{MHz}. \quad (5.1)$$

We can use this total splitting to determine the individual A terms and the magnetic dipole moment.

A standard technique for extracting the magnetic dipole moment from a hyperfine

measurement of A is to due it ratiometrically to some known isotope, or in our case, the known ground state of the isomer. For example

$$\frac{A_{85m}}{A_{85}} = \frac{(\mu_{85m} B_J) / I_{85m} J}{(\mu_{85} B_J) / I_{85} J}. \quad (5.2)$$

If one assumes that the electronic factors are the same for the isomer and the ground state, then they cancel, and assuming no hyperfine anomaly (see below), the equation can be re-written to solve for the unknown magnetic dipole moment in terms of known quantities,

$$\mu_{85m} = \frac{A_{85m}}{A_{85}} \frac{I_{85m}}{I_{85}} \mu_{85}. \quad (5.3)$$

(In the same way, the unknown quadrupole moment can be found

$$Q_{85m} = \frac{B_{85m}}{B_{85}} Q_{85}. \quad (5.4)$$

However, we use a different method in this thesis, as described later in this section.)

Adding the contributions from $A_{P1/2}$ and $A_{P3/2}$ we can write

$$\mu_{85mRb} = \frac{A_{85mRb}^{Total}}{A_{85Rb}^{Total}} \frac{I_{85mRb}}{I_{85Rb}} \mu_{85Rb}. \quad (5.5)$$

Substituting the known value of $\mu = 1.3533505 \mu_N$ [24], with $I_{85} = 5/2$ and $I_{85m} = 9/2$, yields a value

$$\mu_{85m} = (6.043 \pm .005) \mu_N. \quad (5.6)$$

It can also be seen that the A ratios between isomer and isotope are equal, i.e.

$$\frac{A_{S1/2}^{85mRb}}{A_{Total}^{85mRb}} = \frac{A_{S1/2}^{85Rb}}{A_{Total}^{85Rb}} \quad (5.7)$$

and likewise with $A_{P1/2}$ and $A_{P3/2}$. Therefore, we can write

$$A_{S1/2} = (2510 \pm 2) \text{MHz}, \quad (5.8)$$

$$A_{P1/2} = (299.5 \pm 0.7)\text{MHz} \quad (5.9)$$

and

$$A_{P3/2} = (62.04 \pm 0.07)\text{MHz}. \quad (5.10)$$

The Hyperfine Anomaly

The hyperfine anomaly, or Bohr-Weisskopf effect, arises from the fact that the magnetic dipole moment associated with the nucleus is not a point dipole, but is distributed throughout the nucleus. We can account for this effect by adding a correction term, ϵ , to our A value derived above

$$A = -g_I \mu_N H_0 \hbar^2 (1 + \epsilon) \quad (5.11)$$

so that the ratio of two A terms is

$$\frac{A_1}{A_2} = \frac{g_1(1 + \epsilon_1)}{g_2(1 + \epsilon_2)} \cong \frac{g_1}{g_2} (1 + \epsilon_1 - \epsilon_2) \quad (5.12)$$

or defining

$${}_1\Delta_2 = \epsilon_1 - \epsilon_2 \quad (5.13)$$

we can rewrite the differential hyperfine anomaly as

$${}_1\Delta_2 = \frac{A_1 g_2}{A_2 g_1} - 1. \quad (5.14)$$

For example, in rubidium, the anomaly between ^{85}Rb and ^{87}Rb has been measured by Penselin et al. [11] as ${}_{85}\Delta_{87} = 0.0035135(17)$. However, in our work, we are unable to measure both the nuclear g factor and the hyperfine A value independently. In addition, our uncertainties are probably not small enough to measure any anomaly. This is exactly the situation that occurred with Thibault's study of rubidium isotopes, where she found no evidence of any anomalies [19].

5.4.2 Extraction of Electric Quadrupole Moment

The electric quadrupole value can be derived in a similar fashion, once the hyperfine B value is determined. From the splitting between the D2 $F'=6$ level and the F' ($6 \rightarrow 5$) crossover, we can write

$$\Delta_{6 \rightarrow c.o.} = 3A_{P3/2} + .3334B \quad (5.15)$$

or solving for B

$$B = 3(\Delta_{6 \rightarrow c.o.} - 3A_{P3/2}). \quad (5.16)$$

Using the value for $\Delta_{6 \rightarrow c.o.}$ of (165 ± 8.5) MHz, and the value for $A_{P3/2}$ from above, yields $B = (-63.36 \pm 25)$ MHz. From the the $F' = 6$ and $F' = 4$ splitting, we can write

$$\Delta_{6 \rightarrow 4} = 11A_{P3/2} + .45833B \quad (5.17)$$

and again solving for B

$$B = \frac{\Delta_{6 \rightarrow 4} - 11A_{P3/2}}{.45833}. \quad (5.18)$$

Using the value for $\Delta_{6 \rightarrow 4}$ of (650 ± 8.5) MHz, and again the value for $A_{P3/2}$ from above, yields $B = (-70.8 \pm 18.6)$ MHz. A weighted average of the two values gives us a value of

$$B = (-68.2 \pm 15) \text{ MHz}. \quad (5.19)$$

Thibault [19] uses a conversion factor based on the Hartree-Slater calculations that show the best agreement with experiment. That conversion factor is

$$Q_s = 1.064 \times 10^{-2} B \quad (5.20)$$

with Q_s in barns and B in MHz. This yields a value for the quadrupole moment of

$$Q_s = (-.73 \pm .17) \text{ b}. \quad (5.21)$$

5.4.3 Extraction of Isomer Shift Value

To solve for the isomer shift value we write each transition in equation form. For example, the D1 $F=5$ to $F'=4$ transition can be written as

$$\Delta_{54} + 2.25A_{S1/2} + 2.75A_{P1/2} = {}^{85mRb}LC \quad (5.22)$$

where the ${}^{85mRb}LC$ represents the calculated transition frequency in the absence of hyperfine structure. The quantity Δ_{54} represents the energy of the transition (in MHz) and can be written with reference to the ${}^{85Rb}LC$ in the following way,

$$\Delta_{54} = \Delta_{54}^{85RbLC} + {}^{85Rb}LC. \quad (5.23)$$

Substituting this quantity into the above equation, and using the fact that

$$\text{Isomer Shift} \equiv \delta\nu = {}^{85mRb}LC - {}^{85Rb}LC \quad (5.24)$$

allows us to rewrite the expression as

$$\Delta_{54}^{85RbLC} + 2.25A_{S1/2} + 2.75A_{P1/2} = {}^{85mRb}LC - {}^{85Rb}LC = \delta\nu_{D1}. \quad (5.25)$$

In a similar fashion we can write the other D1 transitions as

$$\Delta_{45}^{85RbLC} - 2.75A_{S1/2} - 2.25A_{P1/2} = \delta\nu_{D1}. \quad (5.26)$$

Substituting the values from Tab. 5.2 , and the A values from above, yields

$$\delta\nu_{D1} = (120.6 \pm 5.7)\text{MHz}.$$

This value must be corrected for the D1 collision effect [6], which is (-1.6)MHz, yielding a value of

$$\delta\nu = (-119 \pm 6)\text{MHz}.$$

The D2 transitions can be written in a similar fashion, i.e.

$$\Delta_{56}^{85\text{Rb}LC} + 2.25A_{S1/2} - 6.75A_{P1/2} - .25B = \delta\nu_{D2} \quad (5.27)$$

$$\Delta_{54}^{85\text{Rb}LC} + 2.25A_{S1/2} + 4.25A_{P3/2} + .20833B = \delta\nu_{D2} \quad (5.28)$$

and

$$\Delta_{5co}^{85\text{Rb}LC} + 2.25A_{S1/2} - 3.75A_{P3/2} + .08334B = \delta\nu_{D2}. \quad (5.29)$$

Using the values of A and B from above, and the values from Tab. 5.2, we arrive at a value of

$$\Delta\nu_{D2} = (-108.4 \pm 6)\text{MHz}.$$

Correcting for the D2 collision effect (-1.75)MHz, leaves

$$\Delta\nu = (-106.7 \pm 6)\text{MHz}.$$

Averaging the two values for $\Delta\nu$ yields a value of

$$\Delta\nu = (-113 \pm 5)\text{MHz}. \quad (5.30)$$

Chapter 6

Discussion Of Nuclear Parameters

To discuss the results of the experiment, the nuclear shell model is introduced. The model is used to calculate the single particle magnetic dipole moment and electric quadrupole moment values, and these are compared to the actual values observed. Additionally, the values for other rubidium isotopes are examined. The observed quadrupole moment is used to calculate a deformation parameter. The observed isomer shift value is first converted to a change in the mean square radius, and then converted to a change in deformation. The two deformation parameters are then compared. Again this is done for the other isotopes also. The ^{85m}Rb values are then compared directly to the ^{81m}Rb values, a similar 9/2 single particle state.

6.1 The Nuclear Shell Model

The model used in this work for the interpretation of the results is the nuclear shell model, which combines the extreme single particle model of the nucleus with the collective effects of the nuclear core. A very brief summary of the history behind this model is provided in this section.

6.1.1 Brief Development of the Shell Model

The shell model arose from an effort to explain the observed characteristics of the nucleus. The evolution of the model is described below.

The liquid drop model, as the name implies, came about due to the similarities of the nucleus to a classical liquid drop. Classical liquid drops of incompressible fluid have two properties that stand out; (1) the interior densities are the same, and (2) their heat of vaporization are proportional to their masses. The heat of vaporization is the energy necessary to divide the drop into its constituent molecules. In a similar fashion, nuclei have two properties (1) their interior mass densities are approximately the same and (2) their total binding energies are approximately equal to their masses, i.e. $\Delta E/A \simeq \text{constant}$. Here ΔE is the energy necessary to remove the last nucleon, and A is the number of nucleons. The nucleus is modeled as a sphere with uniform interior density having a well defined surface. The radius is proportional $A^{1/3}$, the surface area proportional to $A^{2/3}$, and the volume proportional to A .

The liquid drop model gives a good description of the average behavior of nuclei in terms of binding energy. However it does not explain the particular stability of certain nuclei when the number of protons, neutrons or both equals a "magic" number;

$$Z \text{ and/or } N = \text{i.e. } 2, 8, 20, 28, 50, 82, 126.$$

This situation is similar to the shell closure known to occur in the electronic configuration of the atom. This led scientist to develop a shell model for the nucleus. However a key sticking point in the analogy with the atomic case arose. In the atomic case it is assumed that the electrons move independently in an atomic potential. In the nucleus, due to the high density, it was hard to believe that nucleons could move without constantly being scattered, and producing a type of Brownian motion [1, page 576].

The answer was provided by Weisskopf through the Fermi gas model[1]. This model, which is similar to the free electron gas model for conduction electrons in a solid, assumes that each nucleon moves in a net potential produced by all the other nucleons in the

nucleus. This net potential has a constant depth inside the nucleus, due to the uniform density of nucleons there, and outside the nucleus the potential falls off consistent with the range of nuclear forces. The potential can then be approximated as a three-dimensional finite square well. Each individual nucleon occupies a particular energy level consistent with the exclusion principle which forbids identical particles from occupying the exact same state. The only collisions that can occur are between two nucleons of the same type exchanging quantum states, producing no measurable effect [1, page 578].

6.1.2 The Extreme Single Particle Model

The next logical step in the evolution of the model was to solve the Schrodinger equation for the potential which best described the empirical evidence. Although many central potential forms were tried, none were found that properly produced the shell closure effect at the magic numbers. In 1949, Mayer (and independently Jensen), introduced the concept of spin-orbit coupling[1]. They proposed that each nucleon, in addition to a central potential, feels a strong spin-orbit coupling. This coupling is much stronger than that felt in the atomic case, and is not magnetic in origin, but is due to the strong nuclear force. This model correctly produced shell closure at the magic numbers. It also predicts the total angular momentum and parities of the ground states of almost all the nuclei. A diagram of these states is shown in Fig. 6.1. Although successful in some predictions, the shell model is not quite as good in predicting such quantities as the magnetic dipole moment or the quadrupole moment. The model predicts that the entire magnetic moment of an odd-A nucleus should be due entirely to the last unpaired nucleon, since the magnetic dipole moments of the other nucleons should cancel out in pairs just as the angular momenta does. This however is not correct. The magnetic moment is not due entirely to the last unpaired nucleon, but also has a contribution from the other nucleons. The total angular momenta and magnetic dipole moment are not always paired off such that they cancel. The assumption only works for the total angular momentum since it is quantized. Therefore if the pair at any one time has

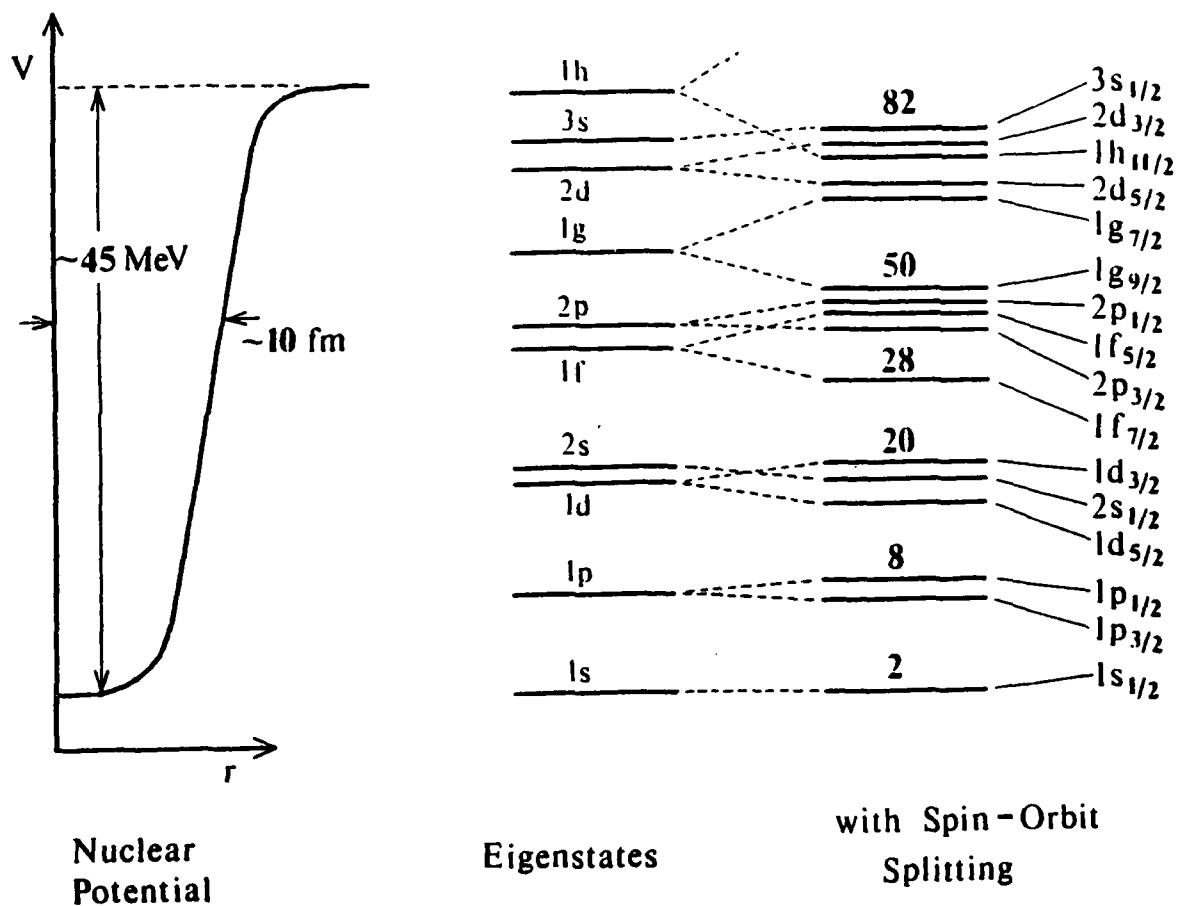


Figure 6-1: Single Particles States with Spin Orbit Splitting.

non-zero angular momentum, the odd nucleon must have exactly the right amount to compensate and keep the total angular momentum of the nucleus constant. The total magnetic dipole moment is not quantized, so this compensation effect does not apply. Although the predictions of the shell model are not accurate, they do provide a limit on the values of the magnetic dipole moment. However, the quantitative predictions of the electric quadrupole moment made using this model are usually very inaccurate, showing the major weakness of this model.

6.1.3 The Shell Model and ^{85m}Rb

As described in chapter 1, ^{85}Kr decays into an excited state of ^{85}Rb , at 514 Kev above ground. The nucleus has 48 neutrons, two neutrons short of shell closure. This excited state, designated as an isomer, is written ^{85m}Rb , and has a half-life of $1 - \mu\text{s}$. The spin of the excited nucleon is $9/2^+$, placing it in the $g_{9/2}$ single particle state, as shown in figure 6.2 (along with other possible configurations for rubidium).

6.1.4 The Shell Model: Single Particle Plus Core Collective Motion

A combination of the single particle model and the liquid drop model is known as the collective model. It incorporates aspects of both models to best fit empirical data. The model assumes that nucleons in unfilled subshells of a nucleus move independently in a net nuclear potential formed by the core of filled subshells, just as the single particle model does. However, the net potential due to the core is not spherically symmetrical as in the shell model, but is a potential that undergoes shape deformations. These deformations represent the collective motion of the nucleons in the core of the nucleus. Just as in the shell model, nucleons fill energy levels associated with the potential, split by the same-spin orbit coupling. A way to view this model is to consider the unpaired nucleon with a relatively large angular momentum moving in a orbit with a large radius,

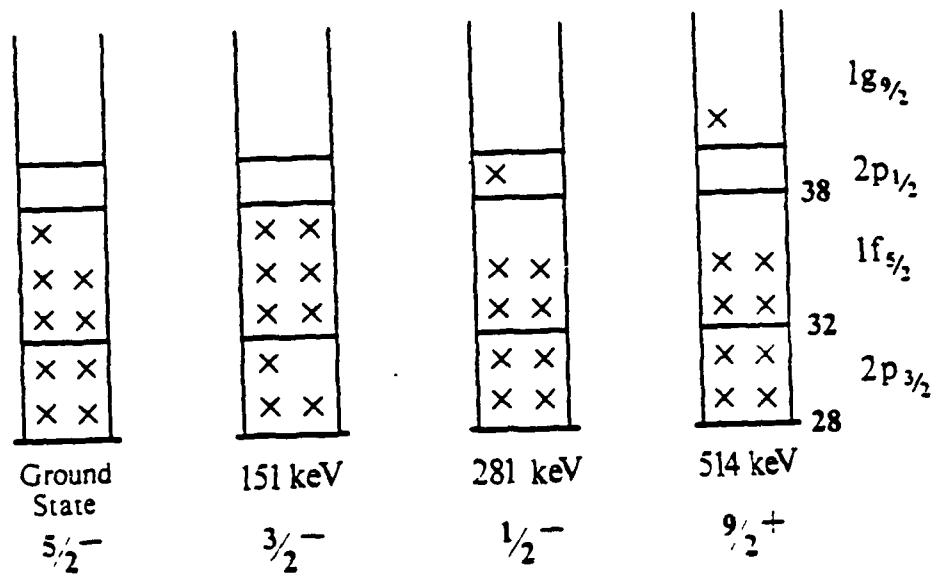


Figure 6-2: Ground state and low-lying excited states of ^{85}Rb .

near the core of the nucleus of filled sub-shells. Due to the nuclear force, the unpaired nucleon distorts the core. This distortion follows the path of the nucleon, much like the moon produces tides on earth. This distortion in turn affects the motion of other unpaired nucleons. So in the collective model part of the angular momentum is carried by the "tidal waves"[1, page 592] of the nucleus, and part by the separate nucleon. This moving deformation is partly composed of protons, and therefore is a current producing a magnetic dipole moment. The total magnetic dipole moment is the sum of the core effect and the single nucleon effect. This model also is better at explaining the electric quadrupole effect, as the bulk of this moment can be attributed to the deformation of the core.

6.2 Comparison of Observed Results to Single Particle Predictions.

The single particle values for the ^{85m}Rb isomer are derived in the following section, and compared to the observed results.

6.2.1 The Source of the Nuclear Magnetic Dipole Moment: The Motion of the Nucleons

The magnetic dipole moment of the nucleus can be considered as arising from its constituent nucleons. If \vec{J} is the current density, then it can be considered as arising from a charge density ρ so that $\vec{J} = (\rho\vec{v})/c$. If the charge density is composed of constituent parts of charge e and mass m , the angular momentum *density* is $\vec{L} = (M\rho/e)(\vec{r} \times \vec{v})$ and so

$$\vec{M} = \frac{1}{2} \frac{e}{Mc} \int \vec{L} dV \quad (6.1)$$

or quantum mechanically for Z protons

$$M_{orbital} = \frac{1}{2} \frac{e\hbar}{Mc} \int \psi^* \sum_{i=1}^Z \vec{l}_i \psi dV \quad (6.2)$$

where \vec{l}_k is the orbital angular-momentum operator of the k th proton, ψ is the wave function of the nucleus. Since all the particles have the same ratio of charge to mass, the magnetic dipole is parallel to the total angular momentum operator with which it is associated [3]. The orbital magnetic dipole operator then is

$$\vec{M}_{orbital} = \mu_0 \sum_{\text{protons}} \vec{l}_k \quad (6.3)$$

where $\mu_0 = (e\hbar/2m_p c)$. Or, including all nucleons

$$\vec{M}_{orbital} = \mu_0 \sum_{k=1}^A g_k^{(l)} \vec{l}_k \quad (6.4)$$

and $g_{proton}^{(l)} = 1$ and $g_{neutron}^{(l)} = 0$. Likewise, the magnetic dipole moment associated with the spin angular momentum

$$\vec{M}_{spin} = \mu_0 \sum_{k=1}^A g_k^{(s)} \vec{s}_k \quad (6.5)$$

where $g_{proton} = 5.5856$ and $g_{neutron} = -3.8263$.

The magnetic-moment operator then of the nucleus can be written

$$\vec{M} = \mu_0 \sum_{k=1}^A (g_k^{(l)} \vec{l}_k + g_k^{(s)} \vec{s}_k). \quad (6.6)$$

The total angular momentum of the nuclear system can be written as the sum of the angular momentum of the constituent nucleons

$$\vec{I} = \sum_{k=1}^A (\vec{l}_k + \vec{s}_k) \quad (6.7)$$

or

$$\vec{I} = \vec{L} + \vec{S}. \quad (6.8)$$

The magnetic moment is defined as the expectation value of M_Z in the state where $I_Z = I$ representing the maximum projection along a spatial axis

$$\mu = gI = \frac{1}{\mu_0} \int \Psi_{I,I}^* M_Z \Psi_{I,I} dV \quad (6.9)$$

In the extreme single particle model, the angular momentum and magnetic moments cancel in pairs, leaving only the contribution from the last nucleon, and $I = i$. In that situation, there are two cases depending on whether $i = l + \frac{1}{2}$ or $i = l - \frac{1}{2}$. For $i = l + \frac{1}{2}$

$$\mu = lg_l + \frac{g_s}{2}. \quad (6.10)$$

For the case where $i = l - \frac{1}{2}$

$$\mu = \frac{i[(i + \frac{3}{2})g_l - \frac{g_s}{2}]}{(i + 1)}. \quad (6.11)$$

The values arrived at using these formulae produce the Schmidt lines, which seem to be rough limits on the actual values obtained by measurement.

In the collective model approach the actual magnetic moment has two components, that due to the single particle and that due to collective effects. A rough measure of how well a particular nucleus can be described in the single particle model is obtained by looking at the ratio of its actual value to its single particle value. This is done in Tab 6.1 for the various $n/2$ isotopes of rubidium measured by Thibault [19], and our value of ^{85m}Rb .

From the table it is clear that the single particle model is a good predictor for the two isomers measured. That is because the excitation of the single particle to the higher angular momentum state, or classically larger orbit, diminishes pulling effect on the core of nucleons, and the magnetic moment approaches that of a single particle.

^ARb	Spin	$\mu_{sp}[\mu_N]$	$\mu_{obs}[\mu_N]$	$\frac{\mu_{obs}}{\mu_{sp}}$
77	3/2	3.8	0.657	0.17
79	5/2	.86	3.36	3.9
81m	9/2	6.8	5.6	.82
81	3/2	3.8	2.06	.54
83	5/2	.86	1.42	1.65
85	5/2	.86	1.36	1.58
85m	9/2	6.8	6.04	.89
87	3/2	3.79	2.75	.73
89	3/2	3.79	2.38	.63
91	3/2	3.79	2.18	.58
93	5/2	.86	1.41	1.64
95	5/2	.86	1.33	1.55
97	3/2	3.79	1.84	.49

Table 6.1: Comparison of single particle magnetic dipole moment values to actual observed values for several $n/2$ isotopes of Rb.

6.2.2 The Single Particle Quadrupole Moment

The electric quadrupole moment is defined as

$$Q_{kj} = \frac{Q}{I(2I-1)} \left[\frac{3}{2} (I_k I_j + I_j I_k) - \delta_{kj} \tilde{I}^2 \right] \quad (6.12)$$

where $I_k (k = 1, 2, 3)$ are the components of \tilde{I} and

$$Q = \left(\frac{16\pi}{5} \right)^{1/2} \langle Q_2 \rangle_{M=I} = \left(\frac{16\pi}{5} \right)^{1/2} \int \Psi_{I,I}^* Q_2 \Psi_{I,I} dV. \quad (6.13)$$

The value

$$Q_2 = e \sqrt{\frac{5}{16\pi}} \sum (3z_k^2 - r_k^2) = \sqrt{\frac{5}{16\pi}} Q_{33} \quad (6.14)$$

so that Q is the expectation value of Q_{33} in which the z component of \tilde{I} has its maximum value I . Q is called the electric quadrupole moment, and is the quantity usually quoted experimentally [3, page 69]. In the shell model the quadrupole moment for a single proton is

$$Q_{\text{single particle}} = -e \frac{2I-1}{2(I+1)} \langle r^2 \rangle, \quad (6.15)$$

where

$$\langle r^2 \rangle = \frac{1}{Ze} \int \rho(r) r^2 dV. \quad (6.16)$$

is the mean-square of the distance from the center of the nucleus. For a spherical nucleus, the radius is given from the liquid drop model as

$$r_0 = R_0 A^{1/3} \quad (6.17)$$

where R_0 is equal to 1.2 fm [19]. Then, the mean square radius becomes

$$\langle r^2 \rangle_{\text{sph}} = \frac{3}{5} (R_0 A^{1/3})^2 \quad (6.18)$$

which is used in evaluating the single particle quadrupole moment.

The single particle prediction can be compared to the actual measured values as was done with the magnetic dipole values. Again the values are taken from Thibault [19]. This is done in Tab. 6.2. It is interesting that there are two distinctive behaviors displayed here. Most of the quadrupole values are only about a factor of two different from the single particle value, showing that the single particle model is a good approximation for these nuclei. However the isotopes 81, 81m, 85m, 77, and 97 show definite deviations from single particle behavior. Again, though, note that 81m and 85m have very similar values.

6.2.3 The Quadrupole Moment of a Deformed Nucleus

The collective model explains these deviations by allowing for deformation in the central core. Here a deformation parameter is introduced in the the nuclear radius $r(\theta)$ in a direction at angle θ to the symmetry axis. Then

$$r(\theta) = r_0(1 + \beta Y_{20}(\cos\theta) + \dots) \quad (6.19)$$

or, stopping at Y_{20}

$$r(\theta) = r_0[1 + \beta(\frac{5}{4\pi})^{1/2}(\frac{3}{2}\cos^2\theta - \frac{1}{2})]. \quad (6.20)$$

For ellipsoidal nuclei, the deformation parameter is related to the difference between the semiaxes, Δr , such that

$$\frac{a-b}{(a+b)/2} = \frac{\Delta r}{r} = \frac{3}{2}(\frac{5}{4\pi})^{1/2}\beta = \delta. \quad (6.21)$$

The actual quadrupole moment can be found in two steps[2]. The quadrupole moment with respect to the symmetry axis (z) is

$$Q' = \sqrt{\frac{16\pi}{5}} \int \langle Q'_2 \rangle \cong \frac{3}{\sqrt{5\pi}} Z r_0^2 \beta (1 + 0.36\beta) \quad (6.22)$$

^ARb	Spin	$Q_{sp}[b]$	$Q_{obs}[b]$	$\frac{Q_{obs}}{Q_{sp}}$
77	3/2	.0623	0.695	11.2
79	5/2	.091	-.098	1.1
81m	9/2	-.118	-.743	6.3
81	3/2	.065	.398	6.1
83	5/2	.094	.196	2.1
85	5/2	.096	.228	2.4
85m	9/2	-.122	-.73	6.0
87	3/2	.068	.130	1.9
89	3/2	.069	.144	2.1
91	3/2	.070	.154	2.2
93	5/2	.101	.177	1.8
95	5/2	.103	.211	2.05
97	3/2	.073	.581	8.0

Table 6.2: Comparison of single particle quadrupole values with actual observed values.

This quadrupole moment must then be projected onto some spatial axis. This is done using the wave functions of a rotating ellipsoid[2], producing

$$Q = Q' \frac{I(2I - 1)}{(I + 1)(2I + 3)}. \quad (6.23)$$

Then using the experimental quadrupole moment yields a value for the deformation parameter. These deformation values will be compared with the deformation values derived from the isotope shift in the following section.

6.3 Deformation Parameter

As seen above, the nucleus in some cases is best described as deformed. This deformation manifest itself in a change of the mean square radius attributed to two factors, a change in volume and a change in shape. Isolating the change in shape allows again for the measurement of another deformation parameter, β_{IS} . Since the β_Q is derived using the wavefunction for a rotating ellipsoid, it is a measure of the permanent deformation of the nucleus. The β_{IS} quantity however can include vibrations, which do not change the mean nuclear charge radius but do change the mean square radius. Therefore, a comparison of the two deformation parameters can yield information about the nucleus. If they are exactly the same, the assumption can be made that the nucleus is permanently deformed, and well represented as a rotor. If they do not agree, then this assumption is not valid, and the nucleus may be undergoing vibrational motion or even a composite vibrational and rotational motion. This section describes how the β_{IS} parameter is extracted from the change in mean square radius. Since Thibault has analyzed many rubidium isotopes in this manner, Her methodology of analysis is presented in this section, where we then apply it to the isomer ^{85m}Rb . In the discussion section, we will compare the two deformation parameters for the isomer.

6.3.1 The Methodology For Separating the Mean Square Radius into a Volume Change and a Deformation Change.

For deformed nuclei the radius is given by equ. (6.20), and so using equ. (6.16) the mean square radius at constant volume is given

$$\langle r^2 \rangle_\beta = (1 + \frac{5}{4\pi} \langle \beta^2 \rangle) \langle r^2 \rangle_{sph}. \quad (6.24)$$

Then the total change in mean square radius can be written as the sum of the volume change and the shape change

$$\delta \langle r^2 \rangle = \delta \langle r^2 \rangle_{sph} + \delta \langle r^2 \rangle_\beta \quad (6.25)$$

where

$$\delta \langle r^2 \rangle_\beta = \frac{5}{4\pi} \delta(\langle \beta^2 \rangle \langle r^2 \rangle) \quad (6.26)$$

is the change due solely to deformation.

In order to isolate this change due to deformation, we merely subtract the change due to volume change from the total change. However, when studying isotope chains, we must add an empirically determined term to account for the fact that volume changes more slowly if we add only neutrons. The change in volume then becomes

$$\delta_{sph} \langle r^2 \rangle = \eta \frac{2}{3} \frac{\delta A}{A} \langle r^2 \rangle_{sph} \quad (6.27)$$

where η is the empirical term. In rubidium, Thibault has found that η is not a single quantity, but depends on the number of neutrons in the isotope. The ^{87}Rb isotope, with a closed neutron shell at $N=50$, is the closest to spherical, so all measurements are made reference that isotope. Then $\eta = 0.25$ for $N < 50$ and $\eta = 0.8$ for $N > 50$ [19]. The change

due to deformation only is then

$$\delta\langle r^2 \rangle_\beta = \delta\langle r^2 \rangle - \eta \frac{2}{3} \frac{\delta A}{A} \langle r^2 \rangle_{sph} \quad (6.28)$$

To solve for the change in the deformation parameter, the change in mean square radius is re-written to isolate $\delta\langle\beta^2\rangle$,

$$\delta\langle\beta^2\rangle = \frac{4\pi}{5} \frac{\delta\langle r^2 \rangle_\beta}{\langle r^2 \rangle_{sph}}. \quad (6.29)$$

Then if the reference isotope deformation is known, the deformation can be written

$$\beta_{isomer} = [\beta_{groundstate}^2 + \delta\beta^2]^{1/2}. \quad (6.30)$$

6.3.2 Calculation of the Deformation Parameter

Using ^{87}Rb as the reference isotope, Thibault [19] observed for ^{85}Rb a $\delta\nu$ of $(-80.1 \pm 1.4)\text{MHz}$, composed of a calculated mass shift of -57.025 MHz and a field shift of $(-23.075 \pm 1.4)\text{MHz}$.

The change in mean square radius for ^{85}Rb due to deformation is

$$\delta\langle r^2 \rangle_\beta = 0.0355 - (0.25) \left(\frac{2}{5}\right) \left(\frac{-2}{87^{1/3}}\right) (1.2)^2 = .1005 \pm .0022 \text{ fm}^2. \quad (6.31)$$

This value is then used to compute the change in deformation

$$\delta\langle\beta^2\rangle = \frac{4\pi}{5} \frac{.1005}{16.70} = .0151. \quad (6.32)$$

Then, using the value of $\beta_{IS} = 0.14$ from Thibault [19]

$$\beta_{85\text{Rb}} = [(0.14)^2 + 0.015]^{1/2} = 0.186 \approx 0.19 \pm .01 \quad (6.33)$$

which is the value used by Shimkaveg. (The value for β used here is taken from Fig.

12 in an article by Thibault [20] with no uncertainty assigned to it. Furthermore, it is the best value for reproducing the quoted values for the other deformations given in her work. A reasonable guess for the uncertainty, then, would probably be ± 0.01 . It is also important to keep in mind when evaluating the results that the η value is a fitted value, and therefore has some undetermined uncertainty associated with it.)

For ^{85m}Rb the observed shift from ^{87}Rb is (-193.1 ± 5.2) , adding the shift from ^{87}Rb to ^{85}Rb and the shift from ^{85}Rb to ^{85m}Rb . Subtracting the mass shift leaves (-136.1 ± 5.2) . The field shift is then converted to a change in the mean square radius, $(0.209 \pm .008)\text{fm}^2$. The component due to volume change is the same computed above for ^{85}Rb (-0.0650 fm^2) , yielding a mean square radius change due to deformation of

$$\delta\langle r^2 \rangle_{85m\text{Rb}} = 0.2740 \pm .008\text{fm}^2. \quad (6.34)$$

This in turn can be converted to a change in deformation of

$$\delta\langle \beta^2 \rangle = 0.041 \pm .0013 \quad (6.35)$$

which in turn yields a deformation parameter of

$$\beta_{85m} = [(0.14)^2 + 0.041]^{1/2} = 0.25 \pm .02. \quad (6.36)$$

This value, and the other deformation values derived from measurements by Thibault are given in table 6.3. The three isotopes of 77, 81, and 97 all appear to have closely matched deformation values, suggesting they are permanently deform nuclei, and may act as rotors. Once again, 81m and 85m display similar behavior. They do not appear to be not pure rotors, but probably have some deformation and some vibrational behavior.

^ARb	$\delta\beta\langle r^2\rangle[\text{fm}^2]$	$\delta\beta^2$	β_{IS}	β_Q	$\frac{\beta_{IS}}{\beta_Q}$
77	.583	.094	.34	.45	.76
79	.469	.074	.31	.04	7.75
81m	.326	.051	.26	.18	1.44
81	.356	.056	.27	.26	1.04
83	.182	.028	.22	.07	3.14
85	.101	.015	.19	.08	2.38
85m	.265	.041	.25	.17	1.47
87	0	0	.14	.08	1.75
89	.094	.014	.18	.09	2.00
91	.130	.019	.20	.09	2.22
93	.161	.023	.21	.06	3.50
95	.196	.027	.22	.07	3.14
97	.621	.086	.35	.33	1.06

Table 6.3: Comparison of quadrupole and isomer shift deformation parameters for several isotopes of rubidium. All values from Thibault except that of ^{85m}Rb measured in this work.

^A Rb	Spin	$\mu_{sp}[\mu_N]$	$\mu_{obs}[\mu_N]$	$\frac{\mu_{obs}}{\mu_{sp}}$	$Q_{sp}[b]$	$Q_{obs}[b]$	$\frac{Q_{obs}}{Q_{sp}}$	β_{IS}	β_Q	$\frac{\beta_{IS}}{\beta_Q}$
81	3/2	3.8	2.06	.54	.065	.398	6.1	.27	.26	1.04
81m	9/2	6.8	5.6	.82	-.118	-.743	6.3	.26	.18	1.44
85	5/2	.86	1.36	1.58	.096	.228	2.4	.19	.08	2.38
85m	9/2	6.8	6.04	.89	-.122	-.73	6.0	.25	.17	1.47

Table 6.4: Comparison of ^{85m}Rb and ^{81m}Rb along with ground states.

6.4 Comparing the 9/2⁺ spin nuclei: ^{81m}Rb and ^{85m}Rb.

Because both ^{81m}Rb and ^{85m}Rb have a proton in the excited 9/2 state, it is worthwhile to compare the parameters of both to see if there are any differences between them attributable to the short ($1 - \mu s$) lifetime of the ^{85m}Rb compared to long (32 minutes) lifetime of ^{81m}Rb. This is done in table 6.4, along with the ground states of both isomers.

From the table, it is quite clear that the two isomers have very similar behavior. They both approach the single particle magnetic dipole moment value, both quadrupole moments show pronounced collective effects, and the isotope shift and quadrupole moment deformation parameters are close. Interesting enough, their behavior relative to their ground state is totally different. The ground state of ⁸⁵Rb is close to a single particle state in terms of collective motion, as the ratio of Q_{obs}/Q_{sp} is about two. The isomer clearly displays more collective behavior. The ⁸¹Rb and its isomer both demonstrate collective behavior.

However, in terms of deformation parameter, the situation is reversed. The ⁸⁵Rb isotope, and its isomer, are not pure rotors, but both probably have vibrational motion (the ground state has been shown to have such motion [19]). On the other hand, ⁸¹Rb

looks like a pure rotor, while the isomer clearly is not. The conclusion drawn here is that the $9/2$ orbital is dominant in determining behavior for these two cases, and that the lifetime difference does not play a major role.

Chapter 7

Concluding Remarks

In conclusion, we have extended the applicability of the LINO technique to the study of short-lived isomers by demonstrating that saturation spectroscopy can be used to produce a narrow resonance change signal in the gamma-ray emission of the $1 - \mu s$ isomer, ^{85m}Rb . The new technique has allowed for an order of magnitude increase in precision. We have also simplified the experiment by showing that it is possible to do optical pumping with only one laser, even with a system that has two ground state hyperfine levels relatively far apart (> 1 GHz).

We have used that technique to measure the quadrupole value of the isomer for the first time. We have also measured a more accurate and precise value for the isomer shift, and confirmed the earlier Doppler broadened measurement of the magnetic dipole moment. The deformation parameter of the isomer was computed using both the quadrupole moment of the isomer and the isomer shift. While the two values do not agree, they both are larger than the corresponding ground state values, showing that the isomer is clearly more deformed than the ground state.

The isomer displays behavior very similar to the longer lived ^{81m}Rb isomer, suggesting the dominance of the excited $9/2$ level in determining behavior. These two isomers have values of the magnetic dipole moment, electric quadrupole moment and deformation parameter which are within 10% of each other.

The development of this technique can be considered as an additional tool to used when necessary to resolve overlapped transitions. If a Doppler resolved signal is adequate to resolve transitions in a gas-cell system under study, it is best to use a one beam signal, since the sub-Doppler technique increases the time necessary to perform the experiment tremendously. Sometimes, however, the sub-Doppler technique is the only way to resolve overlapped lines.

Although there are other candidate system available for study [6], the overall goal has been primarily the development of a technique that allows one to study very short-lived nuclei. Through the efforts of my predecessors a technique was developed using a gas-cell system off-line. My colleagues and I have improved that technique, allowing for narrow resolution using a single laser. The goal of the LINO project here at MIT has been met. This experiment successfully terminates the LINO project in the George R. Harrison Laboratory (at least for the time being).

Bibliography

- [1] R. R.
Eisberg,
Quantum Physics of Atoms, Molecules, Solids, Nuclei and Particles , (Wiley,
New York, 1974)
- [2] Emilio Segrè Nuclei and Particles, (Benjamin, London, 1977)
- [3] M.A. Preston and R.K. Bhaduri, Structure of the Nucleus, (Addison, Reading, 1975)
- [4] W.H. King, Isotope Shifts in Atomic Spectra, (Plenum, New York, 1984)
- [5] Thibault et al., "Hyperfine Structure and Isotope Shift of the D₂ Line of ⁷⁶⁻⁹⁸Rb and
Some of their Isomers", Phys. Rev. C. 23, 2720 (1981)
- [6] G.M. Shimkaveg, "Laser-Induced Nuclear Orientation and Gamma Anisotropy in
^{85m}Rb", Ph.D. Thesis, Unpublished, M.I.T. (1985)
- [7] L. Armstrong, Jr., Theory of the Hyperfine Structure of Free Atoms, (Wiley, New
York, 1971)
- [8] M. Weissbluth Atoms and Molecules, (Academic Press, New York, 1978)
- [9] H. Haken and H.C. Wolf, Atomic and Quantum Physics, (Springer-Verlag, Berlin,
1987)
- [10] O. Redi and H.H. Stroke, "Nuclear Structure and Atomic Spectrum", in
Lasers in Nuclear Physics, edited C.E. Bemis and H.K. Carter, (Harwood, Chur,
1982)

- [11] S. Penselin et al., "Hyperfine Structure of the Electronic Ground States of Rb⁸⁵ and Rb⁸⁷", Phys. Rev. 127, 524 (1962).
- [12] J.T. Hutton and W.W. Quivers, Jr., "Laser Applications To Fundamental Weak Interaction Studies", Phys. Rev. C 40, 314 (1989).
- [13] M.S. Feld, Classroom notes from course 8.242 at M.I.T.
- [14] M.S. Feld and V.S. Letokhov, "Laser Spectroscopy", Scientific American, Vol.229, Dec. 1973
- [15] W.Demtröder, Laser Spectroscopy, (Springer-Verlag,Berlin, 1981)
- [16] W.W. Quivers, Jr., "Production of Highly Polarized Vapors Using Laser Optical Pumping With Velocity Changing Collision", Phys. Rev. A 34, 3822 (1986).
- [17] P.G. Pappas, M.M. Burns, D.D. Hinshelwood, M.S. Feld, and D.E. Murnick, "Saturation spectroscopy with laser optical pumping in atomic barium", Phys. Rev. A 21, 1955 (1980)
- [18] E. Arimondo, M. Inguscio, and P. Violino, "Experimental Determinations of the Hyperfine Structure in the Alkali Atoms", Rev. Mod. Phys. 49, No.1 (1977)
- [19] C. Thibault et al., "Hyperfine Structure and Isotope Shifts of the D2 line of ⁷⁶⁻⁹⁸Rb and some of their Isomers", Phys. Rev. C 23, 2720 (1981)
- [20] C. Thibault and F. Touchard, "High Resolution Laser Spectroscopy Of Radioactive Alkali Isotopes", published in Lasers In Nuclear Physics edited C.E. Bemis, Jr., and H.K. Carter (Hardwood, Chur, 1982)
- [21] M.Feld, "Lasers in Nuclear Physics", published in Lasers in Nuclear Physics edited C.E. Bemis, Jr., and H.K. Carter (Hardwood, Chur, 1982)

- [22] H.J. Kluge "Laser Spectroscopy of Radioactive Isotopes In Resonance Cells ", published in Lasers in Nuclear Physics edited C.E. Bemis, Jr., and H.K. Carter (Hardwood, Chur, 1982)
- [23] J.R. Beene, C.E. Bemis,Jr., S.D. Kramer, and J.P. Young "Laser-Optical Studies of the Spontaneous-Fission Isomer ^{240m}Am ", published in Laser in Nuclear Physics edited by C.E. Bemis, Jr., and H.K. Carter (Hardwood, Chur, 1982)
- [24] P. Raghavan, "Atomic Data and Nuclear Data Tables", 42, 221 (1989)
- [25] J.D. Jackson, Classical Electrodynamics (2nd Edition), (New York, Wiley, 1975)
- [26] M.M. Burns , PH.D. Thesis, MIT 1979 (unpublished)
- [27] L.D. Landau and E.M. Lifshitz Quantum Mechanics, (New York, Pergamon Press, 1977)
- [28] N. Allard and J. Kielkopf, " The Effects of Neutral Nonresonant Collisions on Atomic Spectral Lines ", Rev. Mod. Phys. 54, 1103 (1982).
- [29] P. Dabkiewicz, F. Buchinger, H. Fischer, H.J. Kluge, H. Kremmling, T. Kühl, A.C. Müller and H.A. Schuessler, Phys. Letters 82B, 199 (1979)
- [30] G. Nowicki et al., Phys. Rev. C 18, 2369 (1978)
- [31] K. Bekk et al., Z. Phys. A291, 219 (1979)
- [32] K.R. Anton et al., Phys. Rev. Letters 40, 642 (1978)

Appendix A

Matrix Elements of ^{85m}Rb

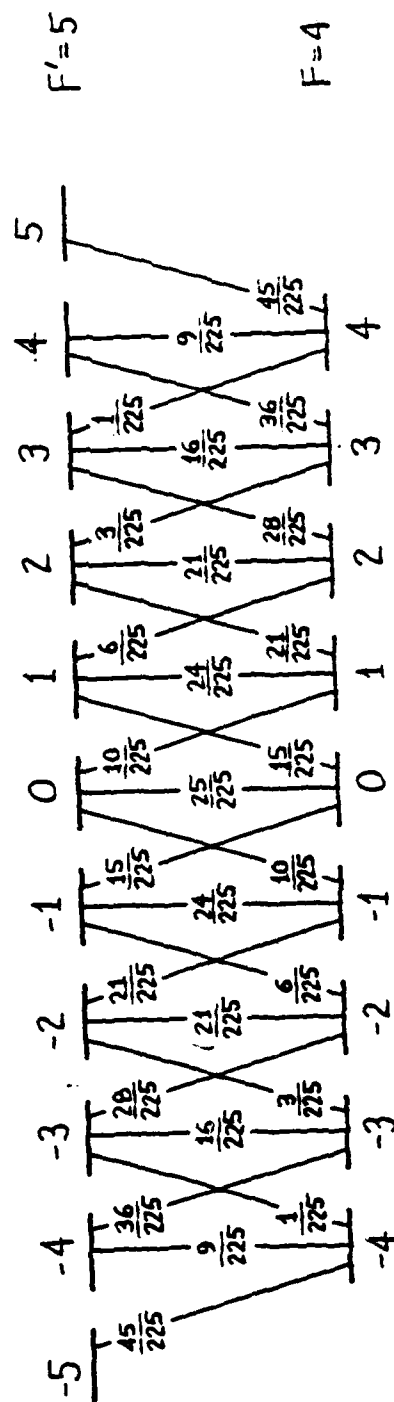
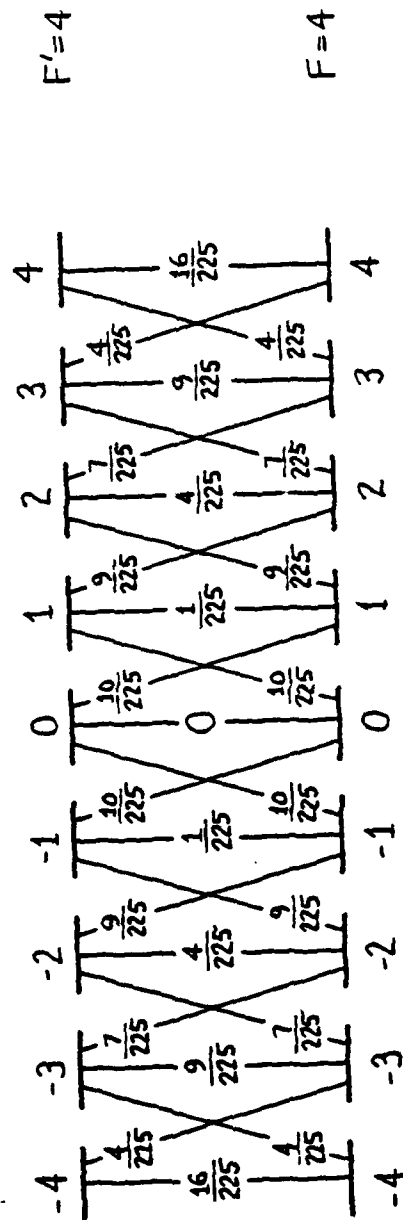
The cross section for absorption for rubidium can be written

$$\sigma_0 = \frac{8\pi k\tau}{\hbar} | \langle F', M_{F'} | \mu_q | F, M_F \rangle |^2 \quad (\text{A.1})$$

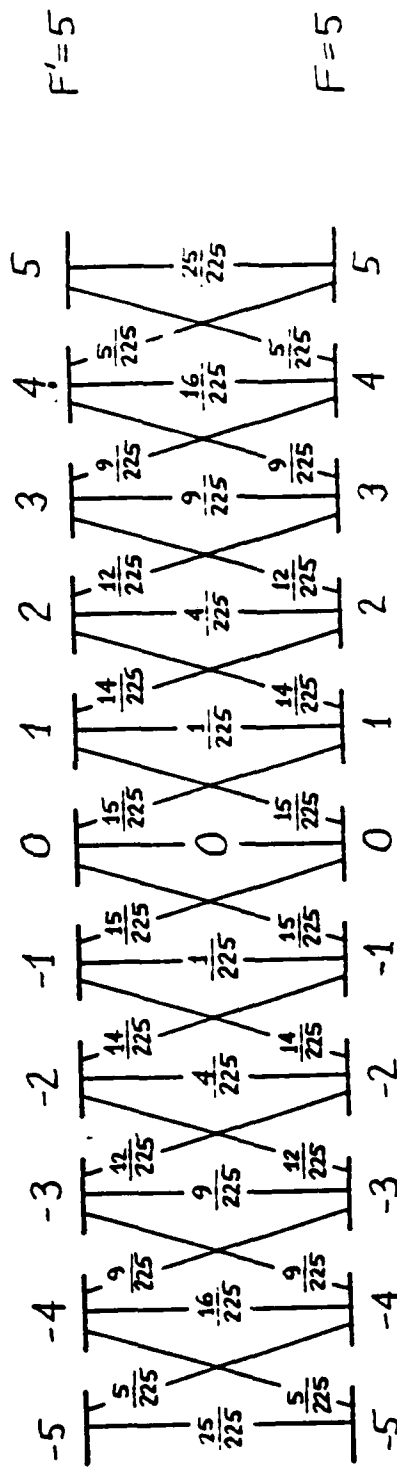
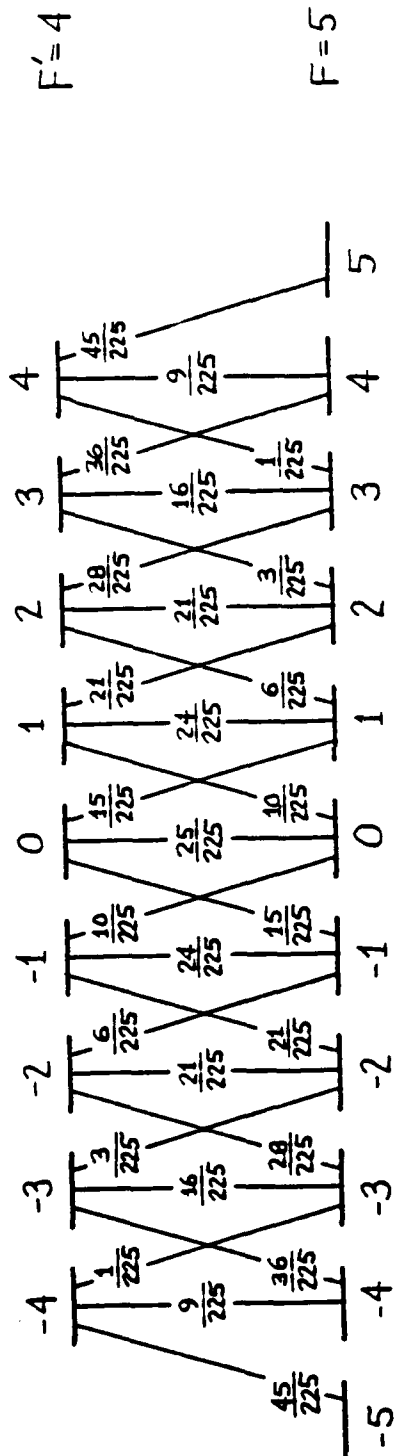
which can be reduced to [6][327-329]

$$\sigma(M_F \rightarrow M_{F'}) = U^2 \mathcal{F}^2 \mathcal{J}^2 \frac{9\lambda}{2\pi}. \quad (\text{A.2})$$

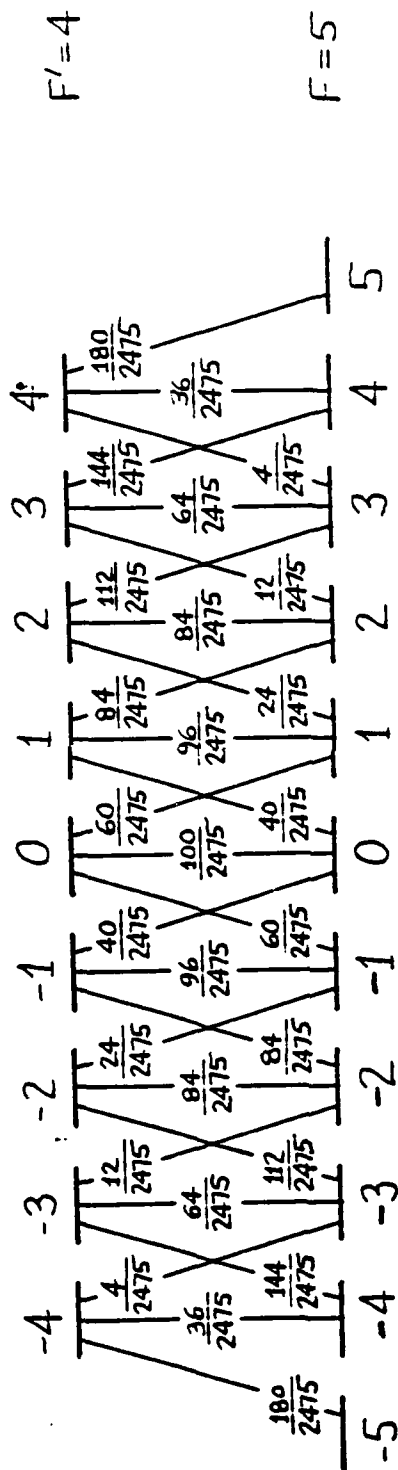
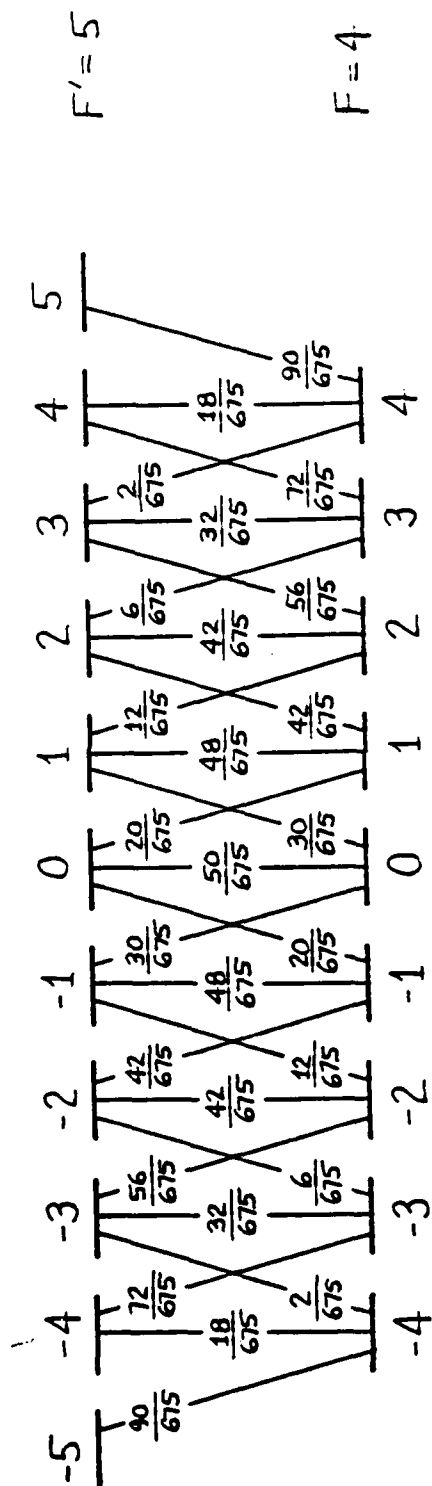
The $U^2 \mathcal{F}^2 \mathcal{J}^2$ term is called the reduced matrix elements, and are given for all ^{85m}Rb transitions on the following pages.



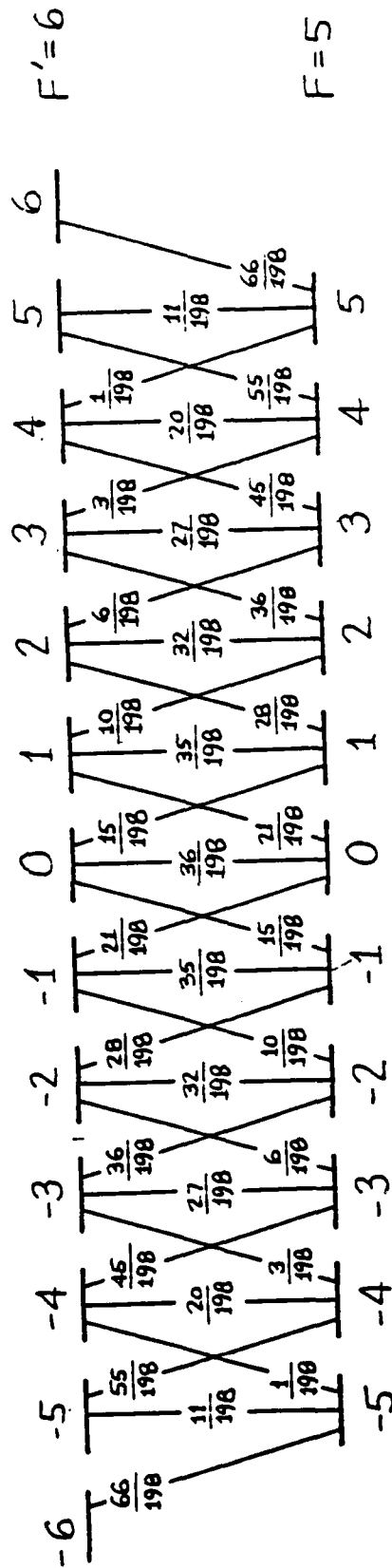
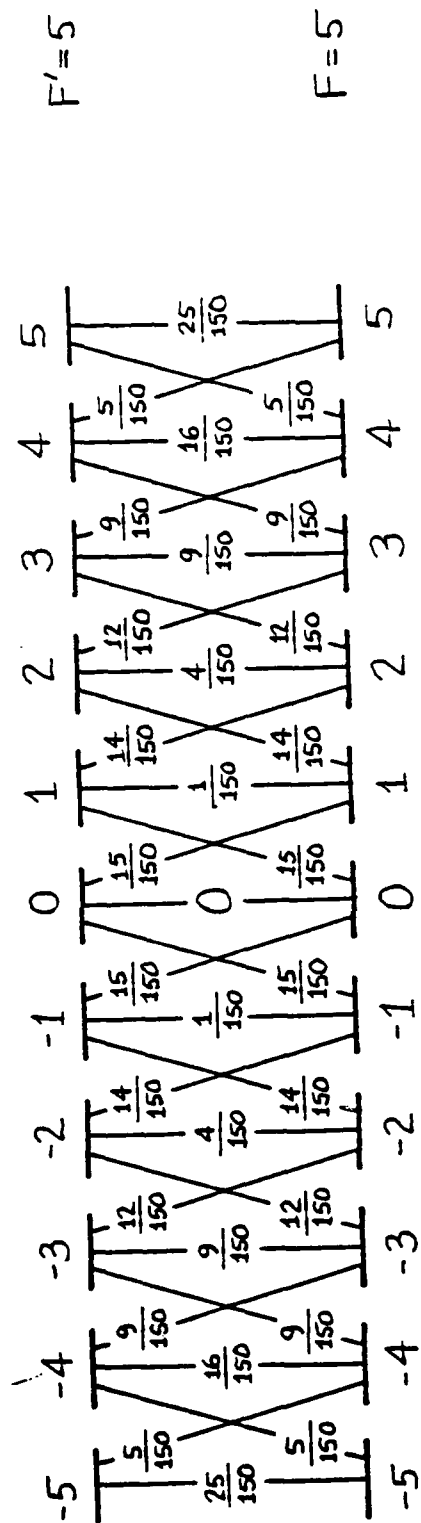
$05^m Rb D_1$



85^m Rb D₁



$85^m\text{Rb } D_2$



$85mRb \quad D_2$

Appendix B

Publication

The following publication was printed as a proceeding from the NICOLS 89 conference at Bretton Woods, and is copyrighted by Academic Press. It was published in Laser Spectroscopy IX, Academic Press (1989).

OBSERVATION OF SUB-DOPPLER LASER INDUCED NUCLEAR ORIENTATION OF ^{85}Rb

W.W. Quivers, Jr., J. Mackin, J.T. Hutton, M. Lercel ,
M. Otteson, G. Shimkaveg, R.R. Dasari, C.H. Holbrow,
M.S. Feld, and D.E. Murnick.

George R. Harrison Spectroscopy Laboratory
Massachusetts Institute of Technology
Cambridge, MA 02139

I. Introduction

We report the first observation of sub-Doppler resolved gamma anisotropy produced by Laser Induced Nuclear Orientation (LINO) [1]. As discussed below, the anisotropy was produced by laser optical pumping the D1 transition of the $1\mu\text{s}$ ^{85}Rb isomer.

Sub-Doppler LINO is uniquely suited for resolving closely spaced hyperfine structure (hfs) of very shortlived isomers, whose lifetimes are between 50 nanoseconds and 1 milli-second. In addition, sub-Doppler LINO allows more precise measurements of hf splittings to be made. For example, this leads to more accurate measurements of nuclear magnetic dipole and electric quadrupole moments, as well as isomer shifts.

LINO uses laser optical pumping to produce electronic alignment. This is transferred to the excited nucleus via the hyperfine interaction. When the oriented nuclei decay, anisotropy is observed in the spatial distribution of the emitted gamma rays. The hfs of the isomer is determined by monitoring the anisotropy as a function of laser detuning.

II. Laser Optical Pumping & Velocity Changing Collisions

Many applications of LINO require the use of a buffer gas. For example, on-line cell studies use buffer gas to slow down and confine the species of interest. Also, as is in our case, the buffer gas can be the parent of the species of interest.

The main effect of the buffer gas is to induce velocity changing collisions (vcc's) between the isomers and the buffer gas atoms. As Fig. 1a shows, vcc's knock atoms out of the resonant velocity bin and distributes them over the remainder of the Doppler distribution. Simultaneously vcc's are also knocking atoms into the resonant bin. The net effect produces increased Doppler coverage [2].

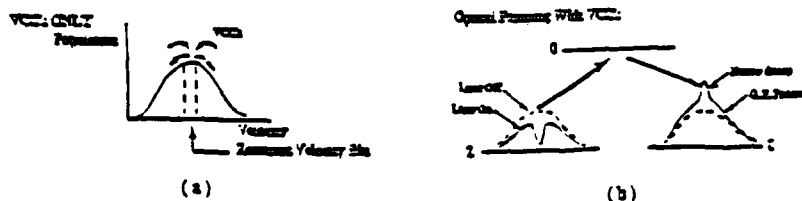


Fig. 1 Laser Optical pumping with VCC.

As Fig. 1a shows, vcc's knock atoms out of the resonant velocity bin and distributes them over the remainder of the Doppler distribution. Simultaneously vcc's are also knocking atoms into the resonant bin. The net effect produces increased Doppler coverage [2]. The effect of the vcc's on the optical pumping process is shown in Fig. 1b. Anisotropy is caused by the excess population transferred to level 1. This population consists of a broad (Doppler width) optical pumping pedestal and a narrow (sub-Doppler width) feature. The pedestal is produced by those isomers that undergo vcc's before they decay, whereas the narrow bump represents isomers that decay before any vcc's. For a given intensity and increasing buffer gas pressure the pedestal will grow at the expense of the bump. At high enough pressures the bump will disappear and the experiment enters the Doppler limited regime [2]. So to achieve sub-Doppler resolution it is crucial that the buffer gas pressure be low enough for the narrow feature to be present.

III. Sub-Doppler LINO

As the above discussion indicates, sub-Doppler resolution requires low buffer gas pressures. This is a disadvantage because there is a decrease in signal size due to incomplete Doppler coverage. A further reduction in signal size also occurs if the buffer is the parent.

However, since the saturation intensity is proportional to the vcc rate [3], it becomes easier to saturate a particular velocity group. Hence less intensity is required to saturate and larger cell volumes can be pumped, with a corresponding increase in signal size.

These effects can be combined in such a way as to result in reasonably sized signals. The key is to determine the optimum cell design (i.e. volume, pressure, etc.) for a given laser power.

IV. LINO and Saturation Spectroscopy

In our experiments the saturation effect of two counter-propagating pump beams (Lamb-dip configuration) is used to produce the sub-Doppler anisotropy signal.

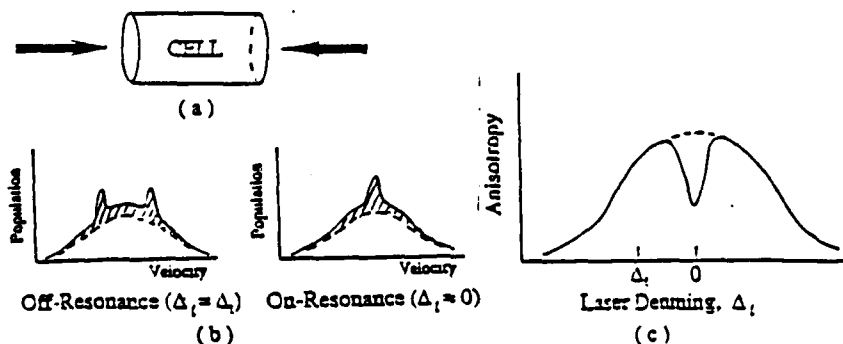


Fig. 2 Saturation and Anisotropy

Figure 2 shows this effect. The anisotropy is proportional to the area under the excess population transferred to the unpumped level, as depicted by the shaded portion of Fig. 2b. Due to the nonlinearity of saturation, the area off resonance is larger (more efficient pumping) than the area on resonance (less efficient pumping). So, as Fig. 2c shows, as the laser is tuned through the hf transition, the anisotropy is greater off resonance than near or on resonance. This decrease manifests itself as a sub-Doppler anisotropy signal, much in the same way as the usual Lamb-dip does in ordinary spectroscopy.

V. Experiments and Results

Figure 3a shows the production scheme for the $1\mu s$ ^{85}Rb isomer, which decays with the emission of a 514 keV gamma ray. The anisotropy is produced by optical pumping on the D1 transition ($\lambda = 7947 \text{ \AA}$). The pumping scheme is depicted in Fig. 3b. A linearly polarized beam pumps the $F = 5$ to $F' = 4$ hf transition. The anisotropy is created by the excess population transferred to the end $M_F = \pm 5$ sub-levels. Since the ground state hf splitting of 12.5 GHz is much larger than the Doppler width, population also accumulates in the $F = 4$ hf level. The overall effect is added to the isotropic background.

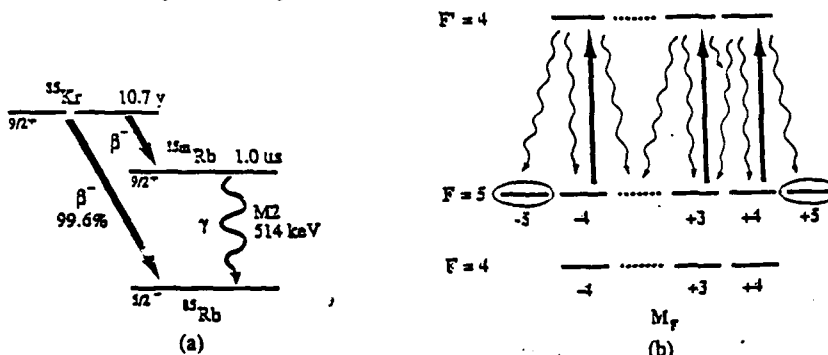


Fig. 3 ^{85}Kr decay and optical pumping schemes.

The experimental setup is shown in Fig. 4. The cell contains 300 mTorr of krypton, which is the parent and also acts as a buffer gas, plus natural rubidium for resonant charge exchange. The number of isomers in the cell is much less than one. Two counterpropagating beams of equal power (150 mW) are incident on opposite faces of the cell. The beams are formed by splitting the output beam from a dye

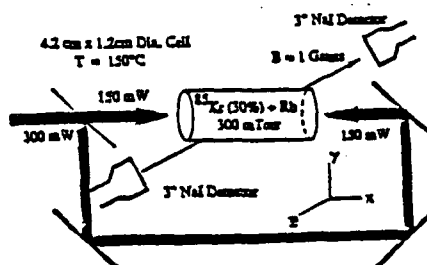


Fig. 4 Experimental set up.

ring dye laser utilizing LD700 dye and pumped by a 5 W krypton ion laser. The sub-Doppler anisotropy change signal is shown in Fig. 5a. The solid curve is a computer fit. The signal shows a narrow feature with a 90 MHz width (FWHM) resting on the beginnings of a broad optical pumping pedestal. Each data point represents five hours of counting time, done in ten minute intervals to correct for laser drift, etc. Figure 5b shows that the width of the sub-Doppler signal is approximately 10% of the Doppler width.

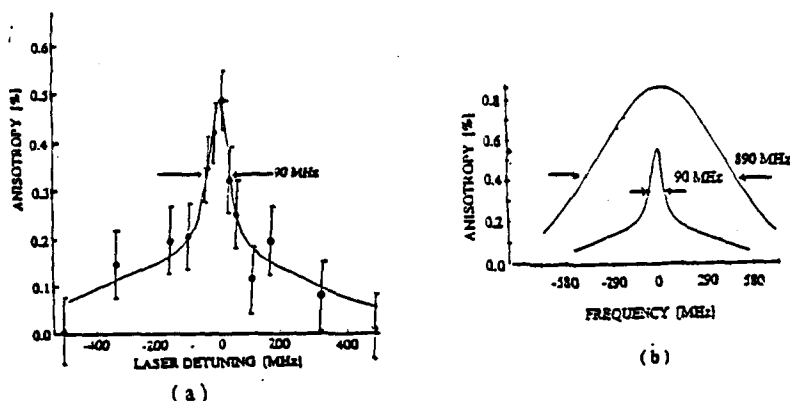


Fig. 5 Sub-Doppler anisotropy change signal

VI. Future Prospects

Our next step is to use sub-Doppler LINO to make the first measurements of the ^{85}Rb electric quadrupole moment. This requires that we apply LINO to the D2 transition, where the estimated excited state hf splittings are less than the Doppler width. We will also utilize sub-Doppler LINO in precise on-line studies of chains of very shortlived isotopes and isomers.

In addition to the above projects, LINO will be applied to kinematic studies of the weak interactions. Generally speaking, in these kinds of experiments the recoil of the daughter is studied. One such experiment uses LINO to measure the electron-antineutrino angular correlation in ^{85}Kr beta-decay [4]. Although not necessarily an application of LINO, it may also be feasible to use lasers to search for neutrino mass in bound-state beta-decay studies [5] and electron capture.

¹ Physics Department Wellesley college, Wellesley, MA 02181.

² L-43, Lawrence Livermore Natl. Laboratory, Livermore, CA 94550.

³ Dept. of Physics & Astronomy, Colgate University, Hamilton, NY, 13346.

Hamilton, NY, 13346.

Department of Physics, Rutgers University, Newark, NJ.

References

1. M. Burns, P. Pappas, M.S. Feld, and D.E. Murnick, Nucl. Instrum. Methods 141, 429 (1977).
2. G. Shimkaveg et al., Phys. Rev. Lett. 53, 2230 (1984).
3. W.W. Quivers, Jr., Phys. Rev. A34, 3822 (1986).
4. J.T. Hutton and W.W. Quivers, Jr., Phys. Rev. C40, 314(1989)
5. S.G. Cohen, D.E. Murnick, and R.S. Raghavan, Hyper. Int. 33, 1 (1987).

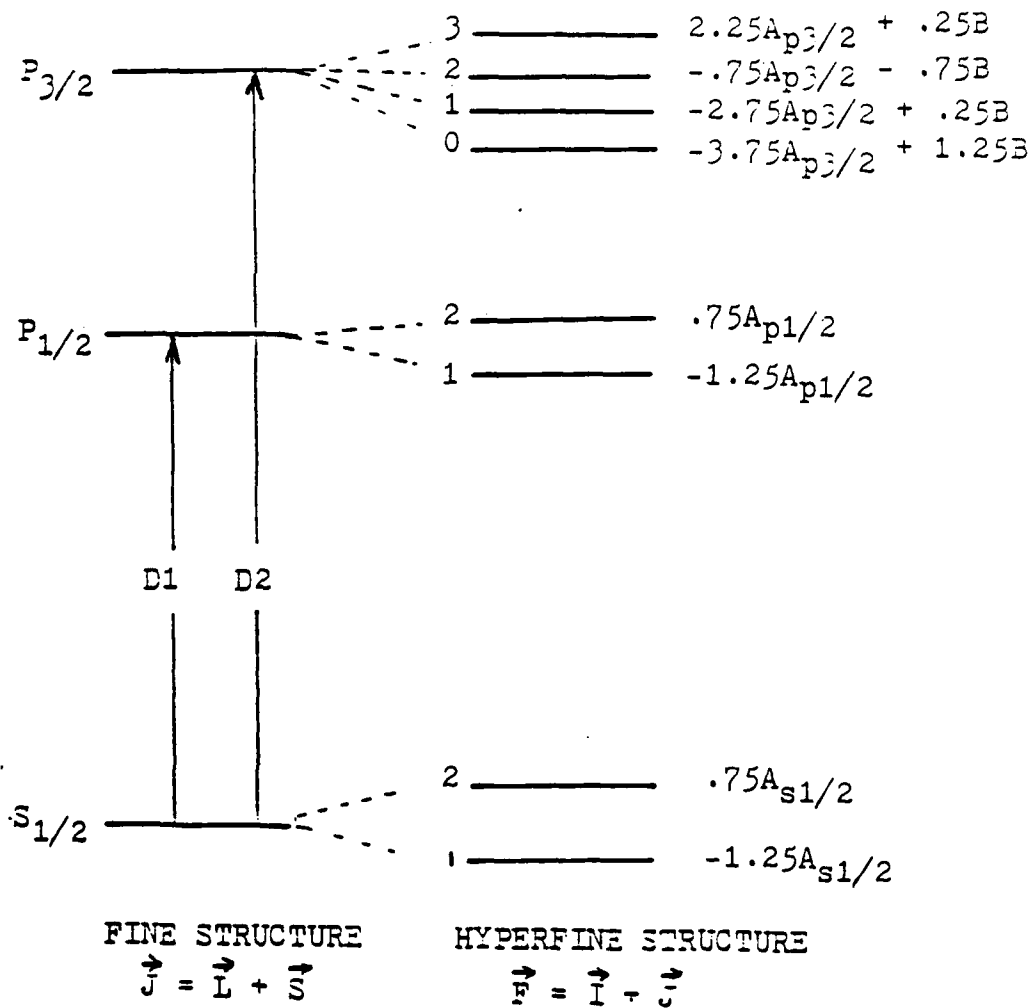
Appendix C

Hyperfine Structure of Natural Rubidium

Natural Rubidium, consisting of 78% ^{85}Rb and 28% ^{87}Rb , is used in this experiment for calibrating the location in frequency space of the ^{85m}Rb transitions. The hyperfine structure of both isotopes is given in this appendix. All A and B values are from Arimondo [18], and the isotope shift value is from Thibault,

^{87}Rb Hyperfine Structure

$$I = 3/2$$



$$A_{s1/2} = 3417.34130642$$

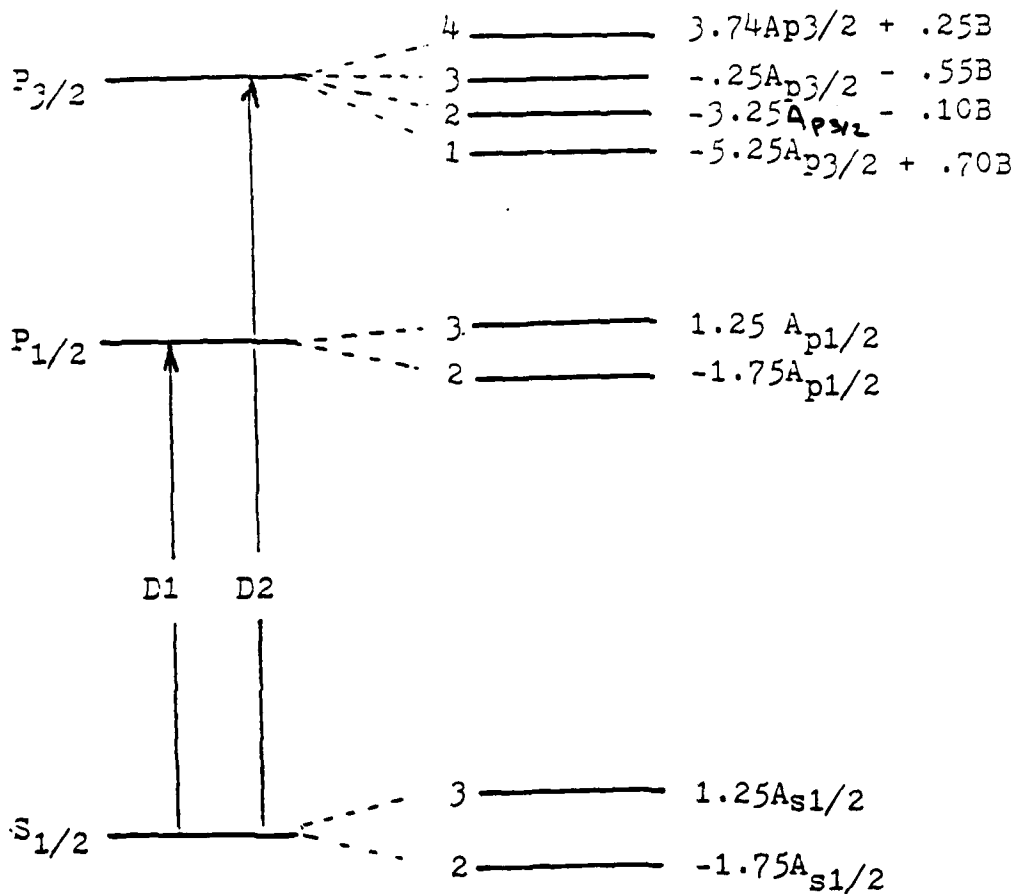
$$B = 12.52(9)$$

$$A_{p1/2} = 406.2(8)$$

$$A_{p3/2} = 84.845(55)$$

All Values in MHz. All values from Arimondo (see Ref).

^{85}Rb HYPERFINE STRUCTURE
 $I = 5/2$



FINE STRUCTURE

$$\vec{J} = \vec{L} + \vec{S}$$

HYPERFINE STRUCTURE

$$\vec{F} = \vec{I} + \vec{J}$$

$$A_{s1/2} = 1011.910813(2)$$

$$B = 25.88(3)$$

$$A_{p1/2} = 120.72(25)$$

$$A_{p3/2} = 25.009(22)$$

Isotope Shift From $^{87}\text{Rb} = -80.1$ (Thibault).

All values in MHz. All values from Arimondo except isotope shift.

LOCATION OF ^{87}Rb and ^{85}Rb TRANSITIONS
ALL LOCATIONS REFERENCE ^{87}Rb LINE CENTER
D₁ LINE: $5s^2S_{1/2} \rightarrow 5p^2P_{1/2}$ 7947 Å

hyperfine component	n_i/n_{Rb}	σ_i	center frequency (MHz) (± 2)
$^{87}\text{Rb } F=2 \rightarrow F'=1$.035	$5\pi\lambda^2$	-3071
$^{87}\text{Rb } F=2 \rightarrow F'=2$.035	$5\pi\lambda^2$	-2258
$^{85}\text{Rb } F=3 \rightarrow F'=2$.06	$(70/9)\pi\lambda^2$	-1558
$^{85}\text{Rb } F=3 \rightarrow F'=3$.06	$(56/9)\pi\lambda^2$	-1194
$^{85}\text{Rb } F=2 \rightarrow F'=2$.06	$(20/9)\pi\lambda^2$	1480
$^{85}\text{Rb } F=2 \rightarrow F'=3$.06	$(70/9)\pi\lambda^2$	1842
$^{87}\text{Rb } F=1 \rightarrow F'=1$.035	$\pi\lambda^2$	3764
$^{87}\text{Rb } F=1 \rightarrow F'=2$.035	$5\pi\lambda^2$	4576

$$\gamma_F = 9.9 \text{ MHz/Torr (HWHM)} \times p_{\text{Kr}}$$

$$\text{pressure shift} = -7.9 \text{ MHz/Torr}$$

$$\pi\lambda^2 = 5.03 \times 10^{-10} \text{ cm}^2$$

D₂ LINE: $5s^2S_{1/2} \rightarrow 5p^2P_{3/2}$ 7800 Å

hyperfine component	n_i/n_{Rb}	σ_i	center frequency (MHz)
$^{87}\text{Rb } F=2 \rightarrow F'=1$.035	$\pi\lambda^2$	-2793
$^{87}\text{Rb } F=2 \rightarrow F'=2$.035	$5\pi\lambda^2$	-2636
$^{87}\text{Rb } F=2 \rightarrow F'=3$.035	$14\pi\lambda^2$	-2369
$^{85}\text{Rb } F=3 \rightarrow F'=2$.06	$(20/9)\pi\lambda^2$	-1429
$^{85}\text{Rb } F=3 \rightarrow F'=3$.06	$(70/9)\pi\lambda^2$	-1365
$^{85}\text{Rb } F=3 \rightarrow F'=4$.06	$(162/9)\pi\lambda^2$	-1245
$^{85}\text{Rb } F=2 \rightarrow F'=1$.06	$(54/9)\pi\lambda^2$	1578
$^{85}\text{Rb } F=2 \rightarrow F'=2$.06	$(70/9)\pi\lambda^2$	1607
$^{85}\text{Rb } F=2 \rightarrow F'=3$.06	$(56/9)\pi\lambda^2$	1670
$^{87}\text{Rb } F=1 \rightarrow F'=0$.035	$2\pi\lambda^2$	3962
$^{87}\text{Rb } F=1 \rightarrow F'=1$.035	$5\pi\lambda^2$	4042
$^{87}\text{Rb } F=1 \rightarrow F'=2$.035	$5\pi\lambda^2$	4199

$$\gamma_F = 8.8 \text{ MHz/Torr (HWHM)} \times p_{\text{Kr}}$$

$$\text{pressure shift} = -8.8 \text{ MHz/Torr}$$

$$\pi\lambda^2 = 4.84 \times 10^{-10} \text{ cm}^2$$